ANALYSIS OF VIBRATION OF 2-D PERIODIC CELLULAR STRUCTURES

A Dissertation
Presented to
The Academic Faculty

by

Sang Min (Joseph) Jeong

In Partial Fulfillment
of the Requirements for the Degree
Doctor of Philosophy

School of Aerospace Engineering
Georgia Institute of Technology
May 2005

ANALYSIS OF VIBRATION OF 2-D PERIODIC CELLULAR STRUCTURES

Approved by:

Dr. Massimo Ruzzene, Advisor
School of Aerospace Engineering
Georgia Institute of Technology

Dr. Laurence J. Jacobs
School of Civil Engineering
Georgia Institute of Technology

Dr. Sathya V. Hanagud
School of Aerospace Engineering
Georgia Institute of Technology

Dr. Kenneth A. Cunefare
School of Mechanical Engineering
Georgia Institute of Technology

Dr. Dewey H. Hodges
School of Aerospace Engineering
Georgia Institute of Technology

Date Approved: May 16 2005

DEDICATION

In loving memory of my father, Ki-Taik Jeong.

ACKNOWLEDGEMENTS

First and foremost, I would to express my profound gratitude and appreciation to my advisor, Dr. Massimo Ruzzene, for his guidance, encouragement, support and patience.

I am indebted to Dr. Sathya V. Hanagud, Dr. Dewey H. Hodges, Dr. Laurence J. Jacobs, and Dr. Kenneth A. Cunefare for taking time out of their busy schedule to be on my thesis committee. Your insight on my research has been invaluable.

My heartfelt thanks to all my friends who have given me enduring support during this whole process. In particular, I would like to especially thank Hungjen John Shu, whose creative and artistic touch has made this dissertation that much better.

My life away from home would not have been easy without my surrogate family, so I would like to extend my thanks to my surrogate family, Mr Joseph and Mrs Chungsuk Whalen. Your concern and support in all my endeavors are deeply appreciated.

I would like to express my gratitude to my mother, Jum Soo Woo, and my brother, Sang Yol Jeong, for their love and support, and the sacrifices they made for me.

Lastly and most importantly, I would to thank God for being the pilot of my life and for giving me strength and hope. It is through Him that all things in my life is possible.

TABLE OF CONTENTS

DEDICATION . . . . . **iii**

ACKNOWLEDGEMENTS . . . . . **iv**

LIST OF TABLES . . . . . **ix**

LIST OF FIGURES . . . . . **x**

CHAPTER I INTRODUCTION **1**

1.1 Overview 1

1.2 Cellular Structures and their Application 2

1.2.1 Foams 2

1.2.2 Honeycomb materials and innovative sandwich core configurations . 4

1.2.3 Truss Structures and Lattices 6

1.2.4 Integrally Stiffened and AGS 9

1.2.5 Dynamic properties of periodic cellular structures 11

1.3 Periodic Structures 11

1.3.1 Early studies 12

1.3.2 Modern Advances in Wave Propagation Studies 12

1.4 Objectives and motivation of the work 14

1.5 Organization of the work 15

CHAPTER II WAVE PROPAGATION IN TWO-DIMENSIONAL PERIODIC STRUCTURES **17**

2.1 Overview 17

2.2 Bloch's Theorem 17

2.3 Group & Phase Velocity 18

2.4 A Simple Example: Spring-mass Lattice 21

2.4.1 Lattice Description 22

2.4.2 Particular Case: $m_1 = m_2$ 22

2.5 Spring-mass lattice with a "hard" inclusion 28

2.5.1 Bloch Reduction 30

2.5.2 First Brioullin zone and dispersion relations 33

2.5.3 Band-gap behavior . . . 34
2.5.4 Harmonic response of a finite lattice . . . 37
2.6 Energy Velocity . . . 39

CHAPTER III MODELING OF GENERAL LATTICE CONFIGURATIONS . . . 45

3.1 Overview . . . 45
3.2 Curved beam element . . . 47
3.2.1 Kinematic relations and displacement interpolations . . . 48
3.2.2 Strain-displacement interpolation . . . 50
3.2.3 Element Mass and Stiffness Matrix . . . 51
3.3 Curved Beam Model Validation . . . 52
3.3.1 Static Validation . . . 52
3.3.2 Dynamic Validation . . . 53
3.4 Spectral Beam Element Formulation . . . 54
3.4.1 Distributed parameter model in the local reference system . . . 57
3.4.2 Dynamic Stiffness Matrix in Local Coordinates . . . 59
3.4.3 Dynamic shape functions . . . 61
3.4.4 Performance of spectral finite elements . . . 62

CHAPTER IV ANALYSIS AND OPTIMIZATION OF RECTANGULAR GRIDS . . . 65

4.1 Overview . . . 65
4.2 Analysis of a baseline lattice configuration . . . 65
4.2.1 Geometry and material properties . . . 67
4.2.2 FE modeling of the unit cell . . . 67
4.2.3 Analysis of band-gap behavior and non-dimensionalization factor . . . 67
4.3 Directional and band-gap behavior of the grids . . . 72
4.3.1 Directional Behavior . . . 72
4.3.2 Band-gap Behavior . . . 75
4.4 Harmonic Response of rectangular lattices . . . 75
4.5 Optimization of 2-D rectangular grids . . . 81
4.5.1 Design variables and objective functions . . . 81

4.5.2 Optimization Results 82

CHAPTER V EXPERIMENTAL INVESTIGATIONS: RECTANGULAR GRID 86

5.1 Overview 86

5.2 Manufacturing Considerations 86

5.3 Configuration of Experimental Lattice 88

5.4 Experimental Validation 90

5.5 Experimental Setup for Band-gap Analysis 90

5.6 Experimental Results 93

CHAPTER VI CYLINDRICAL GRIDS 101

6.1 Overview 101

6.2 Harmonic Response of Rotationally Periodic Structures 101

6.2.1 Equivalent nodal load 104

6.2.2 Reduced equation of motion 105

6.3 Cylindrical Grid Configurations 107

6.3.1 FE discretization of unit cells 108

6.4 Performance of rectangular grids 110

6.4.1 Directional behavior: Phase constant surfaces 110

6.4.2 Harmonic response 111

6.4.3 Band-gaps 113

6.5 Performance of hexagonal grids 113

6.5.1 Phase constant surfaces 113

6.5.2 Harmonic response 118

6.5.3 Band-gaps 121

CHAPTER VII KAGOMÉ AND TETRAHEDRAL LATTICE STRUCTURES 125

7.1 Overview 125

7.2 Performance of Kagomé Lattice 126

7.2.1 Kagomé Lattice Configuration 126

7.2.2 Phase Constant Surfaces 127

7.2.3 Harmonic Response 128

7.2.4 Band-gaps . . . 132
7.3 Performance of Tetrahedron Lattice . . . 132
7.3.1 Tetrahedron Lattice Configuration . . . 132
7.3.2 Phase Constant Surfaces . . . 134
7.3.3 Band-gaps . . . 135
7.3.4 Harmonic Response . . . 135
CHAPTER VIII CONCLUSIONS . . . 142
8.1 Conclusions . . . 142
8.2 Future Work . . . 144
8.2.1 Experimental Validation of Complex Lattice Structures . . . 144
8.2.2 Cylindrical Lattice Structures . . . 144
8.2.3 Multifunctional Optimization . . . 145
REFERENCES . . . 146

LIST OF TABLES

Table 1 Unit Cell Configuration for $m_1 = m_2$, $k_1 = k_2$ 24

Table 2 Unit Cell Configuration for $m_1 = m_2$, $k_1 \neq k_2$ 26

Table 3 Unit Cell Configuration for $m_1 \neq m_2$, $k_1 = k_2$ 34

Table 4 Properties of Cantilevered Curved Beam 53

Table 5 FE predictions vs analytical solution for the tip deflection of cantilevered beam 54

Table 6 ANSYS vs FE predictions for the first 10 natural frequencies of a strip of 5 rectangular cells 55

Table 7 Material and geometry for the strip of 5 rectangular cells 55

Table 8 Material and geometry of the cantilever beam 63

Table 9 Mechanical properties and geometry of rectangular lattice. 67

Table 10 Summary of optimization results 82

Table 11 Parametric Study for Lattice Configuration 89

Table 12 Mechanical properties and geometry of experimental lattice. 90

Table 13 Experimental Equipment 93

Table 14 Geometry and material properties of cylinder 107

Table 15 FE mesh for rectangular cylindrical grids 109

Table 16 FE mesh for hexagonal cylindrical grids 110

Table 17 Mechanical properties and geometry of Kagomé truss core. 127

Table 18 Mechanical properties and geometry of Tetrahedron truss core. 134

LIST OF FIGURES

Figure 1 Closed and open cellular structures 2
Figure 2 Stochastic and deterministic cell architecture 3
Figure 3 Honeycomb sandwich panels 5
Figure 4 Prismatic Structures 6
Figure 5 Prismatic structures with different cores 7
Figure 6 Truss-core Structure 8
Figure 7 Truss Designs 9
Figure 8 AGS Structure 10
Figure 9 Examples of 1-D Periodic Structures 12
Figure 10 Local and Global Coordinates in a generic 2-D periodic structure 18
Figure 11 Phase Constant Surfaces 19
Figure 12 "Carrier" wave propagates at group velocity, c_g 20
Figure 13 Spring-mass Lattice & Cell 22
Figure 14 Spring-mass Unit Cell for $m_1 = m_2 = m$ 23
Figure 15 Phase Constant Surface for ε_x & ε_y from -2π to 2π 25
Figure 16 Phase Constant Surface: $2k_1/m = 2k_2/m = 1.0$ 25
Figure 17 Harmonic Response of Spring-Mass Lattice 27
Figure 18 Phase Constant Surface: $2k_1/m = 1.0, 2k_2/m = 2.0$ 28
Figure 19 Harmonic Response: $2k_1/m = 1.0, 2k_2/m = 2.0$ 29
Figure 20 Generalized boundary nodal displacements and forces 30
Figure 21 3-D Phase Constant Surfaces 34
Figure 22 First Brillouin Zone 35
Figure 23 Spring-Mass System: Dispersion Relations 36
Figure 24 Dispersion relations for various values of the internal mass 38
Figure 25 Unit cell mode corresponding to upper bound of band-gap 39
Figure 26 Amplitude of harmonic response of spring mass lattice at various frequencies 40
Figure 27 Excitation and Response Schematic 41
Figure 28 Frequency Response of the other three Corners 42
Figure 29 Considered Configurations 46

Figure 30 General curved beam element 48
Figure 31 Cantilevered curved beam 53
Figure 32 Strip of 5 Rectangular Cells 54
Figure 33 Mode Comparison 56
Figure 34 Beam element and considered degrees of freedom. 57
Figure 35 Cantilevered beam with tip load 63
Figure 36 FRF Comparison 64
Figure 37 Considered rectangular lattice 66
Figure 38 First Brioullin zone 68
Figure 39 Dispersion relations for increasing number of elements 68
Figure 40 Mesh selected for unit cell analysis (nodes 'o') 69
Figure 41 Dispersion relations for 2 grid configurations 70
Figure 42 Unit cell modes for grid with (a) and without (b) band-gaps 71
Figure 43 Comparison of non-dimensional dispersion relations for various grids . . . 73
Figure 44 First phase constant surfaces for different lattices 74
Figure 45 Sensitivity analysis of directional behavior 76
Figure 46 Dispersion relations for various gird configurations 77
Figure 47 Sensitivity analysis of band-gap width 78
Figure 48 Sensitivity of band-gap center frequency 78
Figure 49 Amplitude of harmonic response at $\Omega = 1.9$ for different lattices 79
Figure 50 Amplitude of harmonic response at $\Omega = 12$ for different lattices 80
Figure 51 Performance of optimal lattice with $d_2 = 2.5$, $d_3 = 0$ ($w_1 = w_2 = 1$, $w_3 = 0$) 83
Figure 52 Performance of optimal lattice with $d_2 = 1.67$, $d_3 = 2.49$ ($w_3 = 1$, $w_1 = w_2 = 0$) 84
Figure 53 Performance of optimal lattice with $d_2 = 2.27$, $d_3 = 1.68$ ($w_1 = w_2 = w_3 = 1$) 85
Figure 54 Unit Cell of Experimental Lattice 87
Figure 55 3-D Model of Lattice 87
Figure 56 Lattice Specimen 88
Figure 57 Clamped Corner and Point of Excitation 91
Figure 58 Frequency Response Comparison 91
Figure 59 Lattice Schematic 92

Figure 60 Schematic of experimental setup 93
Figure 61 Experimental Frequency Response Function 95
Figure 62 Experimental and Computational Band-gap 95
Figure 63 Harmonic response at 2500 Hz 96
Figure 64 Harmonic response at 3000 Hz (Band-gap) 97
Figure 65 Harmonic response at 3200 Hz 98
Figure 66 Harmonic response at 3050 Hz (Band-gap) 99
Figure 67 Harmonic response at 3100 Hz (Band-gap) 100
Figure 68 Curved rectangular cell and grid 102
Figure 69 Hexagonal cell and grid 103
Figure 70 Rotationally Periodic Assembly 104
Figure 71 Convergence of dispersion relations 109
Figure 72 First Brillouin Zone: Rectangular and Hexagonal Cylindrical Grid 109
Figure 73 Phase constant surfaces for rectangular grids (Bold lines: "Transition" frequency) 112
Figure 74 Propagation angles for rectangular grids 113
Figure 75 Harmonic response of first rectangular grid ($\alpha = 1$) 114
Figure 76 Harmonic response of third rectangular grid ($\alpha = 5$) 115
Figure 77 Dispersion relations for rectangular grids 116
Figure 78 Phase constant surfaces for hexagonal grids (Bold lines: "Transition" frequency) 117
Figure 79 Propagation angles for rectangular grids 118
Figure 80 Harmonic response for hexagonal grid with $\beta = 30^\circ$ 119
Figure 81 Harmonic response for hexagonal grid with $\beta = -30^\circ$ 120
Figure 82 Dispersion relations for hexagonal grids 122
Figure 83 Harmonic response for hexagonal grids 123
Figure 84 Sensitivity analysis for hexagonal grids 124
Figure 85 Considered Truss Cores 125
Figure 86 Unit Cell: Kagomé Truss 126
Figure 87 Dimensions of Kagomé Unit Cell 127
Figure 88 Phase Constant Surface: Kagomé Truss 128
Figure 89 Kagomé Lattice: Point of Excitation 129

Figure 90 Harmonic Response of Kagomé Lattice: $D_2 = D_1$ 130
Figure 91 Harmonic Response of Kagomé Lattice: $D_2 = 2D_1$ 131
Figure 92 First Brillouin Zone: Kagomé Truss 132
Figure 93 Dispersion Relations: Kagomé Truss 133
Figure 94 Dimensions of Tetrahedron Unit Cell 134
Figure 95 Tetrahedron Unit Cell with Re-entrant Geometry 135
Figure 96 Phase Constant Surface: Tetrahedron Truss 136
Figure 97 First Brillouin Zone: Tetrahedron Truss 137
Figure 98 Dispersion Relations: Tetrahedron Truss 138
Figure 99 Tetrahedron Lattice: Point of Excitation 139
Figure 100 Harmonic Response of Tetrahedron Lattice: $\beta = 30°$ 140
Figure 101 Harmonic Response of Tetrahedron Lattice: $\beta = -30°$ 141
Figure 102 Curved Truss Core Panel 144

CHAPTER I

INTRODUCTION

1.1 Overview

Cellular structures consist of an interconnected network of solid struts or surfaces which form the edges and faces of cells [1]. This general definition applies to a wide variety of natural systems, such as for example balsa wood, cancellous bone, corals and corks, as well as man-made constructions. Typical examples include among others foams, honeycomb materials and truss assemblies. In general, a structural assembly can be classified as"cellular" based on its so-called "relative density". Relative density is defined as the ratio of the density of the assembly ρ_s to the density of the constitutive material of the cell ρ_c. Typically, cellular structures feature a relative density which is equal or lower than 0.3, while structures with relative density above 0.3 are simply considered as porous solids.

A first classification based on the cell configuration differentiates between closed and open celled cellular structures [1]. Closed-cell structures feature cells which are interconnected via a solid surface and are sealed off from their neighbors (Fig. 1.a), while in open-celled structures the cells are interconnected via struts or surfaces with openings (Fig. 1.b). Another distinction is based upon the architecture of the cellular assemblies. Stochastic structures feature cells whose geometry, shape and dimensions vary spatially within the component, while deterministic architectures are obtained by the assembly of identical cells identically connected to cover the volume of the assembly (Fig. 2). This last category has recently become the object of extensive research. Deterministic cellular assemblies can be in fact employed in the development and implementation of structures with superior thermal, mechanical and acoustical properties [2]. Recent advances in manufacturing techniques have opened the possibility of generating deterministic topologies which can be optimized to improve a specified set of performance indexes. Previous investigations have shown how optimal configurations can be obtained through the proper design of the unit cell, and that multi-functional characteristics can be easily achieved [3]. The previous investigations have mostly addressed static mechanical performance [4] and thermal characteristics [5], but have

not yet investigated the characteristics of the dynamic behavior of this class of structural assemblies. Hence, the objective of the work described in this dissertation is the study of the dynamic properties of cellular structures with deterministic architecture, with focus on the analysis of their application for the design of mechanical components with vibration isolation and wave attenuation capabilities. This is done by recognizing that cellular structures can be considered as periodic structures. The description of several existing cellular concepts and their application follows this introduction. Then a chronological summary of the major research contributions to wave propagation in periodic structures is given. The overview and summary of the state-of-the-art will then be used as a basis for the formulation of the objectives of the present work. The outline of the dissertation will then conclude the chapter.

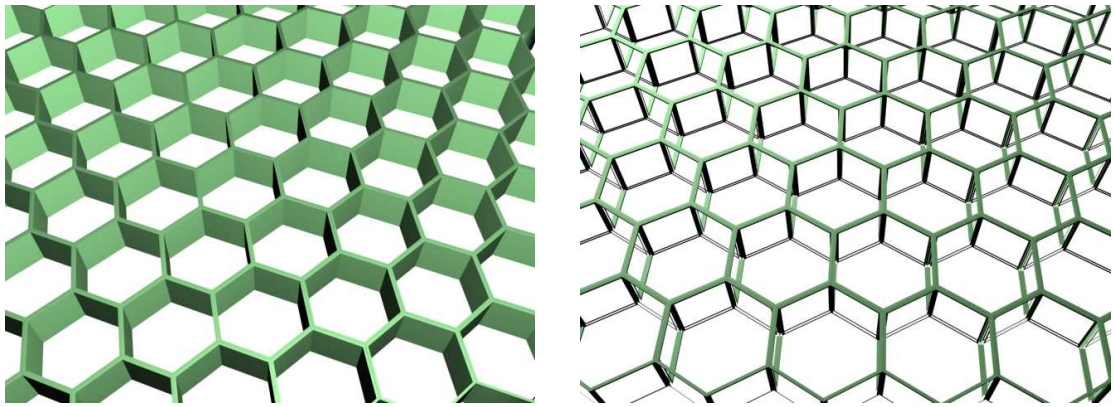

(a) Closed Cell (b) Open Cell

Figure 1: Closed and open cellular structures

1.2 Cellular Structures and their Application

1.2.1 Foams

Foams are probably the cellular-type structures finding the widest range of application. Their material, geometry and configuration can be all defined and properly selected to maximize the foam performance for a required functionality. Foams first of all possess properties which make their application attractive at both ends of the thermal application spectrum, i.e. both for high heat insulation or high conductivity performance. Plastic and

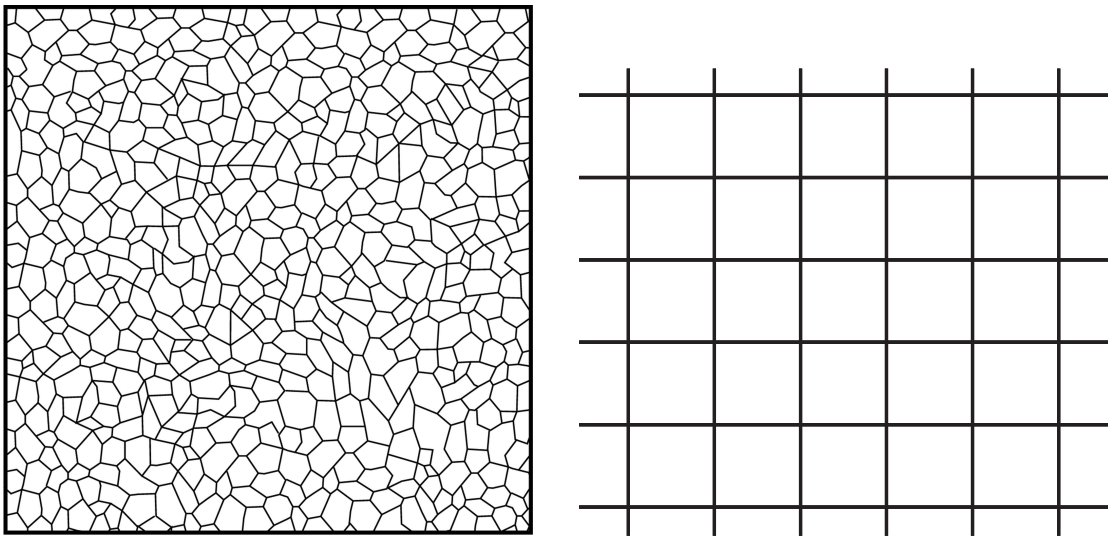

(a) Stochastic Cells (b) Deterministic Cells

Figure 2: Stochastic and deterministic cell architecture

glass foams feature for example very low thermal conductivity. They are typically used as thermal insulators, from something as simple as disposable cups to more elaborate applications on space vehicles. Foams are used for examples as thermal and acoustic insulators on the Space Shuttle [1]. In addition, a variety of transport systems, ranging from refrigerated trucks, railway cars and ships, use plastic foams as thermal insulators. For applications where there may be a fire hazard or where durability is of great importance, glass foams are used instead. Glass foams are employed extensively in building construction and for pipe insulation. Conversely, metallic foams have shown great promise as thermal conductors. Evans and his coworkers [2] have for example investigated the thermal properties of cellular metals versus polymer and ceramic counterparts. They found that the thermal conductivity of cellular metals is significantly larger compared to polymer and ceramic alternatives. In fact, their thermal diffusivity is comparable to that of dense metals [3]. Soft cellular foams also exhibit good sound absorption capabilities and are used to line enclosures for reducing noise transmission [2]. The acoustic properties of metallic foams have also been analyzed [2]. Although not as good as sound absorbers as soft foams, metallic foams combine acceptable acoustic properties with structural strength and rigidity which make them attractive for several structural-acoustic applications [2]. Additional applications for foams include blast

and impact protection and the manufacturing of buoyancy devices. The concept behind blast and impact amelioration is to convert the kinetic energy at impact to some other form, usually heat, through plasticity, viscosity, visco-elasticity or friction. Cellular structures, and particularly cellular foams, exhibit exceptional potentials for energy conversion and accordingly have been extensively employed for packaging and shielding sensitive equipment. For marine buoyancy, corks have been used as fishing floats since the early days, and nowadays closed-cell plastic foams are becoming the standard material used for flotation devices. As opposed to flotation bags or chambers, the closed cell configuration allows the foam to retain buoyancy even after extensive damage has occurred. In addition, open-celled structures are commonly used as filters in many different applications. Ceramic foams are used in the manufacturing of high quality metal castings to filter out any inclusions. More common applications include using a foam pad as a disposable air filter. Recent advances have allowed the advent of special open cell foams that can act as molecular filters, separating molecules of different types in solution. Foam sheets can be used as carrier for inks, dyes and even enzymes for chemical processing. Cells are saturated with the media to be carried and the media is either expunged slowly by allowing it to leak out of the cellular structure at a controlled rate or expelled quickly by applying a force. Ceramic foams or honeycombs lightly coated in aluminum are used as carriers of catalyst in automobiles and energy-related applications.

Finally foams can be commonly employed as core material in sandwich panels characterized by high stiffness-to-weight ratios and high energy absorption capabilities. Sandwich panels are used extensively in the transportation industry and their introduction dates back to World War II.

1.2.2 Honeycomb materials and innovative sandwich core configurations

Recent advances have made sandwich panels a mainstay in aerospace applications. Carbon-fibre composites skins bonded to aluminum and paper-resin honeycombs, or rigid polymer foams have replaced plywood and balsa wood cores proposed in early designs, and are now used in practically all modern day aircrafts, as well as on ships and on light, high speed

rail trains [1]. Honeycomb sandwich structures generally possess high bending stiffness and strength while weighing orders of magnitude less than their solid counterparts. Traditional configuration for honeycomb materials consists of a periodic sequence of hexagonal cells. Various alternatives to this layout have been proposed in the past and some have been successfully employed. Among the most promising innovations in the area of honeycomb design is the application of re-entrant geometries. Honeycomb assemblies with negative internal angles as shown in Fig. 3.b have demonstrate a number of superior properties, which include higher shear modulus, higher indentation resistance and higher flat-wise strength [6].

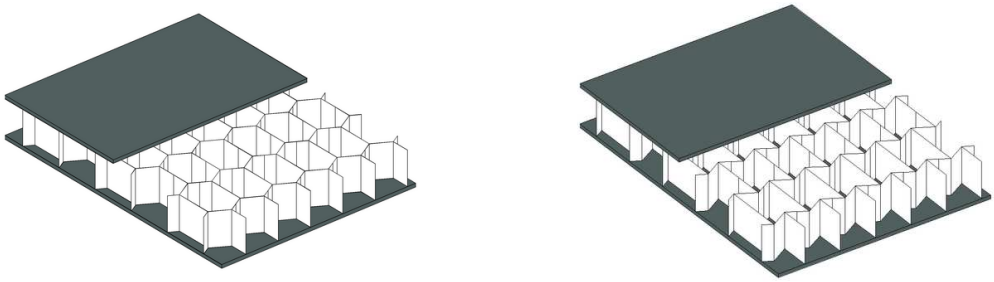

(a) Regular honeycomb core (b) Re-entrant honeycomb core

Figure 3: Honeycomb sandwich panels

New manufacturing techniques have recently allowed the exploration of completely different configurations for sandwich construction. One of these innovative designs include the prismatic material concept shown in Fig. 4. Prismatic materials have periodic, open channels that extend over the length of the structure. This class of structures exhibit structural properties that make them suitable for ultralight applications and also possess other desirable engineering characteristics. For example, Evans investigated the thermomechanical properties of prismatic materials and found that the cell size and density of the prismatic structure had a strong influence on the thermomechanical properties [2]. This meant that thermal properties of cellular metals can be controlled by changing cell geometry and topology. This additional design flexibility makes cellular structures a very attractive alternative

in the design of heat sink systems.

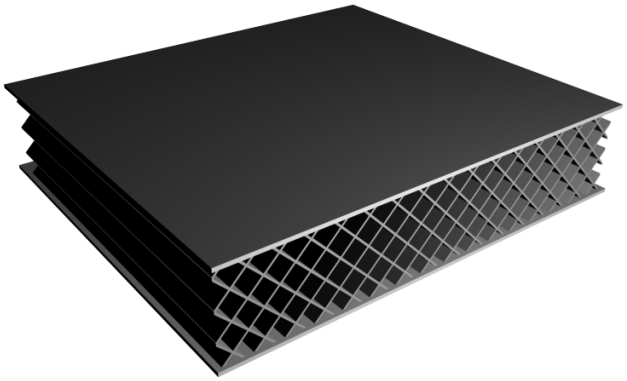

Figure 4: Prismatic Structures

Recognizing this unique capability of prismatic structures, Gu and coworkers [5] attempted the design optimization of cellular metals for combined heat dissipation and structural load capacity. A two stage optimization was carried out to identify the cell morphologies that optimize the structural and heat transfer performance. Three types of core design, rectangular, triangular and hexagonal, were considered (Fig. 5). It was found that the hexagonal core provided the best heat dissipation relative to density, but the rectangular core demonstrated the greatest stiffness. For thin panels, it was found that triangular cells provided the best compromise for stiffness and heat dissipation, making it a desirable design for a compact yet stiff heat sink. However, in the case of high heat flux scenarios where thick cores are required, hexagonal cells significantly outperform both triangular and square cells.

1.2.3 Truss Structures and Lattices

The truss-core concept is another innovative design for sandwich components (Fig. 6). This new class of structures has been proposed and investigated by many researchers for various purposes [7, 8, 9, 10]. Truss-core structures feature a core with interconnected bars to form a truss of given topology. Recent developments in manufacturing make it possible to produce

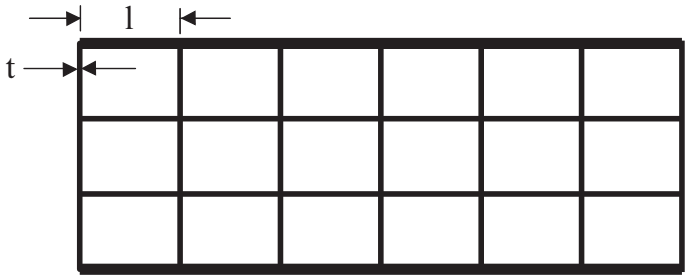

(a) Rectangular Core

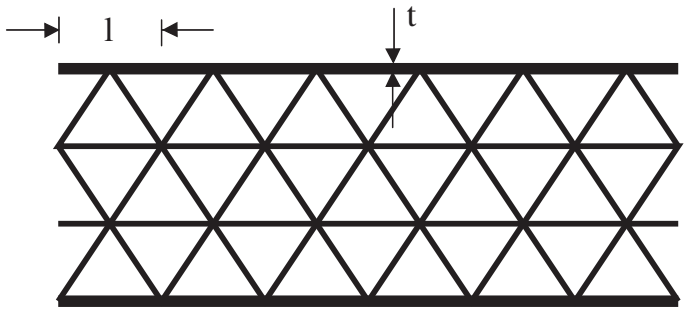

(b) Triangular Core

Figure 5: Prismatic structures with different cores

cores of various geometries and scales to fit requirements of various applications.

Wallach and Gibson [8] for example investigated the mechanical properties of a truss-core structure with a fully triangulated periodic unit cell. Their results showed good agreement between the computed and the experimentally derived properties. In addition, they found that the proposed truss-core design showed improved properties over commercially available closed-cell aluminum foam. Wicks and Hutchinson [11] investigated the strength of tetragonal truss-core plates in bending and shear optimized for weight purposes. These optimized truss-core plates were then compared with similarly optimized honeycomb sandwich panels. The strength to weight efficiency for both types of plates were strikingly similar. Sandwich panels with honeycomb cores have long been regarded as the most efficient design for ultralight applications. However, Wicks and Hutchinson's investigations show that truss-core structures have comparable strength to weight efficiency and have better durability and fewer manufacturing concerns. This makes truss-core structures ideal candidates as a replacement for sandwich honeycomb panels.

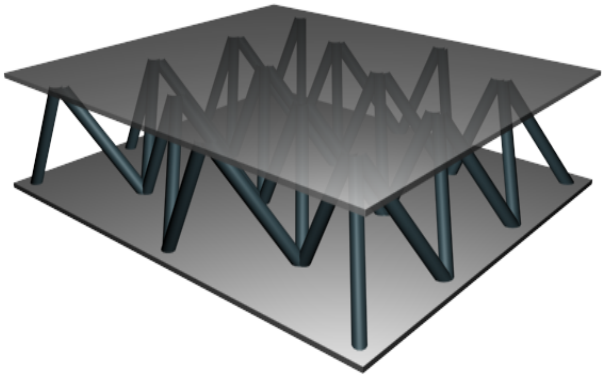

Figure 6: Truss-core Structure

Liu and Lu [4] tackled a multi-objective and multi-loading optimization of two types of truss-core structures, one with a tetrahedron core and one with a plagihedral pyramidal core (Fig 7). The truss-core panels were optimized for three loading conditions, namely bending, twisting and torsion, and for minimum mass. Liu and Lu were able to achieve through their optimization about a 10% decrease in maximum deflection, about a 40% decrease in maximum stress in the struts and facesheets, to increase the first natural frequency from 26.9 to 30.3 Hz and reduce the required structural mass by 20%.

Truss structures also represent an exceedingly common cellular structural concept. Truss or lattice structures are very similar to truss-core structures, except that they do not have face plates. Civil and aerospace engineering applications include wooden truss structures used extensively in building construction, metal truss structures used for bridges and heavy machinery such as cranes, and space platforms, antennae and long satellite booms. Truss designs in general combine low weights with high design flexibility, whereby several shapes and configurations can be obtained through the proper assembly of interconnected beam systems. In addition, trusses can be easily actuated at the joints to modify shape and

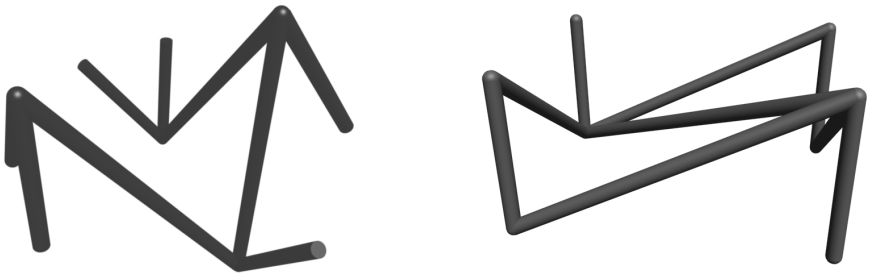

(a) Tetrahedron Truss (b) Plagihedral Pyramidal Truss

Figure 7: Truss Designs

configuration or to deploy the structure to its full extent. This characteristic in particular makes truss structures suitable for aerospace applications, where truss structures can be collapsed and packaged easily into much smaller containers and fully deployed later when they reach their destination. Space mirrors and deployable antenna systems are examples of such lattice-type large space structures (LSS).

1.2.4 Integrally Stiffened and AGS

Advanced Grid Stiffened (AGS) structure (Fig. 8) is a design concept that evolved from early isogrid stiffening concepts [12]. Instead of having simple isogrid stiffeners, AGS structures are characterized by a lattice of rigid, interconnected ribs that are inherently stronger and more resilient than its isogrid precursors.

Huybrechts and Meink [13] demonstrated the multifunctionality of AGS structures by presenting the manufacturing techniques which allow automation and lower cost. With the recent advances in manufacturing techniques, namely the SnapSat concept from Composite Optics Inc., and the Tooling Reinforced Integral Grid (TRIG) concept from Stanford University, Huybrechts and Meink believe that AGS can become an affordable and high quality replacement for many of the isogrid structures used in aerospace applications. In particular, they believe that AGS structures can replace the aluminium isogrid stiffened structures used as launch vehicle shrouds and interstages.

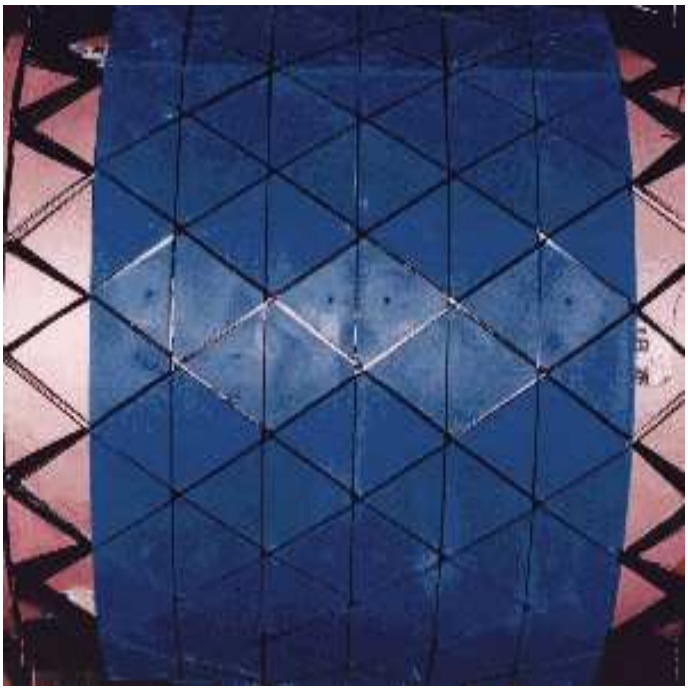

Figure 8: AGS Structure

Meink [14] also compared the performance of a composite AGS structure to a more conventional composite sandwich structure used as a part of a payload shroud. The weight efficiencies of both structures were found to be equivalent. The composite sandwich structure gives a higher safety margin in global buckling, but the AGS structure exhibited higher in-plane stiffness resulting in deflections approximately 28% lower and analysis yielded higher natural frequencies for the AGS structure, which should provide lower acoustic transmission. Another factor favoring the AGS structure was the manufacturing cost, where grid structures have shown to be well suited for an automated production environment. Additionally, the AGS structure was shown to be more damage tolerant. AGS structures also exhibit several improvements over conventional machined aluminum structures, as shown by Vipperman et al [15]. AGS structures show great improvement in weight (60% decrease) and strength (1000% increase in strength along the hoop direction) and a reduction of the transmission [15], which is a measure of the incident acoustic power that is transmitted through the structure.

1.2.5 Dynamic properties of periodic cellular structures

Most of the configurations previously described can be classified as deterministic cellular structures, as they can be considered as generated by the assembly of identical unit cells identically connected to each other. This simple observation represents the main motivation for this work. In fact, structures with spatial periodicity, such as those described above, have attracted the attention of a large number of researchers engaged in the broad areas of elastic wave propagation and structural dynamics. The unique behavior of periodic structures is associated with the destructive/constructive interference patterns which occur as a result of the interaction between incident and waves reflected by the material and/or geometrical discontinuities which identify each cell. Such interference patterns cause waves to propagate only over specified frequency bands, called the pass band, while being attenuated at all other frequencies. A wealth of information is available on the unique vibration and wave propagation characteristics of beams and plates periodically supported or stiffened, and on their unique filtering characteristics. The methodology for the analysis available in the literature can be directly transferred and extended to be applied to deterministic cellular structures and to investigate their dynamic and wave propagation characteristics.

1.3 Periodic Structures

Periodic structures consist of identical substructures or cells connected in an identical manner. One-dimensional (1-D) periodic structures are made up of repeated cells connected along one dimension. Examples of such structures include simple systems such as an interconnected series of lumped masses and springs (Fig. 9.a), uniform beams with supports at regular intervals [16] (Fig. 9.b), or a bi-material beam (Fig. 9.c). Two-dimensional (2-D) periodic structures consist of the repetition of the cell in two directions to cover a plane (Fig. 2.b). Beam grillages, orthogonally stiffened plates and shells are common examples of 2-D periodic structures.

Periodic structures exhibit unique dynamic characteristics. Wave propagation only occurs over specific frequency bands known as 'pass bands', while attenuation occurs over other frequency bands called 'stop bands'. The spectral width and location of these bands

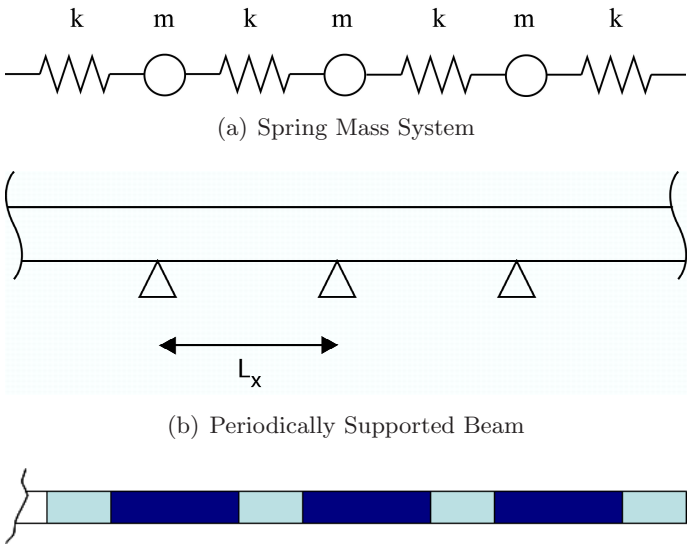

(a) Spring Mass System

(b) Periodically Supported Beam

(c) Bi-Material Beam

Figure 9: Examples of 1-D Periodic Structures

are dependent on the cell geometry and topology.

1.3.1 Early studies

The study of vibration of periodic structures can be traced back to the times of Sir Isaac Newton [17]. The early investigations were restricted to simple systems like lumped masses joined by massless springs (Fig. 9.a). The analysis of such a simple discrete system was however sufficient to determine the underlying principles of free wave propagation in periodic structures.

In 1887, Lord Rayleigh [18] made the first study of a continuous periodic assembly. He investigated a stretched string with density varying periodically along the length and undergoing transverse harmonic motion. Rayleigh solved the governing wave equation of second order with a periodic coefficient using Hill's method. His solution yielded the phase velocities of propagating waves and the spatial decay factor for attenuating waves.

1.3.2 Modern Advances in Wave Propagation Studies

Between 1900 and 1960, several mathematical techniques were developed for studying complicated crystal lattice structures, periodic electrical circuits and continuous transmission

lines [17]. Many of these techniques were then applied to the problem of continuous periodic engineering structures. In 1953, Cremer and Leilich [16] applied some of these techniques to investigate the problem of a 1-D periodic beam with simple supports at regular intervals. This system is considered a "mono-coupled" periodic system, because a basic cell is coupled to its neighbors through a single degree of freedom at the supports, which in this instance is the rotation at the supports. Structures with cells sharing more than one degree of freedom are instead denoted as "multi-coupled". Cremer and Leilich discovered that a continuous periodic system has an infinite number of alternating attenuation and propagation zones. In 1956, Miles [19] studied the natural frequencies of a finite periodic uniform beam resting on an arbitrary number of simple supports, another mono-coupled system, using receptance functions. In 1964, Heckl [20] investigated a 2-D periodic structure consisting of a rectangular grillage with interconnected uniform beams. Using reflection and transmission coefficients, Heckl was able to come up with a simple, albeit approximate solution. The early work on periodic structures at the University of Southampton was done using the receptance method. Mead and Wilby first looked at a 2-D stiffened plate using a quasi-1-D approximation [21]. Sen Gupta then extended this work to rib-skin structures and orthogonally stiffened plates, without the quasi-one-dimensional approximation [22]. Gupta's work confirmed that at over certain frequency ranges, there could be a pair or two pairs of propagating constants, but over other ranges, none could be found [23]. Y.K. Lin and coworkers considered the transfer matrix approach for solving 1-D or quasi-1-D periodic systems. The transfer matrix approach uses a "period transfer matrix" to relate the generalized displacements and forces of two neighboring cells. Gupta [22] expanded on the technique and demonstrated how the propagation constants can be found through the eigenvalues of the transfer matrix. In 1978, De Espindola [24] used transfer matrices to study the free and forced wave propagation along a cylinder with periodic stiffening, using a quasi-one-dimensional approximation. Zhong and Williams [25] later refined the approach to reduce the computational cost.

In 1973, Abrahamson applied energy principles to the problem of wave propagation in periodic structures [26]. Abrahamson developed a Rayleigh-Ritz method for finding the pass

band frequencies for a series of approximate wave modes. Abrahamson applied his Rayleigh-Ritz methods to periodic beams and rib-skin structures. His technique however had the drawback of requiring the careful selection of suitable complex modes to satisfy boundary conditions. Extending this work, Mead [27] presented his general theory of harmonic wave propagation in multi-coupled 1-D and 2-D periodic systems. The critical advance made in Mead's paper was the formulation of generalized equations of motion for a periodic element within a multi-coupled periodic system through which wave propagation occurs. Lagrange's equations were used to set up the initial equations of motion, then the wave-boundary conditions were applied. This leads to an eigenvalue problem that could be solved for the propagation frequencies for an enforced set of propagation constants. Orris and Petyt [28] extended this general theory of harmonic wave propagation to finite element formulations and used it to investigated the frequencies of 1-D periodic beams and rib-skin structures. This was the first instance of applying finite element to the study of periodic structures. The following year, Orris and Petyt [29] extended their work to compute the response of infinite periodic beams and rib-skin structures to convected random pressure fields. In the late 1980s, Mead and coworkers [30] combined the general theory of harmonic wave propagation with the hierarchical finite element method to investigate periodic plates and periodically stiffened cylinders. Through intensive computer processing, phase constant surfaces for several different stiffened cylinder configurations were obtained together with their natural frequencies and modes.

The early investigations of Orris, Petyt, and Mead and coworkers in this area, set the basis for much of the recent research in periodic structures, namely the use of finite element methods in conjunction with the general theory of periodic structures.

1.4 Objectives and motivation of the work

While cellular structures have a myriad of properties and can be applied to many different fields, their true potential is associated with their multifunctional characteristics. This adds a dimension to the design of structures that was previously unavailable. In applications where there is a single design criteria, e.g. highest strength to weight performance, existing

structures are sufficient, and cellular structures provide comparable but not necessarily superior performance. However, this is seldom the case in real life applications. For example in most structural applications, a load bearing structure has a primary role of carrying loads, but it typically has several secondary roles. A pressurized cylinder primarily has to be able to withstand the pressure it is designed for, but it may also need to reduce the acoustic transmission to and from the surrounding fluid. It is in these types of applications where cellular structures truly stand out as an attractive or possibly the only alternative.

The static mechanical performance, the thermal characteristics and the blast amelioration and impact absorption characteristics of cellular structures are now widely documented and supported by investigations by several research groups [1, 2, 3, 5, 31]. To this date however, very little work has been performed on the unique dynamic properties of the various cellular concepts. The focus of this work is therefore the investigation of the unique filtering capabilities of cellular structures in order to add yet another dimension to their multifunctional capabilities.

1.5 Organization of the work

The filtering capabilities of periodic assemblies are first demonstrated on simple lattice structures. The simple geometries allow defining the influence of parameters like geometry and cell topology on the dynamic characteristics of the structure. The study is performed through the application of the methodologies for two-dimensional (2D) periodic structures summarized in Chapter 2 of this dissertation. The evaluation of the wave propagation characteristics is based upon a detailed model of the dynamic behavior of the unit cell. The model is formulated by considering the cells as assembly of beam elements discretized using the Finite Element Method. The considered grid topologies required the development of a general curved beam finite element model, whose formulation is described in detail in Chapter 3. Also the validation of the predictions from the unit cell analysis requires the evaluation of the harmonic response of the complete structure. This can in principle represent a computationally intensive task as the number of cells composing the considered

structure is elevated. Computational burden is reduced through the application of the spectral finite element method which is also detailed in Chapter 3. A study follows in Chapter 4 where these developed techniques are applied to an investigation of the influence of the cell geometry on wave propagation characteristics of rectangular lattices. The investigation on rectangular lattices is concluded in Chapter 5 through the experimental validation on a simple specimen, where the filtering capabilities of periodic cellular structures are physically observed through the use of laser vibrometry. The work then extends the methodology to consider more complex grid-like structures with real life applications, e.g. grid stiffened cylindrical and truss core structures. For the specific case of cylindrical grid like structures, computational cost can be lessened by taking advantage of the rotational periodicity. This technique is described in Chapter 6 and applied to different cylindrical grid structures to investigate the influence of cell topology. The numerical techniques developed in this work are then extended to more complex lattice structures in Chapter 7. Results and insight from this work are summarized in Chapter 8 which also outlines possible extensions of this research.

CHAPTER II

WAVE PROPAGATION IN TWO-DIMENSIONAL PERIODIC STRUCTURES

2.1 Overview

Many engineering structures exhibit 1-D, 2-D or 3-D periodicity. Some common examples are stiffened plates and shells, and beam grillages. While these structures are always finite in dimensions and may have defects and flaws from manufacturing or wear and tear from use, wave propagation can still be studied by considering a suitable periodic idealization. In this work, wave propagation in 2-D periodic structures is studied by using Bloch's Theorem [17] as detailed in this chapter. The case of 1-D structures can be obtained as a special case, while the formulation for 3-D geometries comes as a natural extension and is not relevant to the developments presented in this dissertation.

2.2 Bloch's Theorem

A schematic of a generic 2-D periodic structure is shown in Fig. 10. The structure is assembled by identically connecting a basic unit or cell along the x-y plane. The configuration of a cell is described by a local reference x and y and it is identified by its location in the assembly by the pair of integers, n_x and n_y (Fig. 10). Bloch's theorem [17] states that a wave propagating in a 2-D periodic assembly can be described by the motion of a single cell and by a propagation vector defining wave amplitude and phase changes from one cell to the next. Accordingly, wave motion in a 2-D periodic structure can be described as follows:

$$\underline{w}(x, y, n_x, n_y) = \underline{g}(x, y) \cdot e^{\mu_x n_x + \mu_y n_y} \tag{1}$$

where $\underline{w}(x, y, n_x, n_y)$ is the displacement of a point x, y belonging to the cell at location n_x ,n_y, while $\underline{g}(x, y)$ describes the motion of the cell (Fig. 10). In the current development, vectors are denoted with underlined Greek or Latin letters, while matrices are indicated by bold capital Latin letters. Also in eq. (1), μ_x and μ_y are the propagation constants in the x and y direction. The propagation constants are complex numbers $\mu_k = \delta_k + i\varepsilon_k$ ($k =$

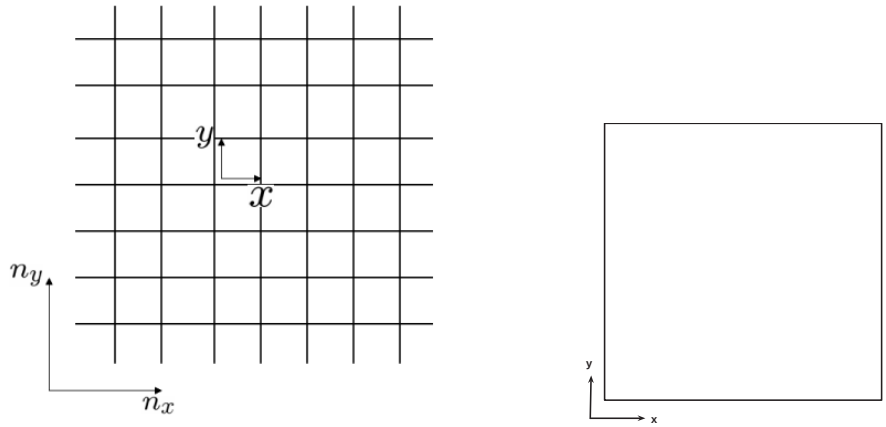

(a) Global (b) Local

Figure 10: Local and Global Coordinates in a generic 2-D periodic structure

x, y), whose real and imaginary parts are denoted respectively as 'attenuation' and 'phase' constants [32]. The propagation constants control the nature of elastic wave propagation in the 2-D assembly. If they are purely imaginary, waves are free to propagate, however if a real part exists, attenuation of the wave's amplitude will be observed as it propagates from one cell to the next. In the analysis of wave propagation in 2-D periodic structures, the attenuation constants δ_x and δ_y are typically set to 0, while the phase constants ε_x and ε_y are varied to investigate the frequencies ω at which waves propagate. This leads to the evaluation of a function $\omega = f(\varepsilon_x, \varepsilon_y)$ which defines the dispersion relations for the considered domain. These functions are known as 'phase constant surfaces' (Fig. 11) and contain a wealth of information about the wave propagation characteristics of the considered domain. They are generally represented as 3-D surfaces (Fig. 11.a) or as iso-frequency contour plots in the ε_x, ε_y plane (Fig. 11.b).

2.3 Group & Phase Velocity

The group velocity of a periodic assembly can be derived using a classical derivation which was first introduced by Stokes [33]. Consider two waves propagating at slightly differing frequencies, $\omega+\triangle\omega$ and $\omega-\triangle\omega$, in a 1-D periodic domain. For the waves to be propagating, the real part of the propagation constant, δ, is set to zero while the corresponding phase constants are given by $\varepsilon+\triangle\varepsilon$ and $\varepsilon-\triangle\varepsilon$. It is assumed that the two waves have the same

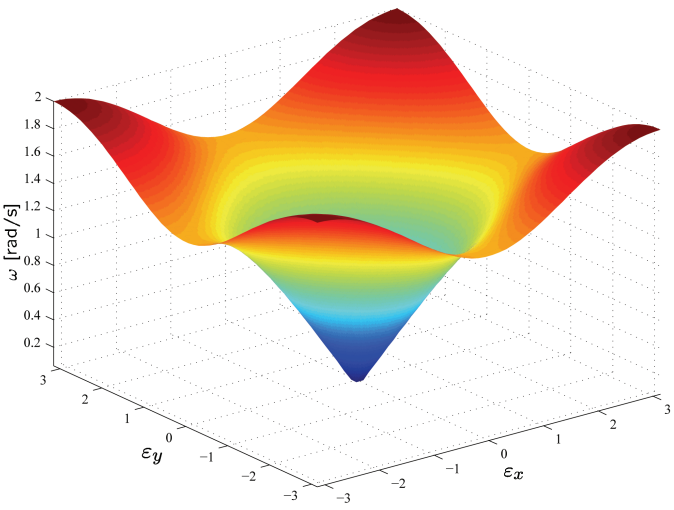

(a) 3D Surface Plot

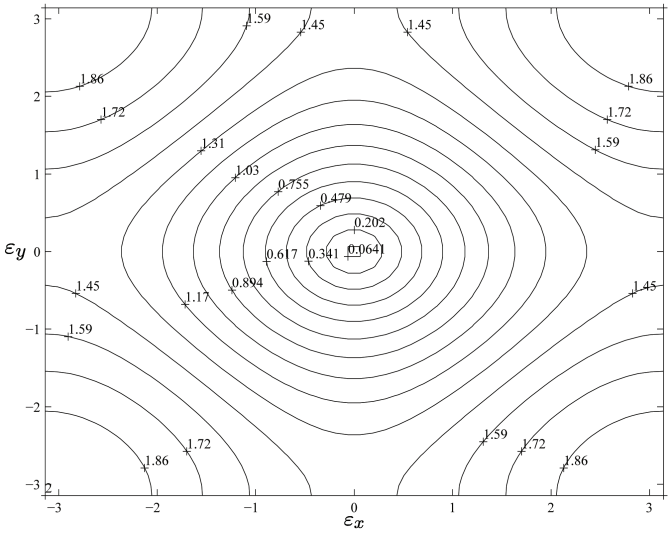

(b) 2D Contour Plot

Figure 11: Phase Constant Surfaces

amplitude w_0 and are in phase at some reference point. The motion of the structure at a location that is at a distance x from the reference point can be expressed as,

$$\begin{aligned} w(x) &= w_0 \cos[(\omega - \triangle\omega)t - (\varepsilon - \triangle\varepsilon)x/L] + w_0 \cos[(\omega + \triangle\omega)t - (\varepsilon + \triangle\varepsilon)x/L] \\ &= 2w_0 \cos(\omega t - \varepsilon x/L) \cos(\triangle\omega t - \triangle\varepsilon x/L) \\ &= 2w_0 \cos[\varepsilon/L(\omega L\ /\varepsilon t - x)] \cos[\triangle\varepsilon/L(L\triangle\omega/\triangle\varepsilon t - x)] \end{aligned} \tag{2}$$

This waveform is a modulated "carrier wave" that has a mean frequency ω and phase constant ε (Fig. 12). The spatial velocity of the modulation is $L\triangle\omega/\triangle\varepsilon$, where L is the characteristic dimension of a unit cell. By definition, this velocity approaches the group velocity c_g as $\triangle\omega$ and $\triangle\varepsilon$ tend to zero. Hence,

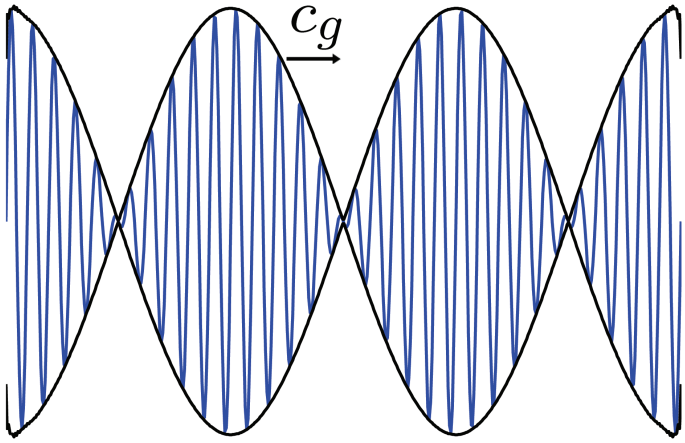

Figure 12: "Carrier" wave propagates at group velocity, c_g

$$c_g = L\partial\omega/\partial\boldsymbol{\varepsilon} \tag{3}$$

This result can be readily extended to the case of a 2-D periodic structure to obtain,

$$c_{g_x} = L_x\partial\omega/\partial\varepsilon_x, c_{g_y} = L_y\partial\omega/\partial\varepsilon_y \tag{4}$$

where L_x and L_y are the characteristic dimensions of the unit cell and c_{g_x} and c_{g_y} respectively denote the group velocity components along the x and y directions. The group

velocity for undamped structures is equal to the velocity of propagation of the vibrational energy. Brillouin [17] has verified this also holds true for 1-D periodic assemblies, and it follows from physical considerations [34] that it should hold true for all periodic structures. A proof for 2-D periodic structures will be given at the end of this chapter (see Section 2.6). This observation implies that the direction of wave propagation in a 2-D periodic assembly lies along the direction of c_{g_x} and c_{g_y}, which can be estimated by taking the normal to the iso-frequency contour lines of the phase constant surfaces. Hence, it is possible to determine the direction of wave propagation at a given frequency through the evaluation of the phase constant surfaces. This property in particular can be utilized to identify regions within the structure where waves do not propagate at certain frequencies. Specifically, the analysis of phase constant surfaces can guide the design of 2-D periodic structures where waves at certain frequencies do not propagate in specified directions.

The phase velocity of a wave in an infinite uniform 1-D structure is generally defined as $c = \omega/k$, where k is the structural wavenumber. In general, for a given wave type and frequency, k is unique apart from sign, which means that only $\pm k$ satisfies the appropriate dispersion relation. This relationship however does not hold true for periodic structures. The phase constant, ε, describes the change in phase across a discrete bay of the structure. Hence, $\varepsilon + 2\pi N$ is also a valid solution for any integer value of N. Since ε can be negative or positive, $\pm\varepsilon \pm 2\pi N$ represent all possible valid solutions that satisfy the dispersion relations. Thus, the definition of phase velocity for a periodic assembly can be arbitrarily defined as $c = \omega L/(\pm\varepsilon \pm 2\pi n)$, where L is the cell characteristic dimension. Mead [35, 36] has shown that the structural wave motion can be represented as a sum of space harmonic waves which have the wavenumbers $\varepsilon \pm 2\pi n$. This indicates that all possible phase velocities are present simultaneously, which means that a single phase velocity for wave motion in a periodic structure cannot be defined.

2.4 A Simple Example: Spring-mass Lattice

To illustrate the unique dynamic characteristics of 2-D periodic structures, a simple spring-mass lattice is first considered.

2.4.1 Lattice Description

The lattice contains two types of masses, m_1 and m_2, and features horizontal springs k_1 and vertical springs k_2 (Fig. 13.a). The unit cell (Fig. 13.b) consists of 9 masses and 12 springs. Corner and edge masses are respectively quartered and halved to obtain a doubly-symmetric unit cell, which allows reducing the computational efforts when investigating the dispersion relations. The springs on the edges of the unit cell are also halved for the same reasons. Each mass has a single degree of freedom, which is the out-of-plane displacement, and the springs apply a force which is proportional to the relative out-of-plane displacements of neighboring connected masses. This configuration is purely theoretical and is here considered as it is suitable for an analytical approach to the wave propagation formulation and to the application of Bloch's Theorem. The lattice considered in this section still allows describing the main features that characterize the dynamic behavior of 2-D periodic assemblies.

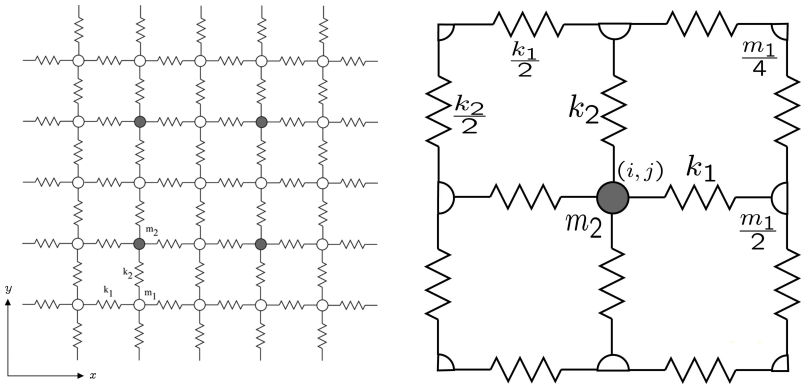

(a) Spring-mass Lattice (b) Spring-mass Unit Cell

Figure 13: Spring-mass Lattice & Cell

2.4.2 Particular Case: $m_1 = m_2$

The 2-D spring-mass system with $m_1 = m_2 = m$ is first analyzed. The unit cell for this configuration can be reduced to the configuration depicted in Fig. 14. The equation describing the harmonic motion of the mass located at location i, j can be expressed as,

$$-\omega^2 m w_{ij} + 2(k_1 + k_2)w_{ij} - k_1(w_{i,j-1} + w_{i,j+1}) - k_2(w_{i-1,j} + w_{i+1,j}) = 0 \qquad (5)$$

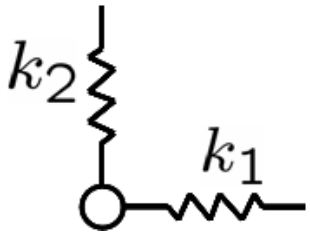

Figure 14: Spring-mass Unit Cell for $m_1 = m_2 = m$

where ω is the frequency of the harmonic motion. According to Bloch's Theorem, the following wave propagation conditions are imposed to relate the displacement of the mass at location i, j with the displacements of the neighboring masses:

$$\begin{aligned} w_{i,j-1} &= e^{-i\varepsilon_x} w_{ij} \\ w_{i,j+1} &= e^{i\varepsilon_x} w_{ij} \\ w_{i-1,j} &= e^{-i\varepsilon_y} w_{ij} \\ w_{i+1,j} &= e^{i\varepsilon_y} w_{ij} \end{aligned} \tag{6}$$

Substituting eq. (6) into eq. (5) yields,

$$\omega^2 = (2k_1/m)(1 - cos(\varepsilon_x)) + (2k_2/m)(1 - cos(\varepsilon_y)) \tag{7}$$

which represents the phase constant surface $\omega = f(\varepsilon_x, \varepsilon_y)$ for the considered lattice. It should be noted at this point that this spring mass lattice has no physical dimensions and therefore the characteristic dimensions of the unit cell are set as $L_x = L_y = 1$. The representation of eq. (7) for the configuration given in Table 1 is shown in Fig. 15 as a 2-D colormap. The phase constant surface is evidently periodic in the interval $\varepsilon_x, \varepsilon_y \in [-\pi \;\; \pi]$. Also, within one period, it is symmetric with respect to the axes along $\varepsilon_x = 0$ and $\varepsilon_y = 0$. Symmetry and periodicity of the phase constant surface allow restricting the analysis of the dispersion characteristics of the lattice to the area $\varepsilon_x, \varepsilon_y \in [0 \;\; \pi]$, highlighted in Fig. 15 by a white rectangle. This area can be identified for all periodic lattices and it is denoted as "first Brillouin zone" [17]. The contour plot of the phase constant surface in the first Brillouin zone

is shown in Fig. 16. This representation is particularly convenient as it allows visualizing the direction of the energy flow from the evaluation of the perpendicular directions to the iso-frequency lines, as discussed in Section 2.3. In this regard, this simple lattice configuration shows very interesting characteristics. The iso-frequency contour corresponding to $\omega = 1.41$ rad/s is in fact a straight line, whose perpendicular direction is always directed along the diagonal at $+45^o$ for all combinations of the propagation constants. This indicates that the energy flow of a wave propagating through the lattice at $\omega = 1.41$ rad/s occurs exclusively along the diagonal direction. On the contrary at all other frequencies, the energy flow spans several directions depending on the $\varepsilon_x, \varepsilon_y$ combinations. The visualization of this behavior is facilitated in Fig. 16 by representing the energy flow at two frequency values through arrows pointing in the corresponding direction. This phenomenon, whereby wave propagation at certain frequency is restricted to only certain directions, is here denoted as the "directional behavior" or "directionality" of 2-D periodic structures.

Table 1: Unit Cell Configuration for $m_1 = m_2$, $k_1 = k_2$

Property	Value	Units
m_1	1	kg
m_2	1	kg
k_1	0.5	N/m
k_2	0.5	N/m

The predictions from the analysis of the phase constant surface and associated energy flow considerations can be readily verified through the computation of the harmonic response of a finite lattice. The dynamic behavior of the lattice can be described in the following well-known matrix notation:

$$(\boldsymbol{K} - \omega^2 \boldsymbol{M})\underline{u} = \underline{F} \tag{8}$$

where $\boldsymbol{K}, \boldsymbol{M}$ are respectively the stiffness and mass matrices of the lattice, while $\underline{u}$ and $\underline{F}$ are vectors containing the out-of-plane displacements and forces on the masses. In here the harmonic response of a lattice composed of a 11×11 grid of masses is evaluated. The

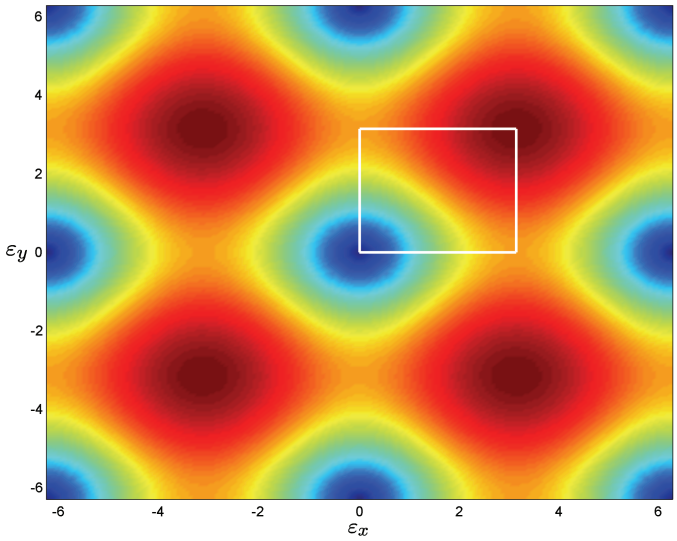

Figure 15: Phase Constant Surface for ε_x & ε_y from -2π to 2π

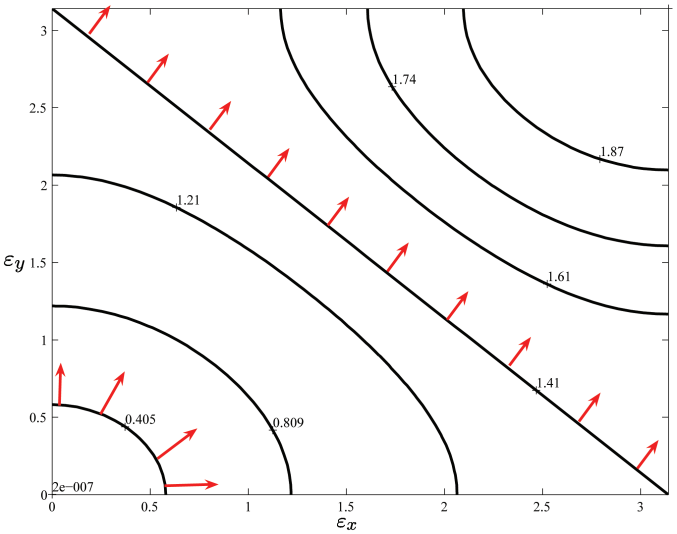

Figure 16: Phase Constant Surface: $2k_1/m = 2k_2/m = 1.0$

lattice is excited by a force of unit amplitude and varying frequency applied at the center of the lattice. The responses at 1.20 rad/s, 1.41 rad/s and 1.60 rad/s are shown in Fig. 17 as an interpolated color map plot of the out-of-plane displacements. The computed response of the system is symmetric, but there is a small asymmetry introduced in the color map plots due to the interpolation routines used. It is evident that the wave propagation occurs in all directions at 1.20 rad/s and 1.60 rad/s (Figs. 17.a and 17.c), while at 1.41 rad/s, vibrations are only restricted to the direction predicted by the phase constant surface.

The directional behavior of the lattice with $k_1 = k_2$ only occurs at a specific value of the frequency $\omega = 1.41$ rad/s. However, it can be shown that lattices with $k_1 \neq k_2$ feature directionality over a wider frequency band. The phase constant surface for the unit cell configuration described in Table 2 is shown for example in Fig. 18. The corresponding contour plot highlights the presence of a frequency range where the perpendicular to the iso-frequency lines spans only a limit angular range. For the considered configuration, this range spans frequencies between approximately 1.41 and 1.92 rad/s. Within this frequency range, wave propagation is expected to occur over limited angles centered along the y direction. These indications are confirmed by the analysis of the harmonic response of the lattice. Fig. 19.a demonstrates for example how no attenuation is observed in the response at 0.80 rad/s, while for $\omega = 1.60$ rad/s, energy flow can only be observed along an angular range centered along the vertical direction. The extension of the angular range corresponds to the one predicted by the phase constant surface analysis.

Table 2: Unit Cell Configuration for $m_1 = m_2$, $k_1 \neq k_2$

Property	Value	Units
m_1	1	kg
m_2	1	kg
k_1	0.5	N/m
k_2	1	N/m

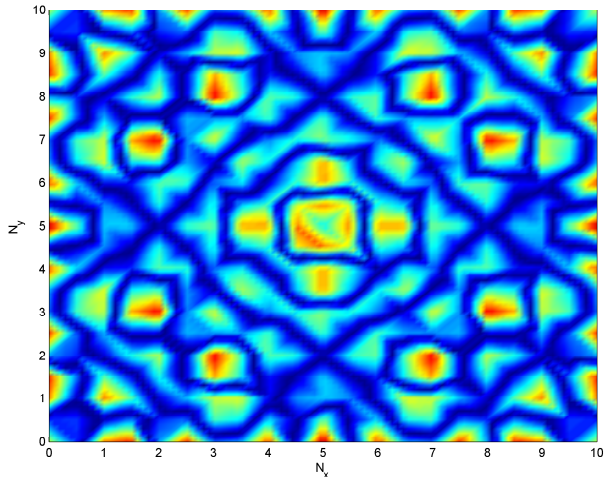

(a) $\omega = 1.20$ rad/s

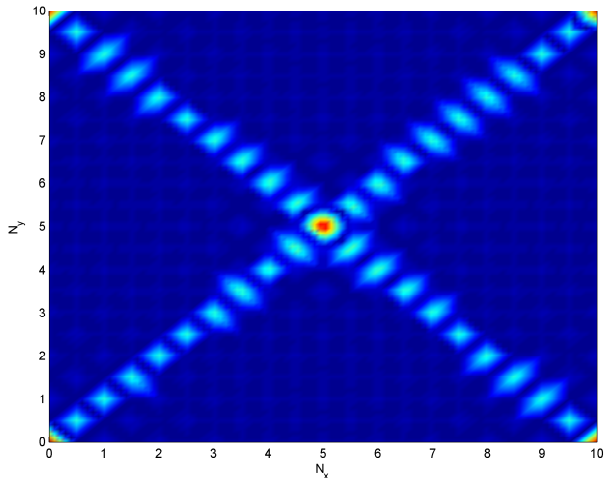

(b) $\omega = 1.41$ rad/s

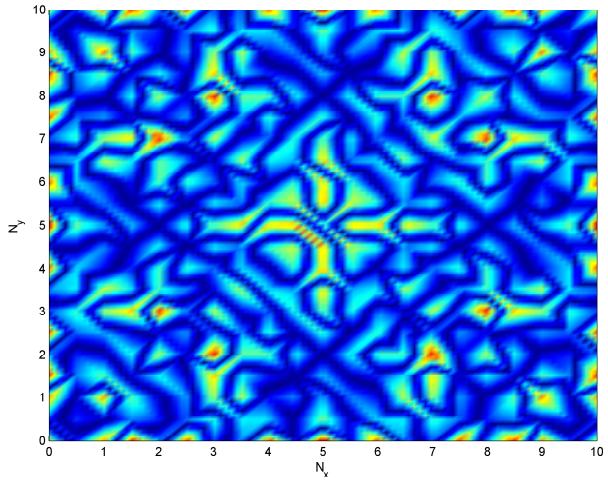

(c) $\omega = 1.60$ rad/s

Figure 17: Harmonic Response of Spring-Mass Lattice

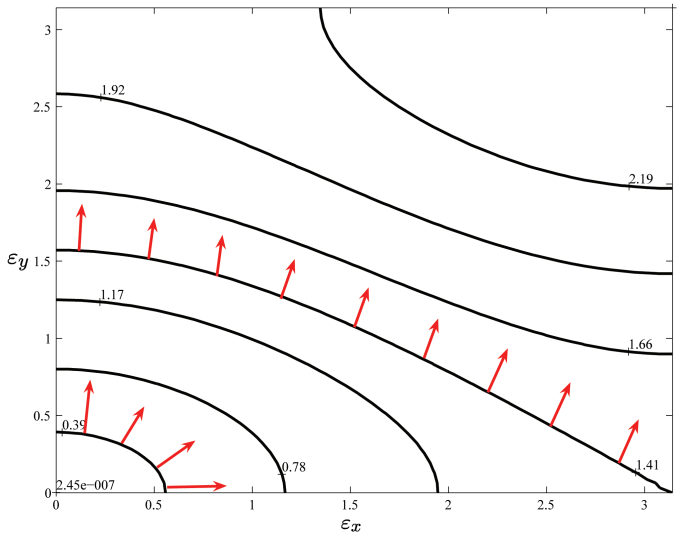

Figure 18: Phase Constant Surface: $2k_1/m = 1.0, 2k_2/m = 2.0$

2.5 Spring-mass lattice with a "hard" inclusion

In the general case where $m_1 \neq m_2$, the unit cell shown in Fig. 20.a needs to be considered. The dynamic behavior of the cell can be conveniently described in matrix form through an equation of the form of eq. (8). This more general configuration for the spring mass lattice is commonly considered in the literature as a simple model for a crystal lattice with inclusions. The lattice is here introduced to illustrate another unique characteristic of the dynamic behavior of periodic assemblies. Periodic structures in general feature frequency bands where waves are attenuated in all directions, so that perturbations remain localized to the region near the point of excitation. These frequency bands are known as "band-gaps" or "stop-bands". The stop-bands are in general identified as gaps in frequency occurring between subsequent phase constant surfaces of a multi-degree of freedom periodic domain. For 2-D periodic structures, their identification is facilitated by the application of a method which reduces the computational cost of the procedure and allows a clear representation for the stop-bands. The concept of stop-bands and their evaluation in the case of 2-D periodic domains is described in the following sections.

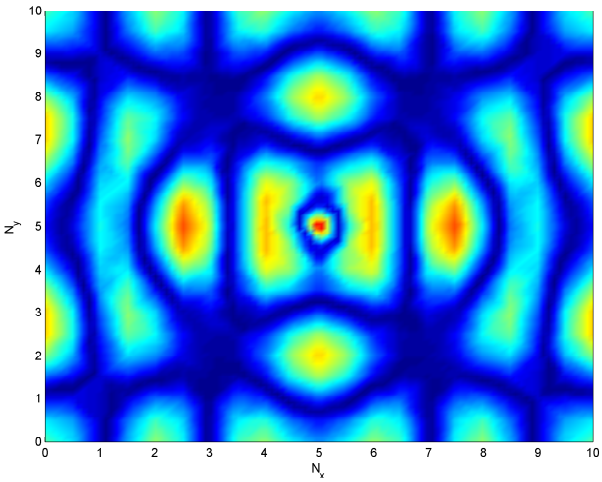

(a) $\omega = 0.80$ rad/s

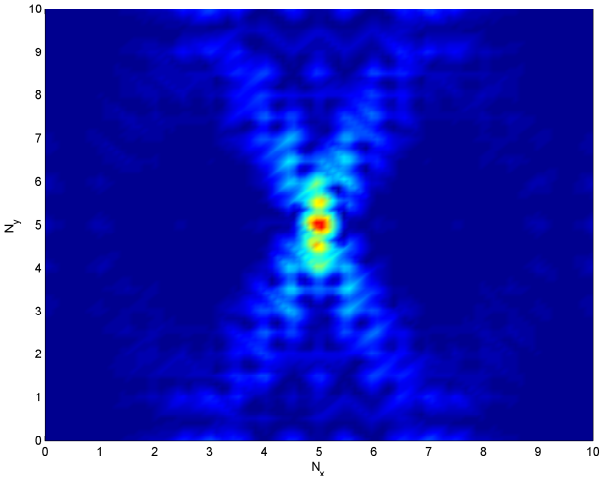

(b) $\omega = 1.60$ rad/s

Figure 19: Harmonic Response: $2k_1/m = 1.0, 2k_2/m = 2.0$

2.5.1 Bloch Reduction

For wave motion at frequency ω, the relation between the cell's displacements and the forces of interaction with the neighboring cells can be generally expressed as:

$$\Big(\boldsymbol{K} - \omega^2 \boldsymbol{M}\Big)\underline{\delta} = \underline{F} \tag{9}$$

where $\boldsymbol{K}$ and $\boldsymbol{M}$ are the cell's mass and stiffness matrices, and $\underline{\delta}$, $\underline{F}$ are respectively the vectors containing nodal displacements and forces at the cell boundaries (see Fig. 20). It should be observed how this formulation can be used for any generic periodic domain, where the behavior of the cell is described through a finite element formulation. The derivations that follow hence apply to a generic 2-D periodic assembly, whose unit cell can be represented according to the configuration shown in Fig. 20. The vector of the cell's degrees of freedom is organized as follows:

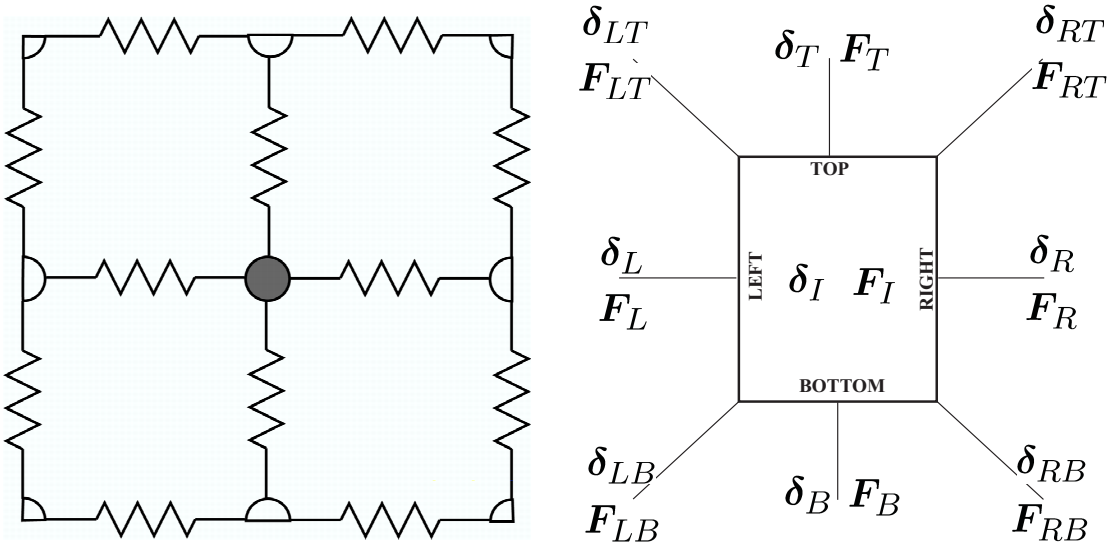

(a) Spring-mass cell (b) Generic representation of a unit cell

Figure 20: Generalized boundary nodal displacements and forces

$$\underline{\delta} = \{\ \underline{\delta}_L^T \quad \underline{\delta}_R^T \quad \underline{\delta}_T^T \quad \underline{\delta}_B^T \quad \underline{\delta}_{LB}^T \quad \underline{\delta}_{LT}^T \quad \underline{\delta}_{RT}^T \quad \underline{\delta}_{RB}^T \quad \underline{\delta}_I^T\ \}^T \tag{10}$$

where R, L, T, B respectively indicate right, left, top and bottom boundaries, while I denotes the degrees of freedom internal to the cell. Similarly, the vector of the forces is expressed

as:

$$\underline{F} = \{ \ \underline{F}_L^T \quad \underline{F}_R^T \quad \underline{F}_T^T \quad \underline{F}_B^T \quad \underline{F}_{LB}^T \quad \underline{F}_{LT}^T \quad \underline{F}_{RT}^T \quad \underline{F}_{RB}^T \quad \underline{F}_I^T \ \}^T \tag{11}$$

According to Bloch's Theorem, the generalized displacements and forces at the cell interfaces are related by:

$$\begin{aligned} \underline{\delta}_R &= e^{\mu_x} \underline{\delta}_L \\ \underline{\delta}_T &= e^{\mu_y} \underline{\delta}_B \\ \underline{\delta}_{LT} &= e^{\mu_y} \underline{\delta}_{LB} \\ \underline{\delta}_{RT} &= e^{\mu_x + \mu_y} \underline{\delta}_{LB} \\ \underline{\delta}_{RB} &= e^{\mu_x} \underline{\delta}_{LB} \end{aligned} \tag{12}$$

and

$$\begin{aligned} \underline{F}_R &= -e^{\mu_x} \underline{F}_L \\ \underline{F}_T &= -e^{\mu_y} \underline{F}_B \\ \underline{F}_{LT} &= -e^{\mu_y} \underline{F}_{LB} \\ \underline{F}_{RT} &= -e^{\mu_x + \mu_y} \underline{F}_{LB} \\ \underline{F}_{RB} &= -e^{\mu_x} \underline{F}_{LB} \end{aligned} \tag{13}$$

Eqs. (12) and (13) can be rewritten in matrix form as follows:

$$\underline{\delta} = \boldsymbol{A} \underline{\delta}_r \tag{14}$$

$$\underline{F} = \boldsymbol{B} \underline{F}_r \tag{15}$$

$$\tag{16}$$

where

$$\underline{\delta}_r = \{\ \underline{\delta}_L^T, \underline{\delta}_B^T, \underline{\delta}_{LB}^T, \underline{\delta}_I^T\ \}^T$$

while $\boldsymbol{A}$ and $\boldsymbol{B}$ are matrices defined as follows,

$$\boldsymbol{A} = \begin{bmatrix} \boldsymbol{I}_L & 0 & 0 & 0 \\ \boldsymbol{I}_R e^{\mu_x} & 0 & 0 & 0 \\ 0 & \boldsymbol{I}_T e^{\mu_y} & 0 & 0 \\ 0 & \boldsymbol{I}_B & 0 & 0 \\ 0 & 0 & \boldsymbol{I}_{LB} & 0 \\ 0 & 0 & \boldsymbol{I}_{LT} e^{\mu_y} & 0 \\ 0 & 0 & \boldsymbol{I}_{RT} e^{\mu_x+\mu_y} & 0 \\ 0 & 0 & \boldsymbol{I}_{RB} e^{\mu_x} & 0 \\ 0 & 0 & 0 & \boldsymbol{I}_I \end{bmatrix} \tag{17}$$

$$\boldsymbol{B} = \begin{bmatrix} \boldsymbol{I}_L & 0 & 0 & 0 \\ -\boldsymbol{I}_R e^{\mu_x} & 0 & 0 & 0 \\ 0 & -\boldsymbol{I}_T e^{\mu_y} & 0 & 0 \\ 0 & \boldsymbol{I}_B & 0 & 0 \\ 0 & 0 & \boldsymbol{I}_{LB} & 0 \\ 0 & 0 & -\boldsymbol{I}_{LT} e^{\mu_y} & 0 \\ 0 & 0 & -\boldsymbol{I}_{RT} e^{\mu_x+\mu_y} & 0 \\ 0 & 0 & -\boldsymbol{I}_{RB} e^{\mu_x} & 0 \\ 0 & 0 & 0 & \boldsymbol{I}_I \end{bmatrix} \tag{18}$$

where $\boldsymbol{I}_L$, $\boldsymbol{I}_R$, $\boldsymbol{I}_T$, $\boldsymbol{I}_B$, $\boldsymbol{I}_{LB}$, $\boldsymbol{I}_{LT}$, $\boldsymbol{I}_{RT}$, $\boldsymbol{I}_{RB}$, and $\boldsymbol{I}_I$ are identity matrices of size corresponding to the degrees of freedoms at the boundaries and the interior of the cell. Substituting eq. (12) into eq. (9), pre-multiplying the resulting equations by $\boldsymbol{A}^H$, with H denoting a complex transpose conjugate, and assuming $\underline{F}_I = 0$ gives:

$$(\boldsymbol{K_r} - \omega^2 \boldsymbol{M_r})\underline{\delta}_r = \underline{0} \tag{19}$$

where,

$$\boldsymbol{K_r} = \boldsymbol{A}^H \boldsymbol{K} \boldsymbol{A} \tag{20}$$

$$\boldsymbol{M_r} = \boldsymbol{A}^H \boldsymbol{M} \boldsymbol{A} \tag{21}$$

are stiffness and mass matrices reduced according to Bloch's theorem. Eq. (19) is an eigenvalue problem whose solution in terms of frequency ω can be obtained by imposing ε_x and ε_y. In other words, eq. (19) defines the dispersion relations of the system. Varying ε_x and ε_y from 0 to π and assuming the attenuation constants to be zero, generates the phase constant surfaces in the first Brillouin zone [17] for a given cell (Fig. 11).

2.5.2 First Brioullin zone and dispersion relations

The methodology outlined above yields the phase constant surfaces for the unit cell of a periodic structure. In particular, for the spring mass lattice shown in Fig. 20.a, the procedure yields 4 phase constant surfaces. The 3-D representation of the phase constant surfaces for $m_2 = 2m_1$ and $k_1 = k_2$ is shown in Fig. 21. The 2-D color map of the first phase constant surface is instead displayed in Fig. 22.a to highlight its periodicity and symmetry over the $[-\pi, \pi]$ interval. The wave propagation characteristics of a 2-D periodic structure can be alternatively analyzed by evaluating the phase constant surfaces for phase constants varying only along the boundary of the first Brillouin zone. This leads to a 1-D representation of the dispersion relation for the domain, which provides a compact representation of the behavior of the lattice. The boundaries of the first Brillouin zone are highlighted in Fig. 22.a by a triangle. For the particular lattice configuration here considered, the phase constant surfaces are in fact symmetric about a 45° line which allows a further reduction of the dispersion relation by considering phase constant pairs varying only along the contour $M \rightarrow \Gamma \rightarrow X \rightarrow M$ shown in Fig. 22.b. The reduced contour defines the so-called first irreducible Brillouin zone, which can be identified for all lattices showing a symmetry of the kind here described. The dispersion relation for the configuration listed in Table 3 is shown in Fig. 23.

Table 3: Unit Cell Configuration for $m_1 \neq m_2$, $k_1 = k_2$

Property	Value	Units
m_1	1	kg
m_2	3	kg
k_1	0.5	N/m
k_2	0.5	N/m

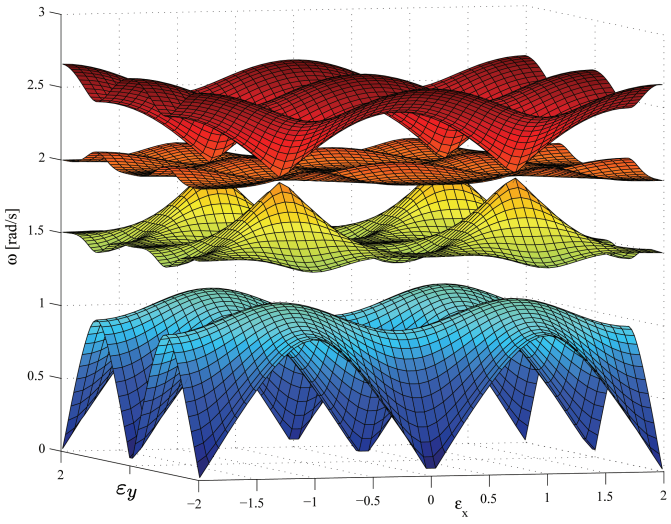

Figure 21: 3-D Phase Constant Surfaces

2.5.3 Band-gap behavior

The 3-D representation of the phase constant surfaces in Fig. 21 shows a gap between the first and second phase constant surfaces. This indicates that, over the corresponding frequency range, there are no associated values for the phase constants, and therefore that waves do not propagate within the lattice. From this analysis, it is therefore possible to determine the regions over which wave propagation is permitted and other regions where waves are attenuated at any given frequency. However, it may be computationally intensive and difficult to discern this information from the 3-D phase constant surfaces. The compact representation of the dispersion relation instead provides a clear indication of the frequency range where attenuation occurs. This frequency range is called stop-band, or band-gap.

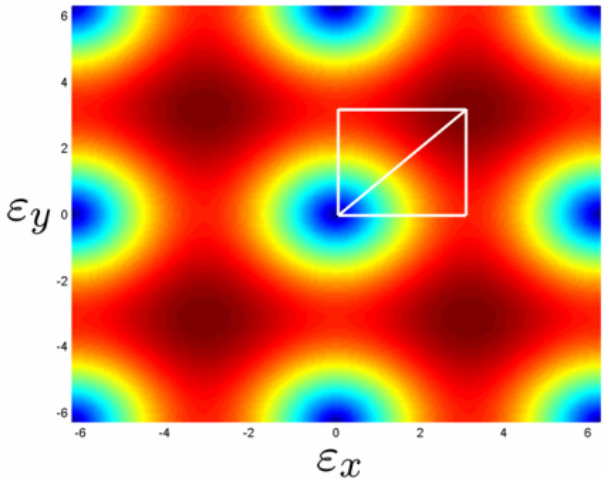

(a) Brillouin Zone

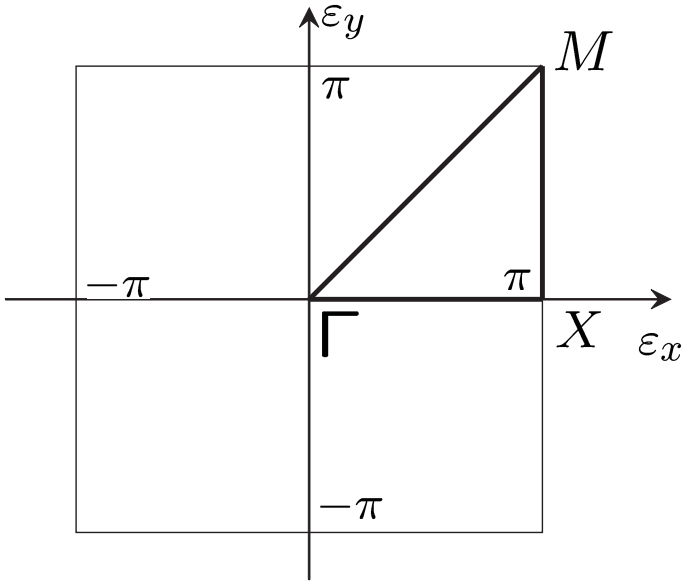

(b) Irreducible Brillouin Zone

Figure 22: First Brillouin Zone

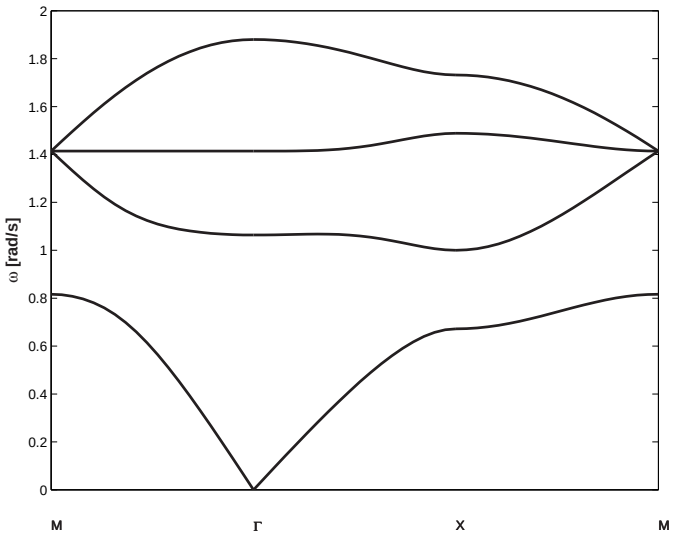

Figure 23: Spring-Mass System: Dispersion Relations

Plots of the kind of Fig. 23 clearly highlight the extension and the location of the band-gap, which, for this configuration, includes frequencies belonging to the range between 0.8 and 1.0 rad/s. The procedure for the reduction of the dispersion relations by varying the propagation parameters along the contour of the Brioullin zone is widely accepted in the literature, although a formal proof demonstrating its accuracy has never been presented. The band-gap behavior for the lattice is associated to the presence of the mass $m_2 \neq m_1$ at the center of each unit cell. The mass generates an impedance mismatch which partially reflects the incident wave. Proper interaction between incident and reflected waves produces destructive interference which is responsible for the attenuation of waves within the lattice. The occurrence of the band-gap corresponds to an internal resonance of the unit cell, as shown by Jensen [37]. For the simple lattice considered in this section, the internal resonance can be predicted simply by computing the resonant frequency of the internal mass m_2 relative to the surrounding masses. This resonance frequency is evaluated by considering all masses m_1 fixed, so that the unit cell reduces to a single degree of freedom oscillator of mass m_2 suspended by a series of 4 springs $k_1 = k_2 = k$. The corresponding resonant frequency is therefore given by:

$$\omega_0 = 2\sqrt{\frac{k}{m_2}} \tag{22}$$

Examples of dispersion relations for various values of the ratio m_2/m_1 and for $k_1 = k_2$ are shown in Fig. 24. In the plots, the frequency axis is normalized to the value of ω_0 defined in eq. (22), which describes the beginning of the band-gap. Different mass values generate band-gaps of different width and location. In all cases, the lower bound for the band-gaps coincides with the value of frequency defined in eq. (22), which corresponds to a value of the non-dimensional frequency parameter $\Omega = \omega/\omega_0$ equal to 1. Furthermore, it may be shown how the top boundary of the band-gap corresponds to the out-of-phase motion of internal and external masses [37]. This frequency can be predicted by computing the natural frequency of the unit cell associated to a mode with opposition of phase between the masses m_1 and m_2. The mode shape of the unit cell corresponding to the upper bound frequency of the band-gap is shown in Fig. 25 for a configuration with $m_2 = 3m_1$.

2.5.4 Harmonic response of a finite lattice

The band-gap behavior is analyzed through the evaluation of the harmonic response of a finite lattice with $m_2 = 2m_1$ (Table 3). The lattice is made up of 10 unit cells in the x and y direction, with 341 masses (m_1) and 100 "hard" inclusions (m_2). An out of plane point load is applied at the center of the lattice and the harmonic response is computed. The response of the lattice at three different frequencies is shown in Fig. 26. Frequencies $\omega = 0.7$ and $\omega = 1.4$ rad/s are respectively below and above the predicted band-gap, while $\omega = 0.9$ rad/s is approximately at the middle of the range of attenuation. Fig. 26.a and Fig. 26.c show how the applied perturbation is free to propagate in all directions, while Fig. 26.b clearly demonstrates how within the band-gap, the vibrations of the structure are localized to the immediate area around the point of loading. Waves are otherwise attenuated in all directions.

Another effective way of verifying the prediction from the dispersion analysis is to evaluate the frequency response of the lattice at various locations. The lattice is excited at the lower left corner, and the frequency response at the upper left, upper right and lower right

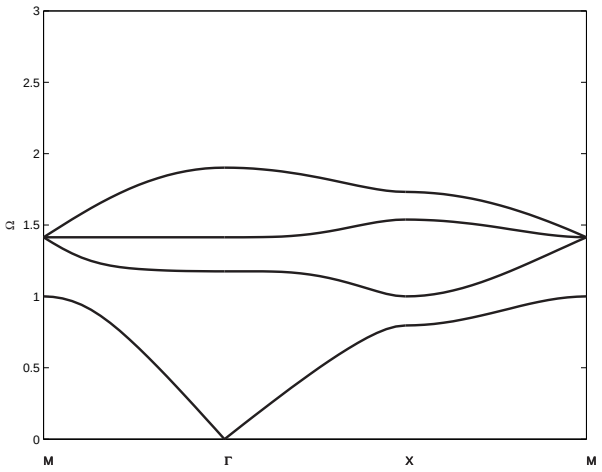

(a) $m_2/m_1 = 2$

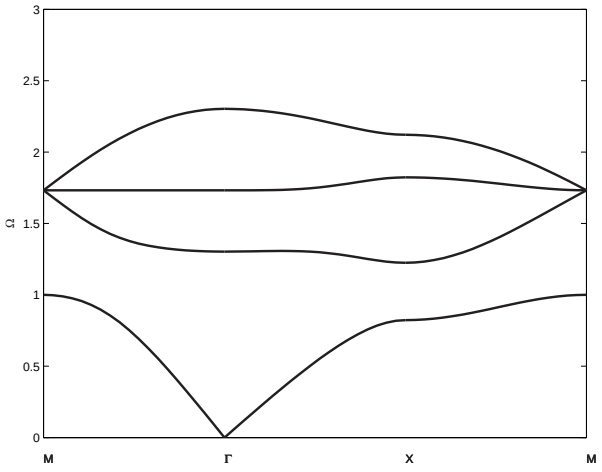

(b) $m_2/m_1 = 3$

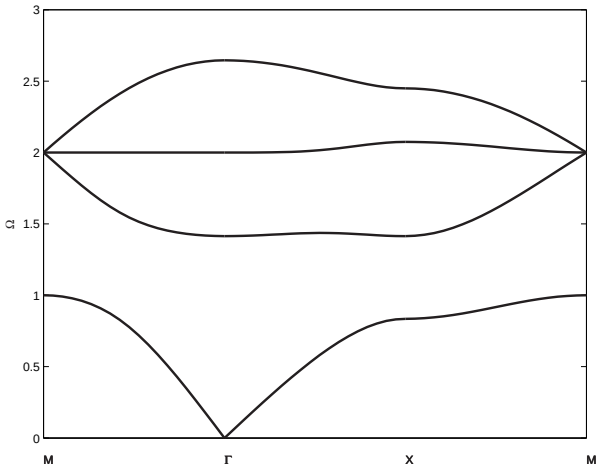

(c) $m_2/m_1 = 4$

Figure 24: Dispersion relations for various values of the internal mass

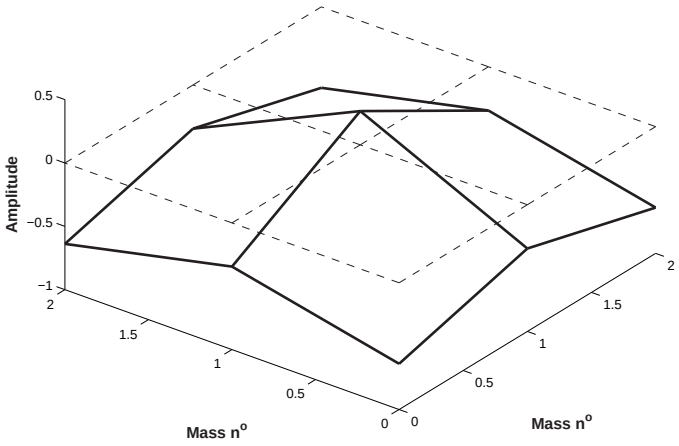

Figure 25: Unit cell mode corresponding to upper bound of band-gap

corner is evaluated to investigate how the excitation propagates along 3 directions within the structure. The configuration considered for this numerical test is depicted schematically in Fig. 27, while the frequency response at each of the three corners is shown in Fig. 28. The response at the upper left and upper right corners are identical because of lattice symmetry. Band-gaps can be identified when a noticeable drop in amplitude over a frequency range is observed at all three locations. For the spring-mass system, this occurs between 0.8 and 1.0 rad/s, which is in agreement with the prediction obtained from the dispersion relations.

The methodology used here to study the spring-mass system can be extended to study more general structures. The finite element formulation needed to analyze more general assemblies is detailed in Chapter 3. Finite element theory and the methodology introduced here are combined, and the dynamic characteristics of a rectangular lattice are analyzed in Chapter 4.

2.6 Energy Velocity

In this section the equality of the group velocity and energy velocity is demonstrated. For wave propagation to occur, the propagation constants μ_x and μ_y must be purely imaginary. If that is the case, then the matrices $\boldsymbol{A}$ and $\boldsymbol{B}$ have the property,

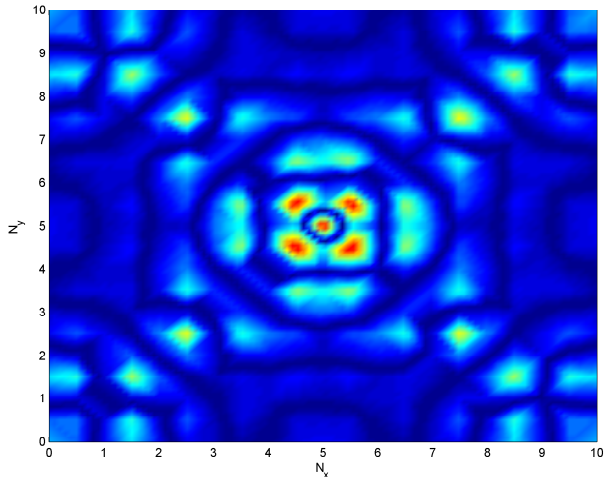

(a) $\omega = 0.70$ rad/s

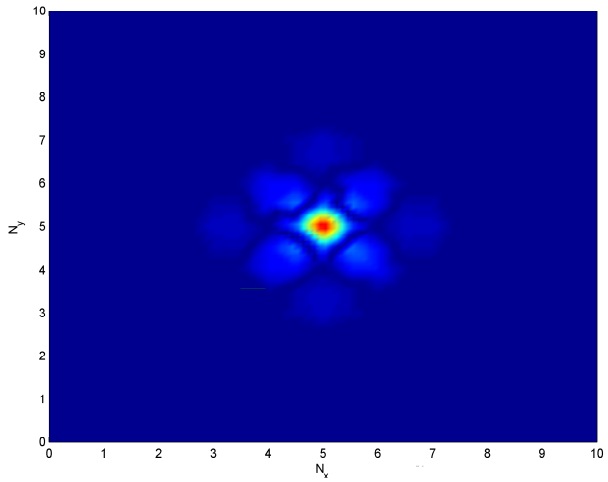

(b) $\omega = 0.90$ rad/s

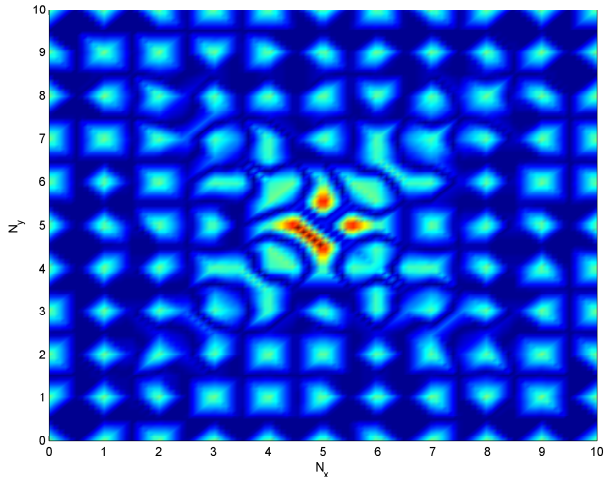

(c) $\omega = 1.40$ rad/s

Figure 26: Amplitude of harmonic response of spring mass lattice at various frequencies

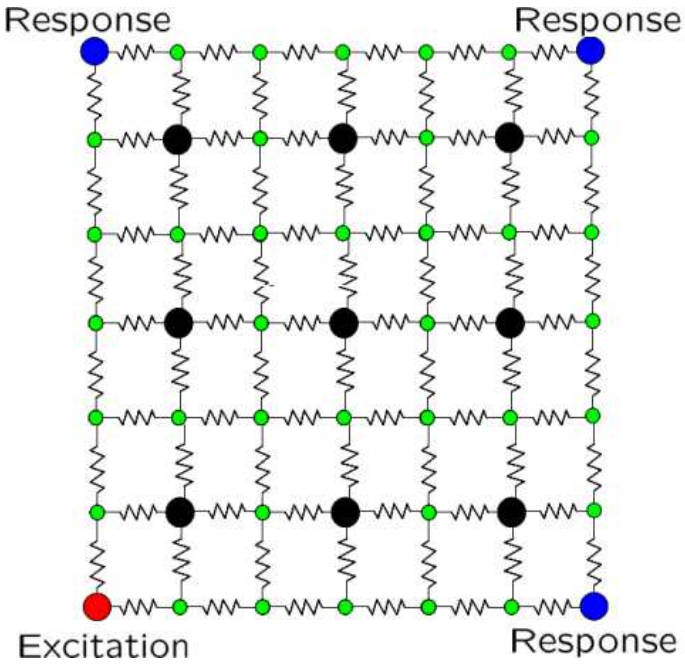

Figure 27: Excitation and Response Schematic

$$\boldsymbol{A}^H \boldsymbol{B} = \boldsymbol{0} \tag{23}$$

Consider a 2-D cell with no "corner" degrees if freedom, so $\underline{\delta}$, $\underline{F}$, $\boldsymbol{A}$ and $\boldsymbol{B}$ are simplified from eqs. (10), (11), (17) and (18) to,

$$\underline{\delta} = \{ \begin{array}{ccccc} \underline{\delta}_L^T & \underline{\delta}_R^T & \underline{\delta}_T^T & \underline{\delta}_B^T & \underline{\delta}_I^T \end{array} \}^T \tag{24}$$

$$\underline{F} = \{ \begin{array}{ccccc} \underline{F}_L^T & \underline{F}_R^T & \underline{F}_T^T & \underline{F}_B^T & \underline{F}_I^T \end{array} \}^T \tag{25}$$

$$\boldsymbol{A} = \begin{bmatrix} \boldsymbol{I}_L & 0 & 0 \\ \boldsymbol{I}_R e^{\mu_x} & 0 & 0 \\ 0 & \boldsymbol{I}_T e^{\mu_y} & 0 \\ 0 & \boldsymbol{I}_B & 0 \\ 0 & 0 & \boldsymbol{I}_I \end{bmatrix} \tag{26}$$

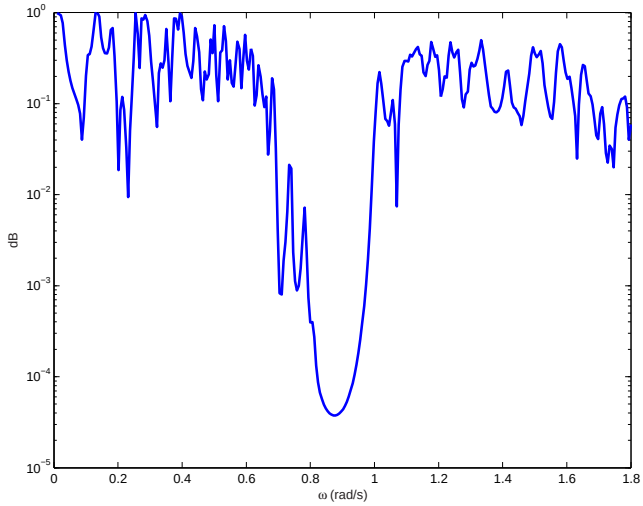

(a) Upper Left

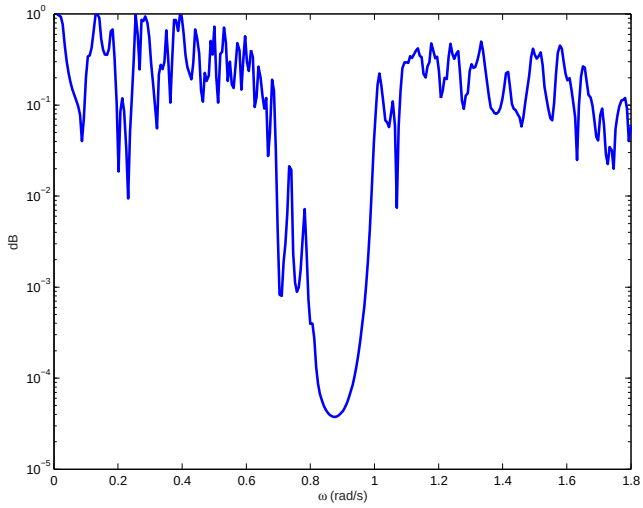

(b) Lower Right

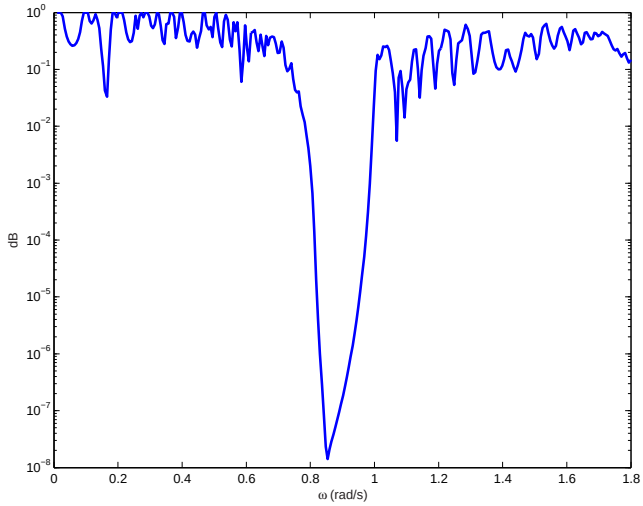

(c) Upper Right

Figure 28: Frequency Response of the other three Corners

$$\boldsymbol{B} = \begin{bmatrix} \boldsymbol{I}_L & 0 & 0 \\ -\boldsymbol{I}_R e^{\mu_x} & 0 & 0 \\ 0 & -\boldsymbol{I}_T e^{\mu_y} & 0 \\ 0 & \boldsymbol{I}_B & 0 \\ 0 & 0 & \boldsymbol{I}_I \end{bmatrix} \tag{27}$$

The equation of motion for a single cell is given by eq. (9), and it follows directly that,

$$\underline{\delta}^T(\boldsymbol{K} - \omega^2 \boldsymbol{M})\underline{\delta} = \underline{\delta}^T \underline{F} \tag{28}$$

Eq. (28) may be used to investigate the effect on frequency of a small change in one of the propagation constants. Upon letting $\triangle v$ represent the change induced in a general quantity v, it follows that,

$$\triangle\underline{\delta}^T(\boldsymbol{K} - \omega^2 \boldsymbol{M})\underline{\delta} + \underline{\delta}^T(\boldsymbol{K} - \omega^2 \boldsymbol{M})\ \triangle\underline{\delta} - 2\omega\ \triangle\omega\underline{\delta}^T \boldsymbol{M}\underline{\delta} = \triangle\underline{\delta}^T \underline{F} + \underline{\delta}^T\ \triangle\underline{F} \tag{29}$$

Using eqs. (9), this can be simplified to,

$$2\omega\ \triangle\omega\underline{\delta}^T \boldsymbol{M}\underline{\delta} = \underline{F}^T\ \triangle\underline{\delta} + \underline{\delta}^T\ \triangle\underline{F} \tag{30}$$

The right hand side of eq. (30) can be expressed in a more convenient form using eqs. (26), (27) and (14),

$$2\omega\triangle\omega\underline{\delta}^T \boldsymbol{M}\underline{\delta} = \underline{F}^T\triangle\boldsymbol{A}\underline{\delta}_r - \underline{\delta}^T\triangle\boldsymbol{B}\underline{F}_r \tag{31}$$

where $\underline{\delta}_r$ and $\underline{F}_r$ are the reduced generalized displacements and forces. If the change is brought about by a small change in $\triangle\varepsilon_x$ then it follows from eq.(26) that the only non-zero term in $\triangle\boldsymbol{A}$ is $\triangle A_{21} = -i\triangle\,\varepsilon_x e^{-\mu_x}$. Similarly, eq.(27) implies that the only non-zero term in $\triangle\boldsymbol{B}$ is $\triangle B_{21} = -i\triangle\,\varepsilon_x e^{-\mu_x}$. Hence, the right hand side of eq. (31) can be simplified to,

$$\begin{aligned} \underline{F}^T\triangle\boldsymbol{A}\underline{\delta}_r &= i\triangle\varepsilon_x \underline{F}_L^T\underline{\delta}_L \\ \underline{\delta}^T\triangle\boldsymbol{B}\underline{F}_r &= i\triangle\varepsilon_x \underline{\delta}_L^T\underline{F}_L \end{aligned} \tag{32}$$

so that eq. (31) becomes,

$$\omega \triangle \omega \underline{\delta}^T \boldsymbol{M} \underline{\delta} = -i \triangle \varepsilon_x Re(i \underline{\delta}_L^T \underline{F}_L) \tag{33}$$

where $Re(v)$ is the real part of the quantity v. In the limit as $\triangle \varepsilon_x \to 0$ this result yields,

$$L_x \partial \omega / \partial \varepsilon_x = -(1/2) Re(i \omega \underline{\delta}_L^T \underline{F}_L) / ((1/2 L_x) \omega^2 \underline{\delta}^T \boldsymbol{M} \underline{\delta}) \tag{34}$$

The right hand side of the equation represents the time average of the energy flow across the left boundary of the cell over the time average of the total energy stored in the cell per unit length (total energy = 2 $\times$ kinetic energy) in the x-direction. Hence, the right hand side of the equation is simply the energy velocity in the x-direction, while the left hand side is the group velocity component in that direction. The equality of these two quantities is demonstrated and can be extended to show the equality in the y-direction.

CHAPTER III

MODELING OF GENERAL LATTICE CONFIGURATIONS

3.1 Overview

The focus of this dissertation is the analysis of the vibration of general lattice assemblies. Examples of the considered configurations are shown in Fig. 29. These structures can all be considered as obtained by the assembly of beam elements, connected either through spherical joints allowing relative rotations, or through rigid joints. In the latter case, the structures can be properly denoted as frames. The analysis of the variety of structures depicted in Fig. 29 requires the formulation of a general beam element. The element should be able to describe three-dimensional displacements, and should be assembled according to a general topology. In addition, the lattice element may be developed along flat or curved surfaces as in the case of the cylindrical grids shown in Fig 29.b.

A general curved beam element is used to model the unit cells of all lattice configurations considered in this work. This beam element, originally introduced by K.J. Bathe [38], represents an improvement with respect to beam elements available in most commercially available software packages, which mostly only support straight beams. The in-house development of the element is also motivated by the fact that the application of Bloch Theorem cannot rely on the solver capabilities of commercial FE packages. In this regards, limitations of commercial software are associated with the application of periodic boundary conditions and with the solution of a complex eigenvalue problem resulting from the application of Bloch's Theorem. In addition, the description of curved surfaces and their approximation with a large number of straight beam elements would imply a high computational cost together with strict aspect ratio limitations.

Computing the response using of such lattice structures conventional FE methods can also prove to be a costly task, particularly if higher frequency analysis is required. This computational burden is reduced through two techniques developed in this research. The first technique consists in exploiting the rotational periodicity in cylindrical grid structures,

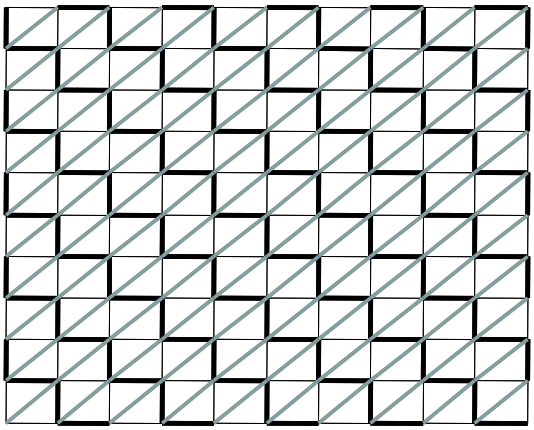

(a) Rectangular Grid

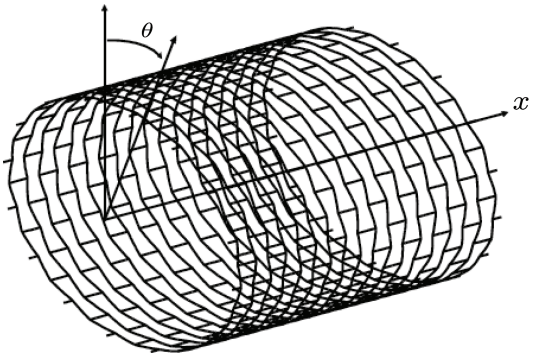

(b) Hexagonal Cylindrical Grid

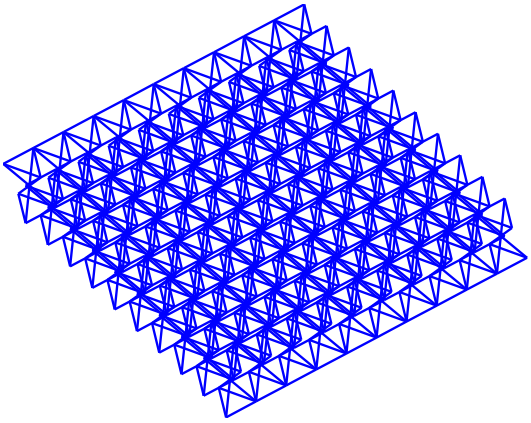

(c) Kagomé Grid

Figure 29: Considered Configurations

whereby the response of a single periodic strip can be computed and the solution extended to find the response of the complete cylinder. This methodology is discussed in Chapter 6. When such rotational periodicity does not exist, Spectral Finite Elements [39] are instead used to describe the harmonic response of lattice structures. The spectral finite element formulation is described in Section 3.4.

3.2 Curved beam element

The formulation of a general curved beam element is primarily complicated by two difficulties: the interpolation of the curved geometry to the beam displacements and the phenomenon of membrane locking [40]. The first difficulty is handled by the careful selection of the coordinate and displacement functions so that the resulting Jacobian can relate the curvilinear geometry to the global coordinate system, and the natural coordinates to the curvilinear geometry. Membrane locking occurs because of the inextensibility condition of the membrane strain when the thickness of the curved beam element approaches zero. Numerical evidence shows that if this phenomenon is not handled appropriately, the resulting element is much too stiff to be of any use. Results as bad as only predicting 5% of the actual displacements are possible if membrane locking is not handled in the formulation [38]. However, in the case of very shallow or straight beam elements, this phenomenon is either negligible or non-existent. There are several approaches to resolve the issue of membrane locking. A simple way to handle the problem is to use reduced or selective integration when computing the membrane strain energy terms [40]. This technique successfully removes the spurious constraints that cause the element to lock, but it can also introduce spurious modes that can lead to inaccuracies. Alternatively, Meck [41] has shown that full integration of quintic shape functions yields a displacement based element that does not exhibit membrane locking. While this is indeed helpful, using a quintic shape function can possibly introduce a high computational cost and adds complexity to the formulation. Bathe's [38] approach is to abandon a purely displacement based formulation, and adopt a mixed interpolation method to derive a simple yet efficient formulation for a general curved beam element. The transverse, bending and membrane strains are related to the nodal displacements and

rotations by evaluating the displacement-based strains and equating them to the assumed strains at the Gauss integration points. In other words, the mixed interpolated element matrices can be obtained by numerically evaluating the displacement-based element matrices at the Gauss integration points corresponding to the number of nodes in an element. Bathe's formulation considers one longitudinal strain, and two transverse shear strains. The formulation may be extended to include a separate torsional warping displacement variable through the addition of an appropriate out-of-plane warping displacement [42].

3.2.1 Kinematic relations and displacement interpolations

The Cartesian coordinates x, y, z of a point in the element are expressed using the natural coordinates r, s, and t (Fig. 30):,

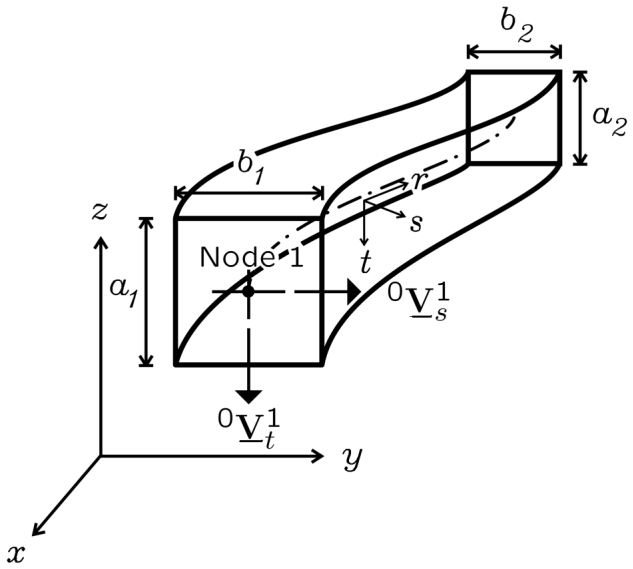

Figure 30: General curved beam element

$$
\begin{aligned}
x(r,s,t) &= \sum_{k=1}^{N} h_k x_k + \frac{t}{2}\sum_{k=1}^{N} a_k h_k {}^0V_{tx}^k + \frac{s}{2}\sum_{k=1}^{N} b_k h_k {}^0V_{sx}^k \\
y(r,s,t) &= \sum_{k=1}^{N} h_k y_k + \frac{t}{2}\sum_{k=1}^{N} a_k h_k {}^0V_{ty}^k + \frac{s}{2}\sum_{k=1}^{N} b_k h_k {}^0V_{sy}^k \\
z(r,s,t) &= \sum_{k=1}^{N} h_k z_k + \frac{t}{2}\sum_{k=1}^{N} a_k h_k {}^0V_{tz}^k + \frac{s}{2}\sum_{k=1}^{N} b_k h_k {}^0V_{sz}^k
\end{aligned}
\tag{35}
$$

where N is the number of nodes in the element, x_k, y_k, z_k are the coordinates of nodal point k, and a_k, b_k are the element's height and width at node k, and $h_k = h_k(r,s,t)$ is the k^{th} shape function. Also $\underline{V}_t = [V_{tx}\ V_{ty}\ V_{tz}]$, $\underline{V}_s = [V_{sx}\ V_{sy}\ V_{sz}]$ are unit vectors identifying the r and s directions, with the superscript ^{0} denoting the initial, or undeformed, configuration of the cross section at nodal location k.

The behavior of the curved beam element is described by 3 displacements and 3 rotations at each nodal location. Accordingly, the vector of the nodal degrees of freedom for node k can be expressed as:

$$\underline{\delta}_k = \{\ u \quad v \quad w \quad \theta_x \quad \theta_y \quad \theta_z\ \}_k^T \tag{36}$$

The displacement of any point within the element can be expressed in terms of the nodal degrees of freedom using the same functions employed to map the coordinates (eq. (35)):

$$\begin{aligned} u(r,s,t) &= \sum_{k=1}^{N} h_k u_k + \frac{t}{2}\sum_{k=1}^{N} a_k h_k V_{tx}^k + \frac{s}{2}\sum_{k=1}^{N} b_k h_k V_{sx}^k \\ v(r,s,t) &= \sum_{k=1}^{N} h_k v_k + \frac{t}{2}\sum_{k=1}^{N} a_k h_k V_{ty}^k + \frac{s}{2}\sum_{k=1}^{N} b_k h_k V_{sy}^k \\ w(r,s,t) &= \sum_{k=1}^{N} h_k w_k + \frac{t}{2}\sum_{k=1}^{N} a_k h_k V_{tz}^k + \frac{s}{2}\sum_{k=1}^{N} b_k h_k V_{sz}^k \end{aligned} \tag{37}$$

where

$$\underline{V}_t^k = \underline{\theta}_k \times {}^0\underline{V}_t^k \tag{38}$$

$$\underline{V}_s^k = \underline{\theta}_k \times {}^0\underline{V}_s^k \tag{39}$$

and

$$\underline{\theta}_k = \{\ \theta_x^k \quad \theta_y^k \quad \theta_z^k\ \}^T \tag{40}$$

The strain and displacement interpolation matrices can be formed using eqs. (35) and (40). The displacement interpolation relations are expressed in the following matrix form:

$$\underline{u} = \mathbf{H}\,\underline{\delta} \tag{41}$$

where $\underline{u} = \{u, v, w\}^T$, and where $\mathbf{H}$ is the displacement interpolation matrix, which is found by substituting eqs. (38) and (39) into eq. (37).

3.2.2 Strain-displacement interpolation

Derivatives in terms of the natural coordinates are related to those with respect to the Cartesian coordinates through the following expression:

$$\begin{bmatrix} \frac{\partial}{\partial x} \\ \frac{\partial}{\partial y} \\ \frac{\partial}{\partial z} \end{bmatrix} = \mathbf{J}^{-1} \begin{bmatrix} \frac{\partial}{\partial r} \\ \frac{\partial}{\partial s} \\ \frac{\partial}{\partial t} \end{bmatrix} \tag{42}$$

where $\mathbf{J}$ is the Jacobian matrix. The relation between partial derivatives of the element displacements in the natural coordinates and the nodal degrees of freedom can be expressed as:

$$\begin{bmatrix} \frac{\partial u}{\partial r} \\ \frac{\partial u}{\partial s} \\ \frac{\partial u}{\partial t} \end{bmatrix} = \sum_{k=1}^{N} \begin{bmatrix} \frac{\partial h_k}{\partial r} & [1 & (g)_{1i}^k & (g)_{2i}^k & (g)_{3i}^k] \\ h_k & [0 & (\hat{g})_{1i}^k & (\hat{g})_{2i}^k & (\hat{g})_{3i}^k] \\ h_k & [0 & (\bar{g})_{1i}^k & (\bar{g})_{2i}^k & (\bar{g})_{3i}^k] \end{bmatrix} \begin{bmatrix} u_k \\ \theta_x^k \\ \theta_y^k \\ \theta_z^k \end{bmatrix} \tag{43}$$

where,

$$(\hat{\mathbf{g}})^k = \frac{b_k}{2} \begin{bmatrix} 0 & -{}^0V_{sz}^k & {}^0V_{sy}^k \\ {}^0V_{sz}^k & 0 & -{}^0V_{sx}^k \\ -{}^0V_{sy}^k & {}^0V_{sx}^k & 0 \end{bmatrix}$$

$$(\bar{\mathbf{g}})^k = \frac{a_k}{2} \begin{bmatrix} 0 & -{}^0V_{tz}^k & {}^0V_{ty}^k \\ {}^0V_{tz}^k & 0 & -{}^0V_{tx}^k \\ -{}^0V_{ty}^k & {}^0V_{tx}^k & 0 \end{bmatrix}$$

$$(g)_{ij}^k = s(\hat{g})_{ij}^k + t(\bar{g})_{ij}^k$$

Derivatives of v and w are obtained by substituting v and w for u. In eq. (43), $i = 1$ for u, $i = 2$ for v, and $i = 3$ for w. The combination of equations in the form of eq. (43) for v and w gives the following relations between strains in the natural coordinate frame and the nodal degrees of freedom:

$$\underline{\epsilon} = \mathbf{B}\underline{\delta} \tag{44}$$

where $\mathbf{B}$ is the strain-displacement interpolation matrix and $\underline{\epsilon} = \{\epsilon_{rr}, \gamma_{rs}, \gamma_{rt}\}^T$. The strain in the global frame can be then obtained through the Jacobian of the coordinate transformation (eq. 42), which for displacement u for example gives:

$$\begin{bmatrix} \frac{\partial u}{\partial x} \\ \frac{\partial u}{\partial y} \\ \frac{\partial u}{\partial z} \end{bmatrix} = \sum_{k=1}^{N} \begin{bmatrix} J_{11}^{-1}\frac{\partial h_k}{\partial r} & (G1)_{i1}^k & (G2)_{i1}^k & (G3)_{i1}^k \\ J_{21}^{-1}\frac{\partial h_k}{\partial r} & (G1)_{i2}^k & (G2)_{i2}^k & (G1)_{i2}^k \\ J_{31}^{-1}\frac{\partial h_k}{\partial r} & (G1)_{i3}^k & (G2)_{i3}^k & (G1)_{i3}^k \end{bmatrix} \begin{bmatrix} u_k \\ \theta_x^k \\ \theta_y^k \\ \theta_z^k \end{bmatrix} \tag{45}$$

where,

$$(Gm)_{in}^k = [J_{n1}^{-1}(g)_{mi}^k]\frac{\partial h_k}{\partial r} + [J_{n2}^{-1}(\hat{g})_{mi}^k + J_{n3}^{-1}(\bar{g})_{mi}^k]h_k$$

3.2.3 Element Mass and Stiffness Matrix

The interpolation of displacements and strains is used to express the element strain and kinetic energy in terms of the nodal displacement vector $\underline{\delta}$. The strain energy of a curved beam element can be obtained from the following general expression:

$$U = \frac{1}{2}\int_V \underline{\epsilon}^T \, \mathbf{C} \, \underline{\epsilon} dV \tag{46}$$

where V is the volume of the beam, and $\mathbf{C}$ is the constitutive matrix for the beam material, which, for an isotropic beam, is defined as:

$$\mathbf{C} = \begin{bmatrix} E & 0 & 0 \\ 0 & G & 0 \\ 0 & 0 & G \end{bmatrix}$$

where E and G are the Young's and shear modulus of the material.

Imposing the strain-displacement relations defined in eq. (44) yields the following expression for the strain energy:

$$U = \frac{1}{2}\underline{\delta}^T \mathbf{K} \underline{\delta} \tag{47}$$

where $\mathbf{K}$ is the stiffness matrix for the considered curved beam element, which is given by:

$$\mathbf{K} = \int\int\int \mathbf{B}^T \mathbf{C} \mathbf{B} \det(\mathbf{J}) dr ds dt \tag{48}$$

Similarly, the kinetic energy for the curved beam can be obtained from:

$$T = \frac{1}{2}\int_V \rho \dot{\underline{u}}^T \dot{\underline{u}} dV \tag{49}$$

where ρ is the density of the beam's material, and where $\dot{(\,)}$ indicates differentiation with respect to time. Imposing the displacement interpolations defined in eq. (41) gives:

$$T = \frac{1}{2}\dot{\underline{\delta}}^T \mathbf{M} \dot{\underline{\delta}} \tag{50}$$

where $\mathbf{M}$ is the mass matrix for the considered beam element, defined as:

$$\mathbf{M} = \rho \int\int\int \mathbf{H}^T \mathbf{H} \det(\mathbf{J}) dr ds dt \tag{51}$$

3.3 Curved Beam Model Validation

3.3.1 Static Validation

The static performance of the general curved beam element is first evaluated. The tip rotation of the curved cantilever beam shown in Fig. 31 is computed using a single 3 node element and is compared with analytical predictions. The comparison is carried out for

Table 4: Properties of Cantilevered Curved Beam

Property	Value	Units
Young's modulus E	7×10^{10}	Pa
Density ρ	2700	kg/m^3
Poisson's ration ν	0.3	
θ	45°	

varying h/R ratios in order to evaluate the element's robustness for increasing radii of curvature for the beam. The properties of the cantilevered beam are listed in Table 4 and the results are listed in Table 5, which illustrates the accuracy of the considered curved beam element.

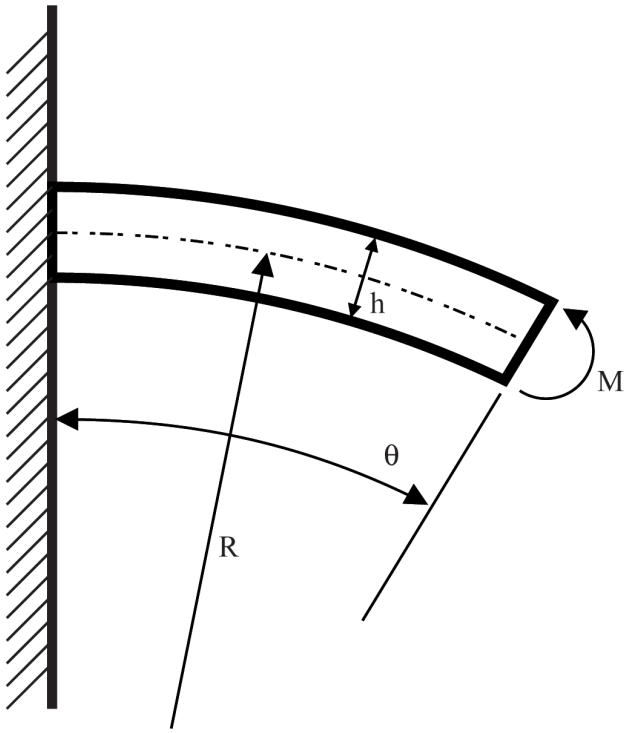

Figure 31: Cantilevered curved beam

3.3.2 Dynamic Validation

The dynamic performance of the general curved beam element is validated by comparing the FE predictions with the ANSYS results for a strip of 5 rectangular cells (Fig. 32). The

Table 5: FE predictions vs analytical solution for the tip deflection of cantilevered beam

h/R	FEM	Analytical
0.5	6.7441×10^{-7}	6.7320×10^{-7}
0.1	1.3488×10^{-6}	1.3464×10^{-6}
0.01	$1.3488E \times 10^{-5}$	1.3464×10^{-5}
0.001	$1.3488E \times 10^{-4}$	1.3464×10^{-4}

first 10 natural frequencies (ignoring the rigid body modes) are found for the FE model and compared with the ANSYS results in Table 6. The geometry and material properties of the strip are given in Table 7. The results indicate that all the computed natural frequencies show agreement with their ANSYS counterparts. The first three non-rigid body modes found using the FE model and ANSYS are compared and shown Fig. 33. This agreement is achieved despite using a much coarser mesh in the FE model than the one used in ANSYS. In ANSYS, the model of the strip had 480 2-noded BEAM4 elements, with 476 nodes. In comparison, the FE model only had 80 3-noded general beam elements and 156 nodes.

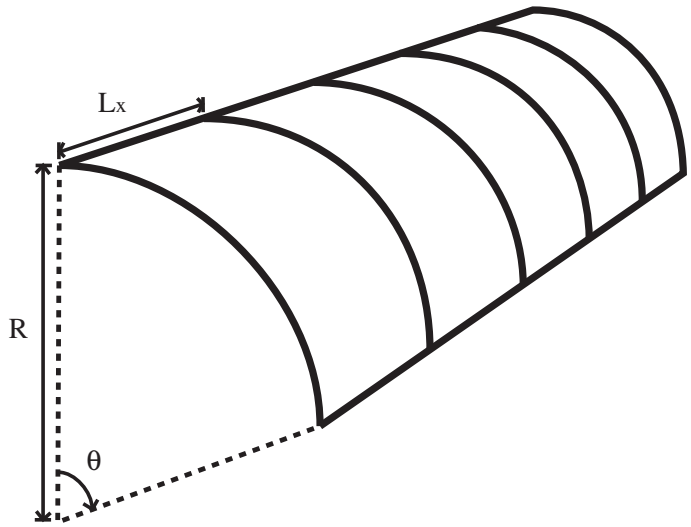

Figure 32: Strip of 5 Rectangular Cells

3.4 Spectral Beam Element Formulation

The Spectral finite element (SFE) method describes the behavior of each element composing the considered mesh through dynamic equations derived from distributed parameter

Table 6: ANSYS vs FE predictions for the first 10 natural frequencies of a strip of 5 rectangular cells

ANSYS (Hz)	FEM (Hz)	% Difference
0.0169	0.0168	0.59%
0.0463	0.0459	0.86%
0.0646	0.0644	0.31%
0.0898	0.0893	0.56%
0.0957	0.0955	0.21%
0.1437	0.1433	0.28%
0.1452	0.1448	0.28%
0.1709	0.1710	0.06%
0.2159	0.2144	0.69%
0.2498	0.2498	0.00%

Table 7: Material and geometry for the strip of 5 rectangular cells

Property	Value	Units
Young's Modulus, E	$7E10$	Pa
Poisson's Ratio, ν	0.3	
Density, ρ	2700	kg/m^3
Height of cross-section	0.01	m
Width of cross-section	0.01	m
R	10	m
L_x	10	m
θ	30°	

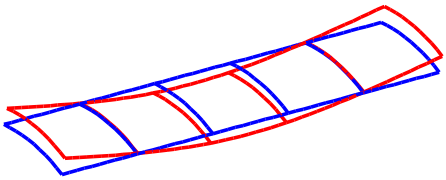

(a) FEM: $\omega = 0.0168Hz$

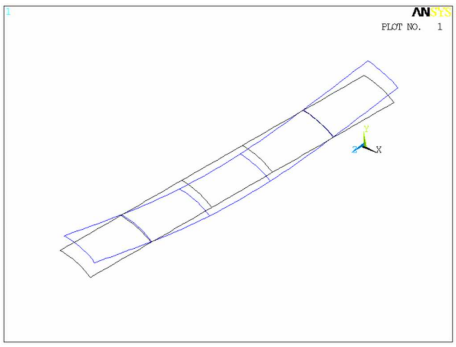

(b) ANSYS: $\omega = 0.0168Hz$

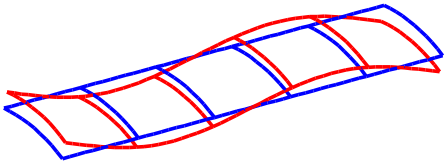

(c) FEM: $\omega = 0.0459Hz$

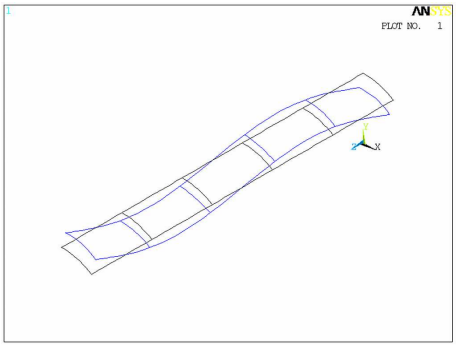

(d) ANSYS: $\omega = 0.0463Hz$

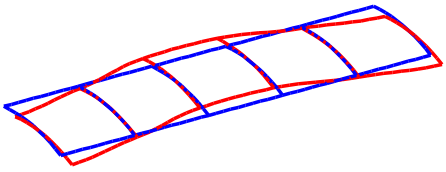

(e) FEM: $\omega = 0.0644Hz$

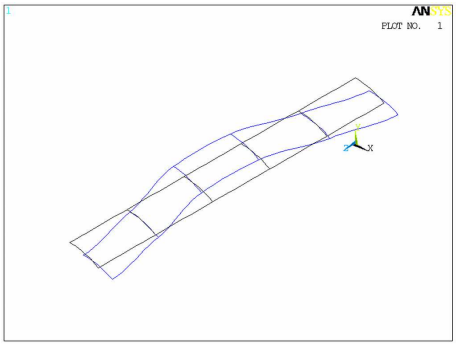

(f) ANSYS: $\omega = 0.0646Hz$

Figure 33: Mode Comparison

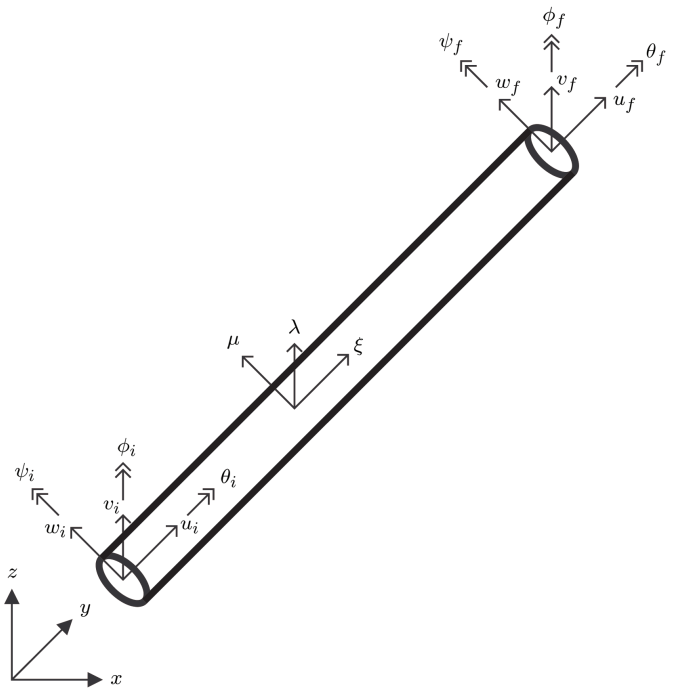

Figure 34: Beam element and considered degrees of freedom.

models [39, 43]. This allows an accurate prediction of the dynamic response of the structure over a wide frequency range, without requiring to refine the discretization as frequency increases. The dynamic behavior of each element is described in the local reference system $\mathcal{L} = (\xi, \lambda, \mu)$, rotated with respect to the global reference system $\mathcal{G} = (x, y, z)$ (see Figure 34). A Timoshenko beam model is considered to prevent loss of accuracy from use of Euler-Bernoulli beam theory for relatively short members.

3.4.1 Distributed parameter model in the local reference system

The spectral formulation for a Timoshenko beam element is outlined here. The equations of motion and boundary conditions governing the longitudinal and transverse vibrations of the beam can be derived by applying Hamilton's principle for a conservative system,

$$\int_{t_1}^{t_2} \delta(T - U + W)dt = 0 \tag{52}$$

where $\delta(.)$ denotes the first variation, where t_1 and t_2 are the initial and final time. T and U are respectively the kinetic and the strain energy of the beam, and W is the work

of the external forces. In the following development, it is assumed that the local axes λ and μ are principal centroidal axes of the cross section. It is assumed that $\lambda = \mu = 0$ at the centroid and the cross section has at least two axes of symmetry coinciding with the λ and μ axes. Additionally, it is also assumed that the centroid is coincident with the shear center. Furthermore for noncircular cross sections, the out of plane warping due to torsion is ignored for simplicity. Accordingly, the beam's strain energy in the local reference system can be expressed as:

$$\begin{aligned} U &= \frac{1}{2}\int_0^L \left[EAu_{,\xi}^2 + EI_{\lambda\lambda}\phi_{,\xi}^2 + EI_{\mu\mu}\psi_{,\xi}^2\right] \mathrm{d}\xi \\ &+ \frac{1}{2}\int_0^L \left[\kappa_\lambda AG(v_{,\xi} - \psi)^2 + \kappa_\mu AG(w_{,\xi} + \phi)^2 + GJ\theta_{,\xi}^2\right] \mathrm{d}\xi \end{aligned} \tag{53}$$

where E, G are the Young's and shear moduli of the beam material, A, $I_{\lambda\lambda}$ and $I_{\mu\mu}$ are respectively, the area, and the second moments of area of the beam cross section with respect to λ and μ, GJ is the torsional rigidity, and κ_λ and κ_μ are the shear coefficients with respect to λ and μ, respectively. Also, in equation (53), $u = u(\xi, t), v = v(\xi, t), w = w(\xi, t)$ denote the axial and transverse deflections of the beam, while $\theta = \theta(\xi, t), \phi = \phi(\xi, t), \psi = \psi(\xi, t)$ are three section rotation angles at location ξ and time t. Finally, the following notation $(\diamond)_{,\xi} = \frac{\partial(\diamond)}{\partial\xi}$ is used to denote partial differentiation along the local axis ξ.

The kinetic energy is given by

$$T = \frac{1}{2}\int_0^L \left[\rho A(\dot{u}^2 + \dot{v}^2 + \dot{w}^2) + \rho I_p\dot{\theta}^2 + \rho I_{\lambda\lambda}\dot{\phi}^2 + \rho I_{\mu\mu}\dot{\psi}^2\right] \mathrm{d}\xi \tag{54}$$

where ρ is the density of the beam material and I_p is the polar moment of inertia.

Substituting U and T in eq. (52), assuming the absence of external forces ($W = 0$), and performing the variations gives a set of six differential equations describing the beam's longitudinal and transverse vibrations. For harmonic motion at frequency ω the equations of motion are

$$
\begin{aligned}
EAu_{,\xi\xi} + \rho A\omega^2 u &= 0 \\
\kappa_\lambda AG(v_{,\xi\xi} - \psi_{,\xi}) + \rho A\omega^2 v &= 0 \\
\kappa_\mu AG(w_{,\xi\xi} + \phi_{,\xi}) + \rho A\omega^2 w &= 0 \qquad (55) \\
GJ\theta_{,\xi\xi} + \rho I_p \omega^2 \theta &= 0 \\
EI_{\lambda\lambda}\phi_{,\xi\xi} + \kappa_\mu AG(w_{,\xi} + \phi) + \rho I_{\lambda\lambda}\omega^2\phi &= 0 \\
EI_{\mu\mu}\psi_{,\xi\xi} + \kappa_\lambda AG(v_{,\xi} - \psi) + \rho I_{\mu\mu}\omega^2\psi &= 0 \qquad (56)
\end{aligned}
$$

3.4.2 Dynamic Stiffness Matrix in Local Coordinates

Equations (55) can be rewritten in matrix form as follows:

$$\underline{z}_{,\xi}(\xi) = \boldsymbol{A}\underline{z}(\xi) \tag{57}$$

where $\boldsymbol{A}$ is a matrix of constant coefficients, and where

$$\underline{z} = [\ u \quad v \quad w \quad \theta \quad \phi \quad \psi \quad u_{,\xi} \quad v_{,\xi} \quad w_{,\xi} \quad \theta_{,\xi} \quad \phi_{,\xi} \quad \psi_{,\xi}\ ]^T \tag{58}$$

is the state vector describing the axial and bending behavior of the considered beam element at frequency ω. A general solution of equation (57) can be expressed as:

$$\underline{z}(\xi) = e^{\boldsymbol{A}\xi}\underline{z}(0) \tag{59}$$

which relates the vector $\underline{z}$ at the generic location ξ with that at $\xi = 0$. An alternative expression for the state vector can be introduced to contain generalized displacements and stress resultants at the considered location. A vector $\boldsymbol{y}$ can be defined as:

$$\underline{y} = [\ u \quad v \quad w \quad \theta \quad \phi \quad \psi \quad N \quad V_\lambda \quad V_\mu \quad M_\xi \quad M_\mu \quad M_\lambda\ ]^T \tag{60}$$

where,

$$
\begin{aligned}
N(\xi) &= EAu_{,\xi} \\
V_\lambda(\xi) &= \kappa_\lambda AG(v_{,\xi} - \psi) \\
V_\mu(\xi) &= \kappa_\mu AG(w_{,\xi} + \phi) \\
M_\xi(\xi) &= GJ\theta_{,\xi} \\
M_\lambda(\xi) &= EI_{\lambda\lambda}\phi_{,\xi} \\
M_\mu(\xi) &= EI_{\mu\mu}\psi_{,\xi}
\end{aligned}
$$

are respectively the axial resultant, the shear forces, the torsional and bending moments at location ξ. The vector $\underline{y}$ and $\underline{z}$ are simply related through the following expression:

$$
\underline{y}(\xi) = \boldsymbol{G}\underline{z}(\xi) \tag{61}
$$

where $\boldsymbol{G}$ is a matrix containing the material and cross sectional properties of the beam element. Equations (59) and (61) can be used to obtain a relation between state vectors at two locations on the element:

$$
\begin{aligned}
\underline{y}(\xi) &= \boldsymbol{G}e^{\boldsymbol{A}\xi}\boldsymbol{G}^{-1}\underline{y}(0) \\
\underline{y}(\xi) &= \boldsymbol{T}(\xi)\underline{y}(0)
\end{aligned} \tag{62}
$$

where $\boldsymbol{T}(\xi)$ is the "transfer matrix" of the beam element calculated at location ξ. The transfer matrix can be used to relate generalized displacements and forces at the two ends of the beam element:

$$
\underline{y}(L) = \boldsymbol{T}(L)\underline{y}(0) \tag{63}
$$

Equation (63) can be expanded as follows:

$$
\begin{pmatrix} \underline{u}_f \\ \underline{f}_f \end{pmatrix} = \begin{pmatrix} \boldsymbol{T}_{11} & \boldsymbol{T}_{12} \\ \boldsymbol{T}_{21} & \boldsymbol{T}_{22} \end{pmatrix} \begin{pmatrix} \underline{u}_i \\ \underline{f}_i \end{pmatrix} \tag{64}
$$

where $\underline{u}_i, \underline{u}_f$ and $\underline{f}_i, \underline{f}_f$ respectively are the generalized displacements and forces at the initial and final node. Equation (64) can be rearranged to obtain:

$$\underline{f}_e^{\mathcal{L}} = \boldsymbol{K}_{d_e}^{\mathcal{L}} \underline{u}_e^{\mathcal{L}} \tag{65}$$

where $\underline{f}_e^{\mathcal{L}} = (\underline{f}_i, \ -\underline{f}_f)^T$, $\underline{u}_e^{\mathcal{L}} = (\underline{u}_i, \ \underline{u}_f)^T$, and where $\boldsymbol{K}_{d_e}^{\mathcal{L}}$ is the dynamic stiffness matrix of the element, which is obtained as:

$$\boldsymbol{K}_{d_e}^{\mathcal{L}} = \begin{pmatrix} -\boldsymbol{T}_{12}^{-1}\boldsymbol{T}_{11} & \boldsymbol{T}_{12}^{-1} \\ \boldsymbol{T}_{12} + \boldsymbol{T}_{22}\boldsymbol{T}_{12}^{-1}\boldsymbol{T}_{11} & \boldsymbol{T}_{22}\boldsymbol{T}_{12}^{-1} \end{pmatrix} \tag{66}$$

In equation (65), the subscript e denotes vectors pertaining to the element, while superscript $\mathcal{L}$ indicates that the expression is obtained in the local reference system $\mathcal{L} = (\xi, \lambda, \mu)$. This frequency-domain, finite-element formulation, denoted as "spectral" [39], allows an accurate prediction of the dynamic response of the global structure by using a reduced number of elements. As opposed to traditional finite elements, the number of elements does not need to be increased to fully capture the dynamic response at high frequencies. One should note however that the evaluation of the shape functions from the continuous beam model requires the evaluation of an exponential matrix, which at extremely high frequencies may become affected by numerical errors that limit the accuracy of the analysis. These numerical difficulties can be circumvented by considering finer meshes. Regardless of such limitations, the high frequency behavior can be captured with a substantially reduced number of elements with respect to conventional formulations.

3.4.3 Dynamic shape functions

The interpolation functions which express the generalized displacements of points within the element as a function of the nodal degrees of freedom can be expressed using the transfer function formulation (eq. (62)). According to eq. (62), the generalized displacements at location ξ, $\underline{u}(\xi)$, can be expressed as:

$$\underline{u}(\xi) = \boldsymbol{T}_{11}(\xi)\underline{u}_i + \boldsymbol{T}_{12}(\xi)\underline{f}_i \tag{67}$$

where $\underline{u}(\xi)$ is given by,

$$\underline{u}(\xi) = [\ u(\xi) \quad v(\xi) \quad w(\xi) \quad \theta(\xi) \quad \phi(\xi) \quad \psi(\xi)\ ]^T \tag{68}$$

and in particular the displacements for $\xi = L$ are given as:

$$\underline{u}_f = \boldsymbol{T}_{11}(L)\underline{u}_i + \boldsymbol{T}_{12}(L)\underline{f}_i \tag{69}$$

From equation (69), one obtains:

$$\underline{f}_i = \boldsymbol{T}_{12}^{-1}(L)[\boldsymbol{T}_{11}(L)\underline{u}_i - \underline{u}_f] \tag{70}$$

which can be substituted into equation (67) to give:

$$\begin{aligned} \underline{u}(\xi) &= \left[\ \boldsymbol{T}_{11}(\xi) + \boldsymbol{T}_{12}(\xi)\boldsymbol{T}_{12}^{-1}(L)\boldsymbol{T}_{11}(L) \quad \boldsymbol{T}_{12}(\xi)\boldsymbol{T}_{12}^{-1}(L)\ \right] \underline{u}_e^{\mathcal{L}} \\ \underline{u}(\xi) &= \boldsymbol{N}(\xi)\underline{u}_e^{\mathcal{L}} \end{aligned} \tag{71}$$

where $\boldsymbol{N}(\xi)$ is the matrix of the dynamic interpolation functions. The dynamic stiffness matrix for the element is obtained from the beam's distributed parameter model for harmonic motion at frequency ω. Within the validity of Timoshenko approximations, the model reproduces the exact displacements of the considered element. The Timoshenko beam model requires $\frac{h^3}{l^3} \ll 1$, where h is the cross-sectional characteristic length and l is the wavelength of deformation along the beam. Within these limitations, a single finite element is sufficient to fully characterize the response of the beam in the frequency domain.

3.4.4 Performance of spectral finite elements

The performance of the spectral finite element formulation is validated by computing the frequency response of a cantilever beam with a tip load (Fig. 35). The configuration of the beam is given in Table 8. The frequency response for the cantilevered beam is first computed using a mesh containing a single spectral element and two nodes. Then the beam is modelled using the general beam element presented in Section 3.2. The frequency response is found for three different meshes of varying refinement. The first mesh considered

Table 8: Material and geometry of the cantilever beam

Property	Value	Units
Young's Modulus, E	7×10^{10}	Pa
Poisson's Ratio, ν	0.3	
Density, ρ	2700	kg/m^3
Height of cross-section	0.05	m
Width of cross-section	0.05	m
L	2	m
Force, F	1	N

is the coarsest with 2 elements and 5 nodes, then the second mesh is refined to consider 6 elements with 13 nodes. The last mesh considered consists of 20 elements and 41 nodes. The frequency response of the tip deflection is computed over the range 0-1000 Hz. Fig. 36 shows the frequency response comparison for the spectral element versus the three different meshes using the general beam element. The first mesh is only accurate up to around 50 Hz and cannot capture the beam's behavior accurately above this frequency (Fig. 36.a). The second mesh is accurate up to around 400 Hz (Fig. 36.b). The finest mesh using the general beam element shows the best agreement and only differs slightly for frequencies higher than 850 Hz (Fig. 36.c). This reaffirms the fact that spectral finite elements can be used to obtain accurate harmonic responses without having to refine the mesh to capture high frequency behavior.

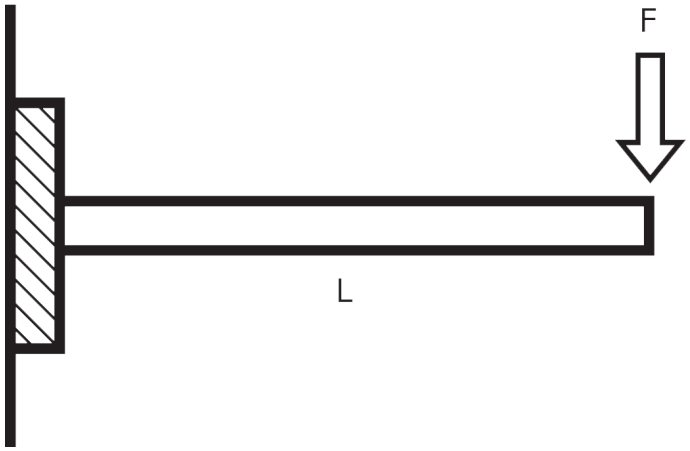

Figure 35: Cantilevered beam with tip load

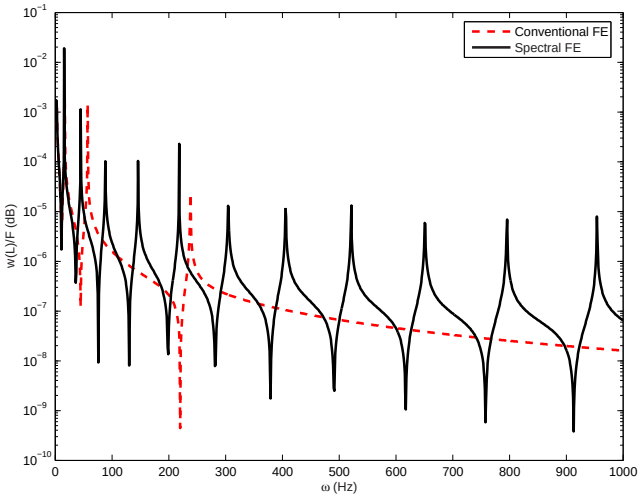

(a) Spectral vs Coarse Mesh

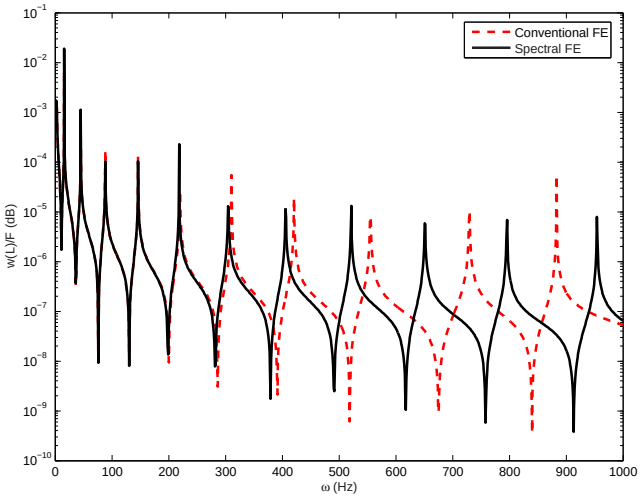

(b) Spectral vs Fine Mesh

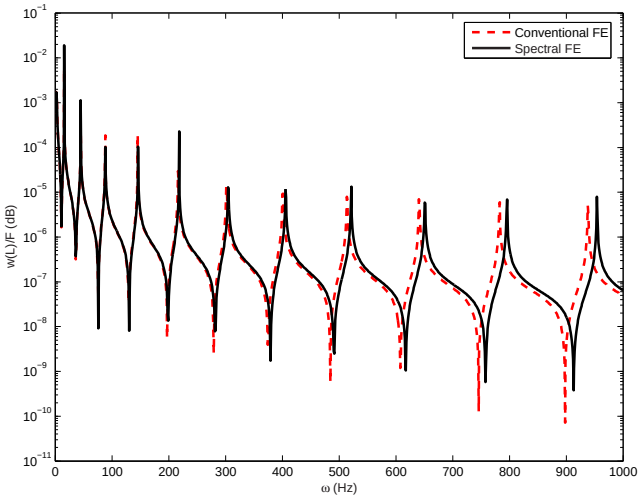

(c) Spectral vs Very Fine Mesh

Figure 36: FRF Comparison

CHAPTER IV

ANALYSIS AND OPTIMIZATION OF RECTANGULAR GRIDS

4.1 Overview

In this chapter the properties of a simple rectangular lattice structure are investigated. This simple configuration is selected to demonstrate the attractive properties of the considered type of cellular structures and to test the developed analysis procedures. The objective of the investigations is to evaluate the band-gap and directionality properties of the considered grids and to demonstrate the design flexibility offered even by simple configurations. The sensitivity of band-gap location and width, and of the directional behavior with respect to changes to the unit cell configuration is first analyzed. This sensitivity study then guides the formulation of an optimization problem which aims at maximizing an objective function accounting for both directionality at low frequencies and band-gap width and location. The study is performed by combining the theory outlined in Chapter 2 and the finite element formulation detailed in Chapter 3, which is used for the detailed modeling of a unit cell. The predictions from the theory of periodic structures and the performance of the grid are then evaluated through the estimation of the harmonic response of grids obtained through the assembly of several unit cells. The computational cost associated to this procedure is significantly reduced through the application of Spectral Finite Elements (SFE), as described in Chapter 3. The evaluation of harmonic response of the grid through a completely different model also serves as a validation for predictions of the unit cell analysis.

4.2 Analysis of a baseline lattice configuration

The lattice is composed of beam elements of circular cross section rigidly connected to form a frame-type structure. The diameter of the members varies periodically along the x, y directions according to the configuration shown in Fig. 37, while the diameter of the diagonal components is uniform throughout the structure, but generally different from that of the vertical and horizontal beams. A similar configuration, without diagonal members,

has previously been proposed and studied by Martinsson et al [44].

A baseline configuration is first analyzed to describe the main characteristics of the lattice. A non-dimensionalization strategy will then be introduced so that the results presented in the remainder of the chapter will be independent upon material, and dimensions of the unit cell.

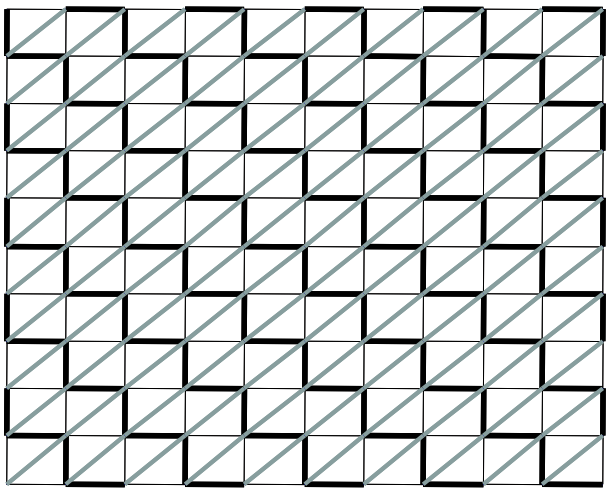

(a) Lattice

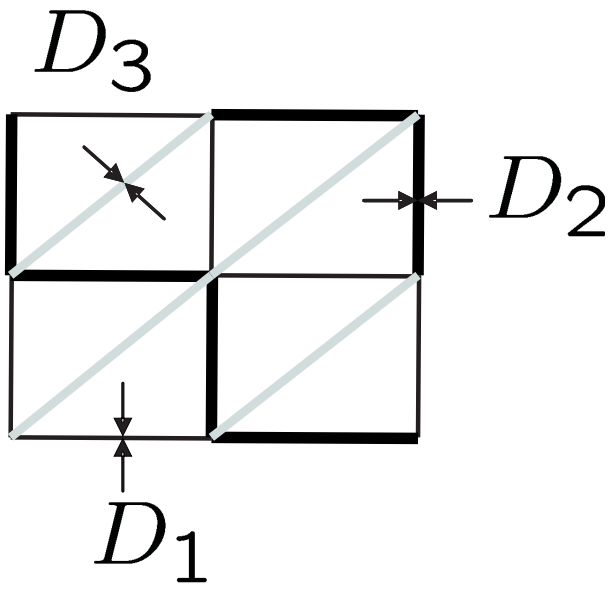

(b) Unit cell

Figure 37: Considered rectangular lattice

4.2.1 Geometry and material properties

The baseline configuration assumes that the lattice is made of ABS plastic, whose properties are listed in Table 9. The unit cell is square and measures 5 cm per side. Material and unit cell dimensions are conveniently chosen for future manufacturing of the periodic assembly through stereolithography techniques.

Table 9: Mechanical properties and geometry of rectangular lattice.

Property	Value	Units
Young's Modulus	2.634×10^9	Pa
Density	1180	kg/m^3
Poisson's Ratio ν	0.3	
Diameter D_1	2.5	mm

4.2.2 FE modeling of the unit cell

The unit cell is modeled using the general beam element described in the previous chapter. The FE discretization used for the cell analysis is selected in order to accurately capture the cell's dynamic behavior in a frequency range corresponding approximately to the first 7 phase constant surfaces. It can be shown how this frequency range includes a large number of modes for the assembled lattice, and therefore it reproduces most of its dynamic behavior [45], [46]. A convergence study is performed on the lattice dispersion relations obtained by varying the phase constant surfaces along the contour of the first irreducible Brioullin zone for the lattice shown in Fig. 38. The dispersion relations obtained with increasing increasing mesh refinement are shown in Fig. 39, which indicates how 4 elements per side are sufficient to fully capture the cell dynamic behavior in the considered frequency range, and how increasing the number of elements does not change the dispersion relation predictions. The selected FE mesh is depicted in Fig. 40.

4.2.3 Analysis of band-gap behavior and non-dimensionalization factor

The dispersion relations shown in Fig. 41.a, which are obtained for $D_2 = 1.5D_1$ and $D_3 = 0$, clearly show a band-gap between approximately 3800 and 5000 rad/s. The presence of the

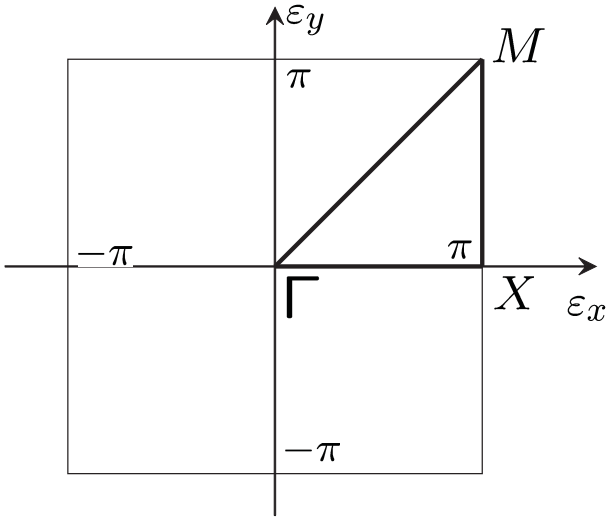

Figure 38: First Brioullin zone

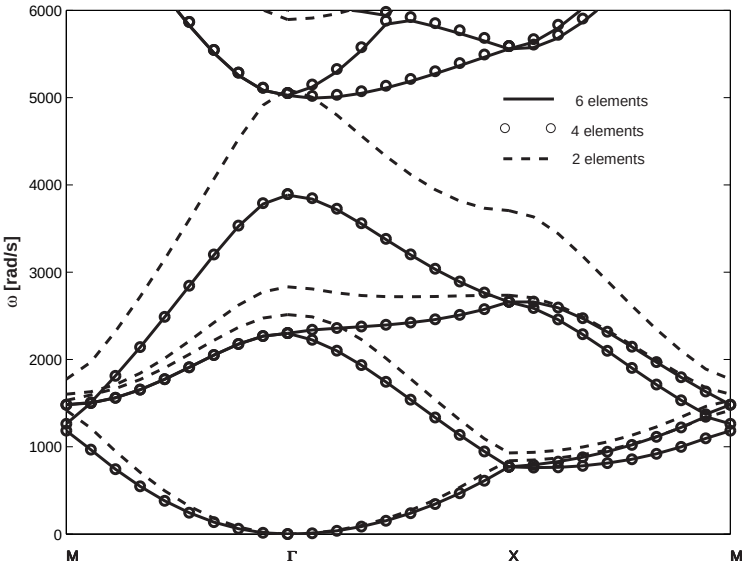

Figure 39: Dispersion relations for increasing number of elements

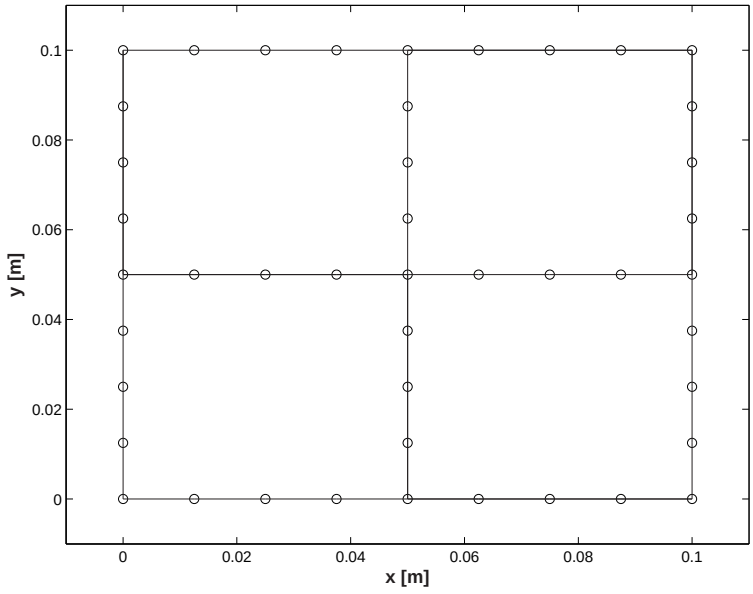

Figure 40: Mesh selected for unit cell analysis (nodes 'o')

band-gap can be attributed to the impedance mismatch caused by the difference in diameter D_1, D_2, which affects the relative impedance of the lattice members. The lower boundary of the band-gap corresponds to a frequency which can be evaluated by imposing $\varepsilon_x = \varepsilon_y = 0$ and computing the resulting eigenvalues and eigenvectors. Of particular interest is the eigenvector corresponding to the band-gap lower boundary, which is presented in Fig. 42.a. It is interesting to observe how the occurrence of a band-gap coincides with the internal resonance of some of the members of the unit cell, while the other members remain almost undeformed. This comment is in line with the discussion presented in Chapter 2 for the case of the spring-mass lattice. The dispersion relation for a grid with $D_2 = D_1$ and $D_3 = 0$ is shown in Fig. 41.a. In the considered frequency range, this grid does not present any band-gaps. It is therefore interesting to consider the same mode for which the previous grid presented internal resonance. This mode, presented in Fig. 42.b, shows a global deformation of all the unit cell members, as opposed to the more localized pattern of the mode shown in Fig. 42.a. This particular behavior can be considered as an indicator of the occurrence, or lack of, of a band-gap in a given lattice. The frequency of resonance of the beams belonging to the unit cell can in general be predicted by:

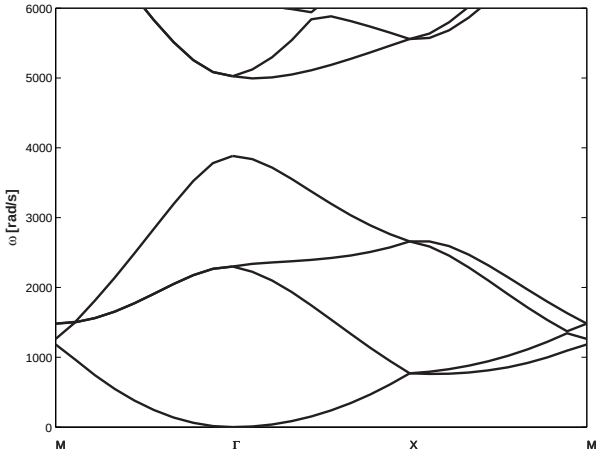

(a) $D_2 = 1.5D_1$

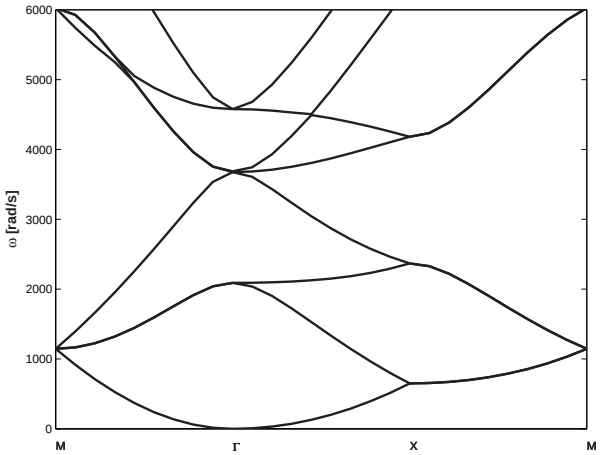

(b) $D_2 = D_1$

Figure 41: Dispersion relations for 2 grid configurations

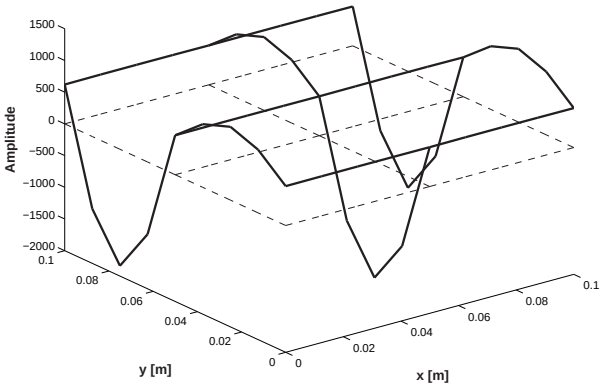

(a) $D_2 = 1.5D_1$

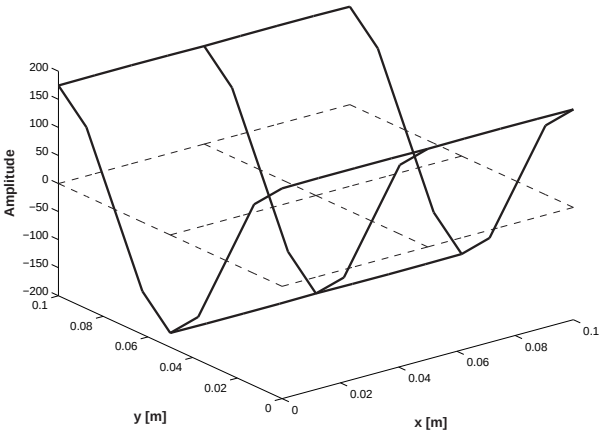

(b) $D_2 = D_1$

Figure 42: Unit cell modes for grid with (a) and without (b) band-gaps

$$\omega = \beta^2 \frac{1}{L_i^2} \sqrt{\frac{EI_i}{m_i}} \tag{72}$$

where L_i, EI_i and m_i are the length, the bending stiffness and linear mass of the beams belonging to the lattice, with the subscript $i = 1, 2, 3$ indicating beams of diameter D_i. Also in eq. (73), β is a non-dimensional parameter that depends on the boundary conditions applied to the ends of each beam. It can therefore be expected that the occurrence of a band-gap is related to the frequency of eq. (73), so that it may be used to scale the lattice behavior and non-dimensionalize the analysis that follows. The boundary conditions of each beam of the lattice are quite complex as they include the flexibility of neighboring beams connected to it. Hence, a value for β cannot be easily specified in this case. The following parameter is therefore used for the non-dimensionalization of the analysis:

$$\omega_0 = \frac{1}{L_1} \sqrt{\frac{EI_1}{m_1}} \tag{73}$$

The validity of ω_0 as a scaling parameter can be tested by considering the dispersion relations of different grids scaled with respect to the baseline configuration. The analysis is performed by changing the length l of the unit cell and the diameter of the beams D_2, while keeping the ratio D_2/D_1 constant. The dispersion relations in terms of the normalized frequency $\Omega = \omega/\omega_0$ are presented in Fig. 43. The plot shows that dispersion relations of scaled grids actually coincide when the frequency is normalized, and that the dispersion relations scale exactly as ω_0. This parameter will then be used in the remainder of this chapter to present results which are independent upon the absolute dimensions of the grid and its material properties.

4.3 Directional and band-gap behavior of the grids

4.3.1 Directional Behavior

The directional behavior of the lattice is investigated through Bloch's theorem and the phase constant surface analysis. The influence of the unit cell configuration on the directional performance of the grid is investigated by considering cell configurations obtained for different combinations of diameters D_1, D_2, D_3.

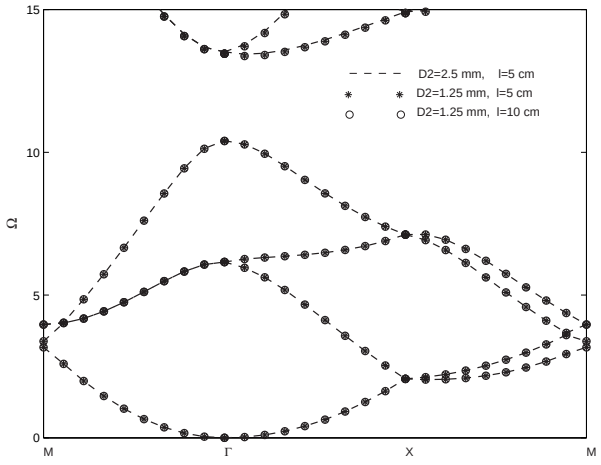

Figure 43: Comparison of non-dimensional dispersion relations for various grids

Fig. 44.a shows for example the contour plot of the first phase constant surface obtained for $D_3 = 0$ and $D_2 = D_1$. The isofrequency contour lines in the considered normalized frequency range are very regular and the perpendicular to each contour line is characterized by a slope that spans the entire angular range ($0-90°$). This indicates that wave propagation occurs in all directions. The phase constant surface obtained for a configuration with $D_2 = D_1$ and $D_3 = 1.5D_1$ shows a significantly different behavior (Fig. 44.b), whereby a limited angular range, centered at 45°, can be observed. This preliminary results indicate that the lattice design can be modified to achieve wave attenuation properties by adding or removing the diagonal member. In particular, the results of Fig. 44 indicate that adding a diagonal member causes the behavior of the lattice to become directional along the 45° direction. The influence of the diagonal beam member on the directional behavior is studied by considering the extension of the angular range of wave propagation for various unit cell configurations. Directionality is quantified by evaluating the angle spanned by the normal to the iso-frequency line corresponding to an assigned frequency range. This angle is here called "propagation angle". A propagation angle varying between 0 and 90° indicates that waves are free to propagate along any direction on the plane of the structure, while a smaller range of variation indicates directionality. The propagation angle is evaluated for various combination of diameter D_1, D_2, D_3 over a normalized frequency range of up to

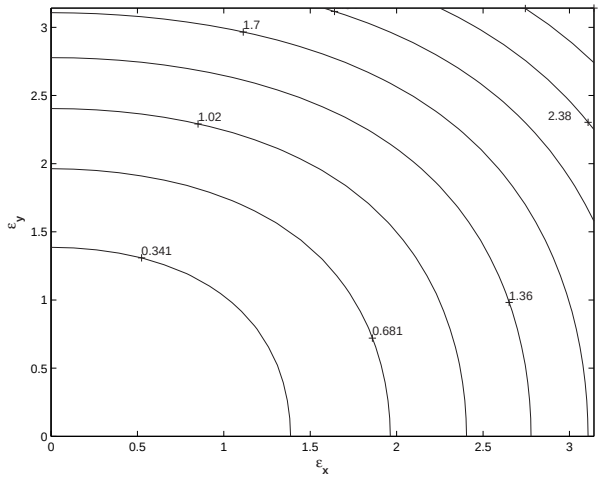

(a) $D_2 = D_1$, $D_3 = 0$

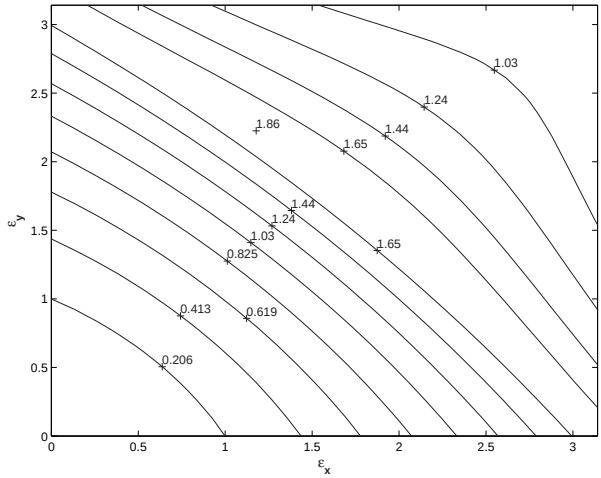

(b) $D_2 = D_1$, $D_3 = 1.5D_1$

Figure 44: First phase constant surfaces for different lattices

$\Omega = 1.1$, which covers most of the first phase constant surface range for all considered configurations. The results of this sensitivity analysis are shown in Fig. 45. Fig. 45.a is a plot of the maximum and minimum angle of propagation for a given configuration. A maximum angle of 90° and a minimum angle of 0° corresponds to a case where waves are free to propagate in all directions. In this sensitivity analysis, it is evident that wave propagation is strongly favored in the ±45° direction in configurations with a diagonal beam (Fig. 45.a). Additionally, it can also be deduced that the larger the diameter of the diagonal beam, D_3, the stronger the directional behavior. However, increasing the diameter of the second beam D_2 has the reverse effect of reducing directionality (Fig. 45.b).

4.3.2 Band-gap Behavior

The dispersion relations for various diameter combinations are shown in Fig. 46. From these results it is evident how the relative values of the diameter have a strong influence on band-gap width and location. In particular, the plots of Fig. 46 suggest that adding a diagonal is detrimental to the band-gap behavior, which is a trend opposite to that observed for directionality. The sensitivity of the band-gap behavior is again investigated for various combinations of the diameters D_1, D_2, D_3 by monitoring band-gap normalized width ($\Delta\Omega$) and associated center frequency (Ω_c). Fig. 47 shows the variation of the the band-gap with respect to D_2/D_1 for different values of D_3/D_1. From this analysis, it is determined that the largest band-gap exists when there are no diagonal beams in the unit cell ($D_3/D_1 = 0$). Fig. 48 shows the sensitivity of the band-gap location, here quantified by its central frequency, with respect to D_2/D_1 for different values of D_3/D_1. It is found that the largest band-gap with $D_3/D_1 = 0$ generally occur at higher frequencies than the smaller band-gaps found with the unit cells with diagonal beams.

4.4 Harmonic Response of rectangular lattices

The characteristic behavior of the considered lattice configuration is demonstrated by evaluating the harmonic response of structural systems obtained through the assembly of the unit cells here proposed. All the structures are composed of 20 cells in the x, y directions to form a square grid. The lattices are unconstrained and excited by a harmonic force of unit

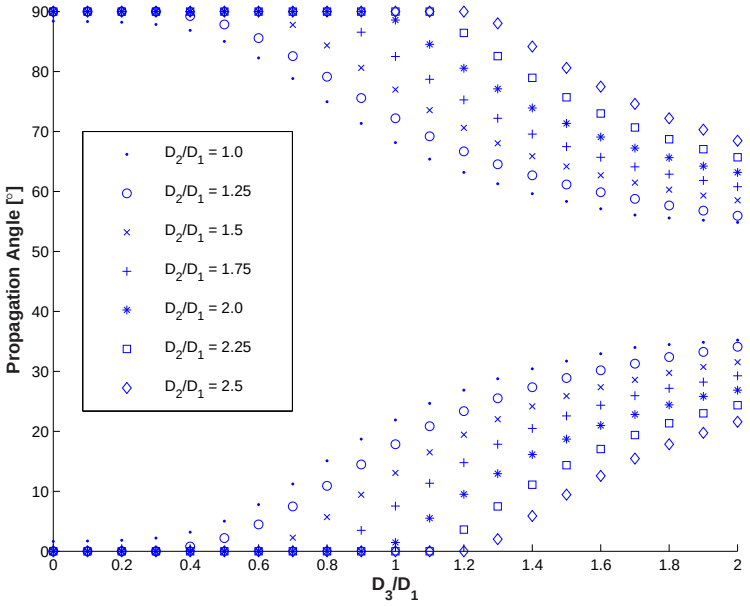

(a) Maximum and minimum angle of propagation

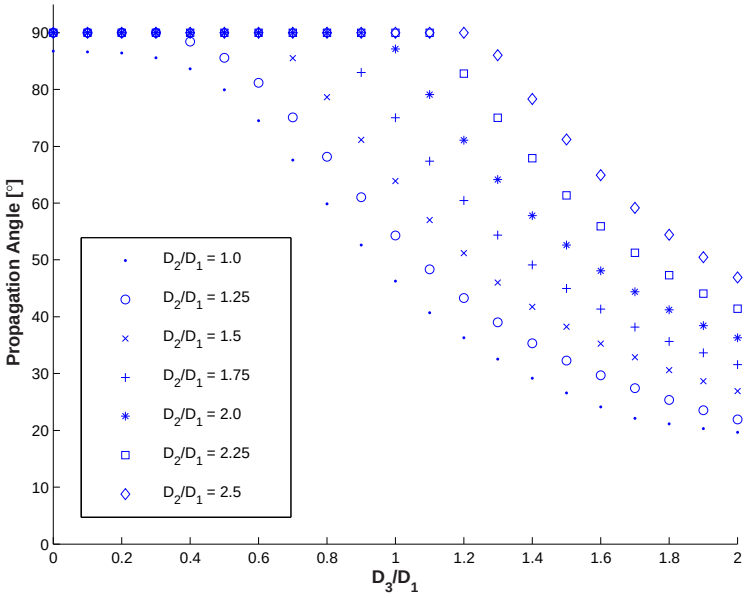

(b) Angular range of propagation

Figure 45: Sensitivity analysis of directional behavior

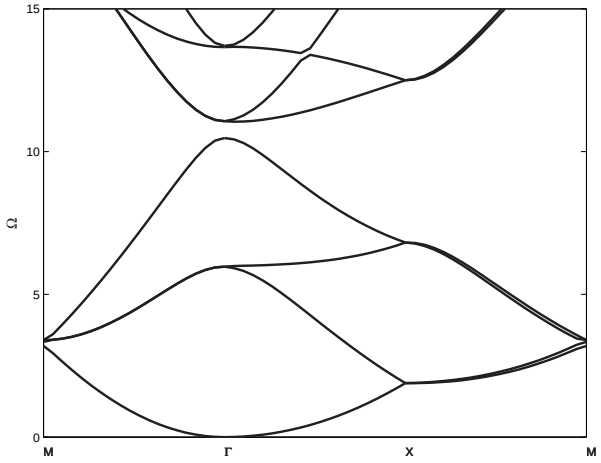

(a) $D_2 = 1.2D_1$, $D_3 = 0$

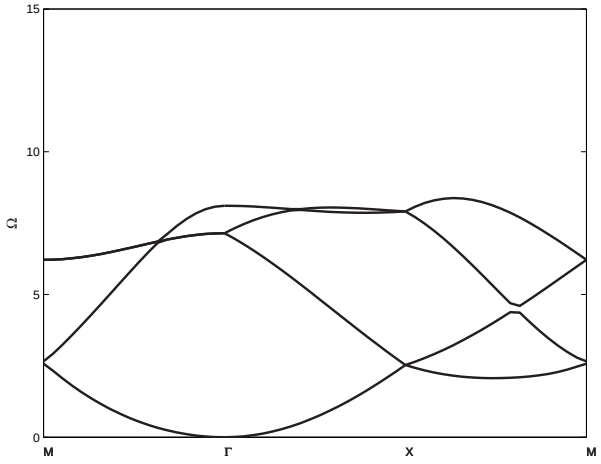

(b) $D_2 = 2.5D_1$, $D_3 = 0$

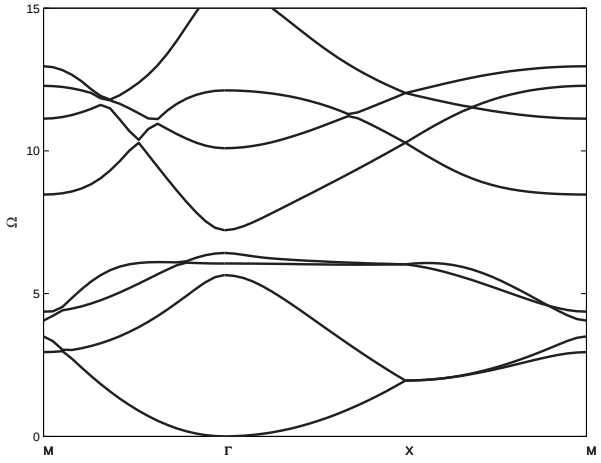

(c) $D_1 = 2D_2$, $D_3 = D_1$

Figure 46: Dispersion relations for various gird configurations

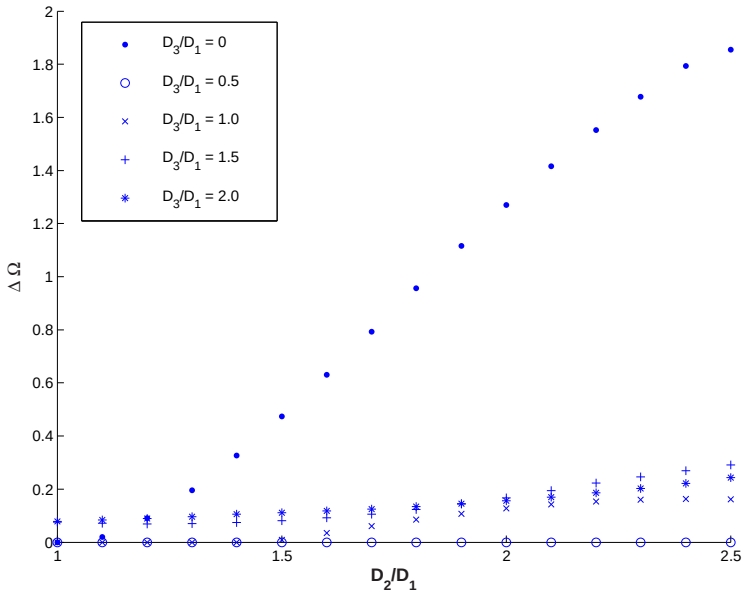

Figure 47: Sensitivity analysis of band-gap width

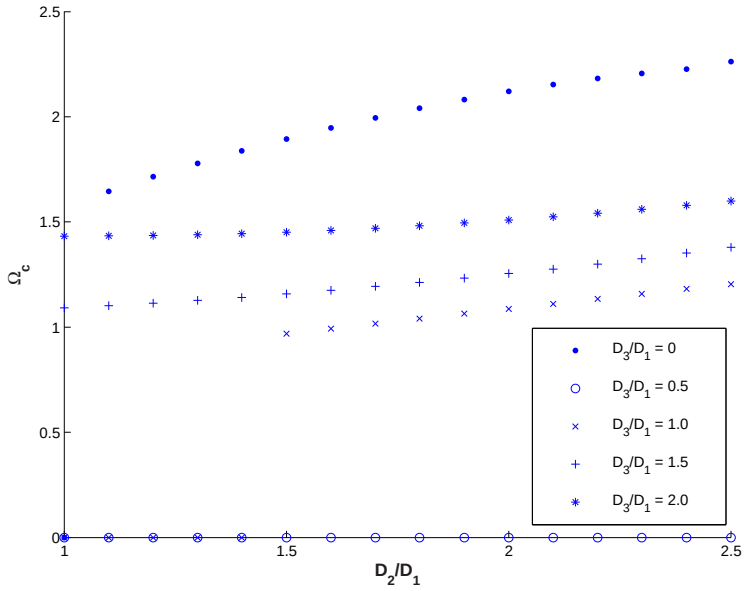

Figure 48: Sensitivity of band-gap center frequency

amplitude and specified frequency applied at the lower left corner of the structure. The force is directed perpendicularly to the x, y plane in order to excite its out-of-plane motion. The unit cells considered above are here used to investigate both directional and band-gap behaviors of the assemblies. Spectral finite elements, detailed in Chapter 3, are used to model the lattices and reduce computational cost.

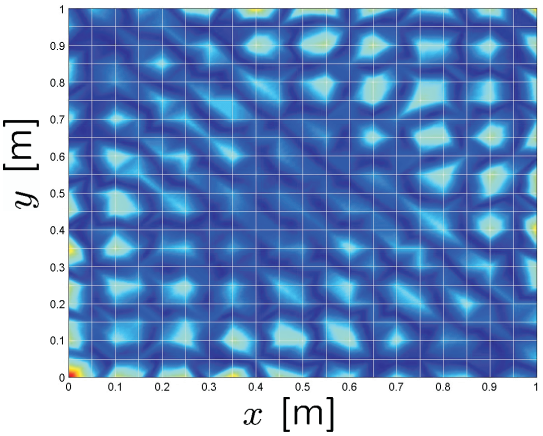

(a) $D_1 = D_2$, $D_3 = 0$

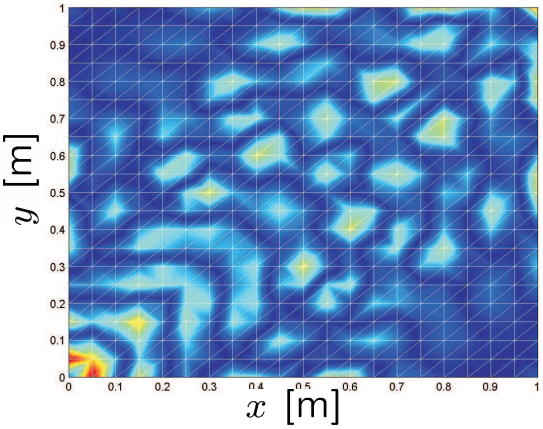

(b) $D_1 = D_2 = D_3$

Figure 49: Amplitude of harmonic response at $\Omega = 1.9$ for different lattices

Fig. 49 compares the magnitudes of the out of plane displacements corresponding to an excitation at $\Omega = 1.9$ for two different lattices. The response for the first lattice ($D_1 = D_2$, $D_3 = 0$) does not show any particular directional behavior, while the response of the second lattice ($D_1 = D_2 = D_3$) clearly demonstrates how wave propagation mostly occurs

along a 45° line. The continuous maps have been obtained through the two-dimensional interpolation of the displacements of the nodes in the grid.

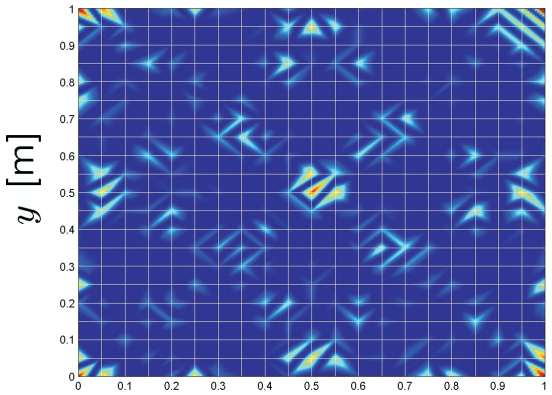

(a) $D_1 = D_2$, $D_3 = 0$

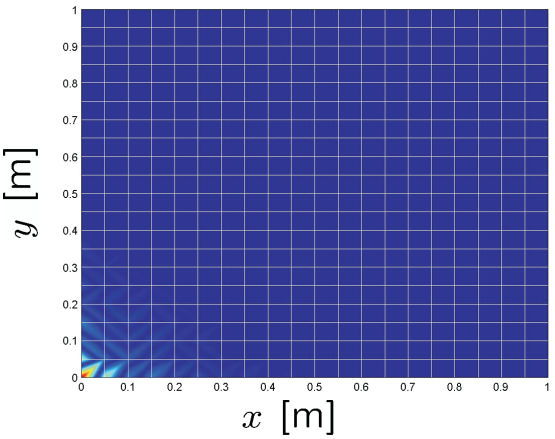

(b) $D_2 = 1.5D_1$, $D_3 = 0$

Figure 50: Amplitude of harmonic response at $\Omega = 12$ for different lattices

Fig. 50 compares the vibration amplitude at $\Omega = 12$ for the two different lattices. As predicted by Fig. 46, the amplitude map of Fig. 50.b demonstrates the wave attenuation behavior of the second lattice when excited within one of its stop bands, while such behavior is not observed for the first lattice.

4.5 Optimization of 2-D rectangular grids

The results presented in the previous sections suggest that the design of the unit cell composing the lattice can be optimized in order to enhance the attenuation characteristics of the lattice. The sensitivity studies performed on the considered configurations have shown that a general tendency for reducing the angle of propagation within the first phase constant surface frequency range requires increasing the diameter of the diagonal components with respect to those of the horizontal and vertical elements. This however tends to reduce the width of the band-gap. An optimization procedure is implemented in order to identify optimal diameter ratio values in order to achieve the multiple objective of reducing the angular range of propagation at low frequencies, while extending the high frequency band-gap.

4.5.1 Design variables and objective functions

The two design variables $d_2 = D_2/D_1$ and $d_3 = D_3/D_1$ are constrained within the following intervals:

$$\begin{aligned} d_2 &\in [\ 0.5 \quad 2.5\ ] \\ d_3 &\in [\ 0 \quad 2.5\ ] \end{aligned}$$

The objective function to be minimized can be expressed as:

$$F(d_2, d_3) = -w_1\overline{F_1}(d_2, d_3) + w_2\overline{F_2}(d_2, d_3) + w_3\overline{F_3}(d_2, d_3) \tag{74}$$

In eq. (74), $\overline{F_1}$ is the normalized width of the band gap, $\overline{F_2}$ is the normalized band gap's center frequency, while $\overline{F_3}$ measures the extension of the angular range over $\Omega \in [0 \quad 1.1]$. For all terms in eq. (74), normalization is performed with respect to the values obtained with the design variables set at the upper limits of the design space. Also in eq. (74), w_i $(i = 1, .., 3)$ are the weights which can be varied in order to attribute more importance to each of the terms of the objective function.

4.5.2 Optimization Results

The optimization problem described in the previous section is solved by using the gradient based, constrained optimization routine `fmincon` in MATLAB®. Several starting points were used in the optimization process and all points converged to the identical solution. However, without an exhaustive search on the design space, it is not possible to state definitively that the converged solution is indeed the global optimum. The solution is carried out for various combinations of the weights w_i $(i = 1, .., 3)$, first to evaluate optimal configurations for the single objectives as well as for the combined performance index described by eq. (74). A summary of the considered optimization problems and of the obtained results is given in Table 10. The presented results confirm the trends highlighted by the sensitivity analysis. For instance, the largest band gap is obtained for an optimization problem with $w_1 = w_2 = 1$, $w_3 = 0$, (see Fig. 51.a), which results in a lattice with $d_3 = 0$, and d_2 coinciding with the upper boundary of the design space. Such enhancement of the band-gap characteristics is however achieved at the expenses of the low frequency directionality (see Fig. 51.b). On the other hand, optimizing for directionality only gives a very narrow band gap (see Fig. 52).

The performance of the lattice obtained from the complete optimization analysis, i.e. for $w_1 = w_2 = w_3 = 1$ compromises the two behaviors and provides both a significant band-gap width and significant directionality Fig. 53).

Table 10: Summary of optimization results

	$w_1 = w_2 = 1,\ w_3 = 0$	$w_3 = 1,\ w_1 = w_2 = 0$	$w_1 = w_2 = w_3 = 1$
d_2	2.50	1.67	2.28
d_3	0	2.49	1.67

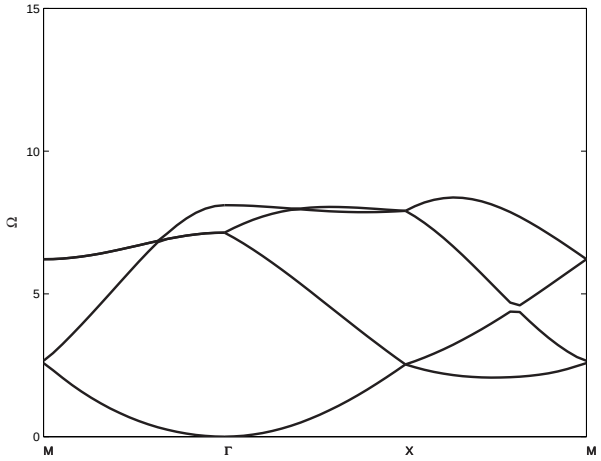

(a) Dispersion

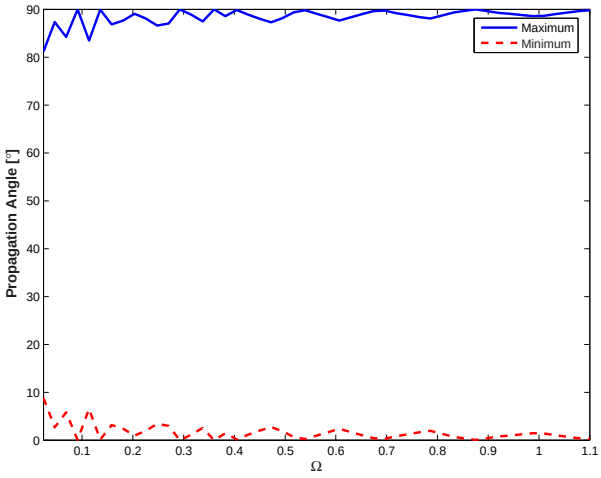

(b) Directionality

Figure 51: Performance of optimal lattice with $d_2 = 2.5$, $d_3 = 0$ ($w_1 = w_2 = 1$, $w_3 = 0$)

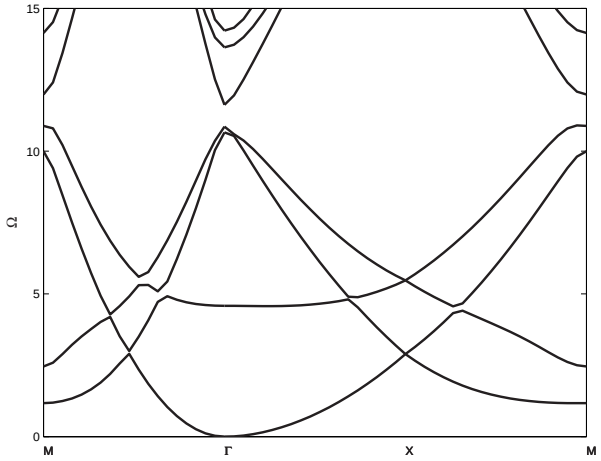

(a) Dispersion

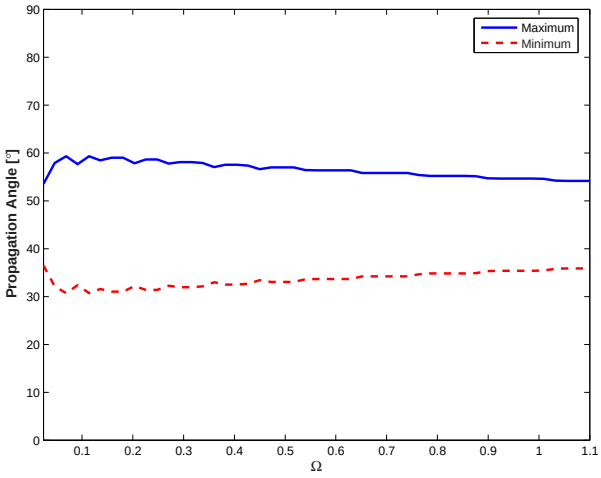

(b) Directionality

Figure 52: Performance of optimal lattice with $d_2 = 1.67$, $d_3 = 2.49$ ($w_3 = 1$, $w_1 = w_2 = 0$)

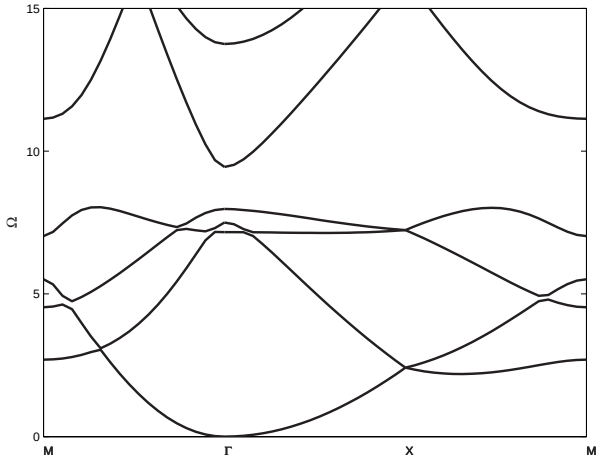

(a) Dispersion

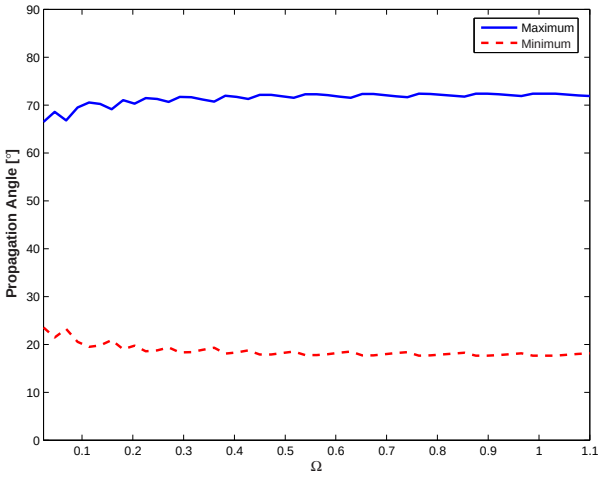

(b) Directionality

Figure 53: Performance of optimal lattice with $d_2 = 2.27$, $d_3 = 1.68$ ($w_1 = w_2 = w_3 = 1$)

CHAPTER V

EXPERIMENTAL INVESTIGATIONS: RECTANGULAR GRID

5.1 Overview

Limited work has been done in the experimental demonstration of the unique dynamic characteristics of 2-D periodic cellular structures. To the author's knowledge Langley and Bardell's [47] investigations of a beam grillage remains the only experimental work done. Their study presented a good demonstration of the directional behavior of a beam grillage but their experimental results showed only fair agreement with theoretical predictions. To this date, no work has been done to experimentally demonstrate the band-gap behavior of 2-D periodic structures. The objective of this chapter is to verify this behavior by considering a rectangular lattice made up of the unit cell shown in Fig. 54, where w_1 and w_2 represent the width of each beam element. The thickness of the members is fixed, however the width is allowed to vary periodically along the x and y directions according to the considered configuration. This simple design was chosen on the basis of the analysis done in Chapter 4 which indicates that cells with no diagonal members have band-gaps over larger frequency ranges and that the gaps generally occur at lower frequency. Since the experimental work has primarily the objective of observing the band-gap phenomenon, the unit cell configuration given in Fig. 54 is selected.

5.2 Manufacturing Considerations

Manufacturing of periodic cellular structures can be a challenging task as conventional manufacturing techniques are too costly and/or inadequate. 3-D stereolithography was initially proposed as a solution, however this technique had several limitations. First, lattices manufactured via stereolithography can only be made from two different types of ABS plastic; hence, selection of material is very limited. Additionally, the viscoelastic properties of ABS plastic makes the prediction of the dynamic behavior over a wide frequency range difficult. In fact, the information showing the variation of material properties over large frequency

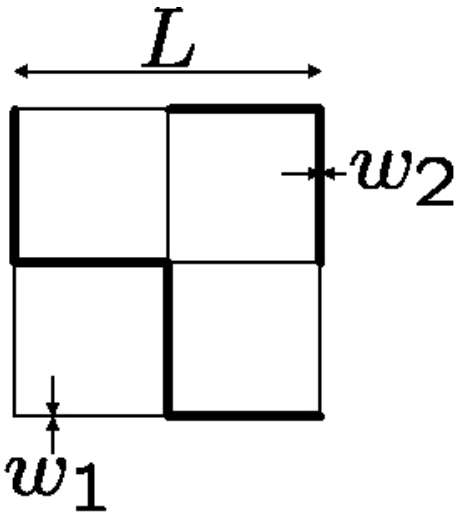

Figure 54: Unit Cell of Experimental Lattice

ranges, known as "master curves", are not easily available for ABS plastic. Hence it is not possible to accurately model the frequency dependence of Young's Modulus and loss factor for the material.

Ultimately, the experimental specimen had to be manufactured via more conventional methods, where the lattice is machined out of a thin aluminum plate. A 3-D solid model of the lattice is first created in I-DEAS using the Master Modeler (Fig. 55), then the 3-D model is exported to a 2-D schematic using I-DEAS Master Drafter. Finally, the model is exported to a 2-D drawing format as required by the Fadal 15XT machining system.

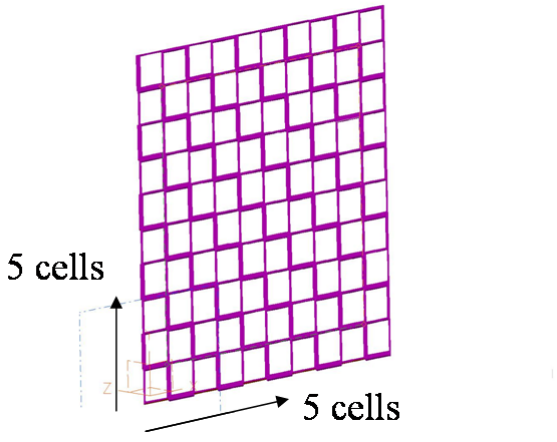

Figure 55: 3-D Model of Lattice

5.3 Configuration of Experimental Lattice

The largest band-gap at the lowest possible frequency is generally desirable. It is found through numerical analysis that the thinner the specimen, the lower the frequency range over which the band-gap phenomenon can be observed. However, if the specimen is too thin, warping will occur during the manufacturing process because of the amount of material being removed. On the other hand, if the specimen is too thick, band-gap behavior will occur at very high frequencies, difficult to observe experimentally. Through trial and error, a 1/16" aluminum plate was selected as the best compromise and was used to manufacture the experimental specimen shown in Fig. 56.

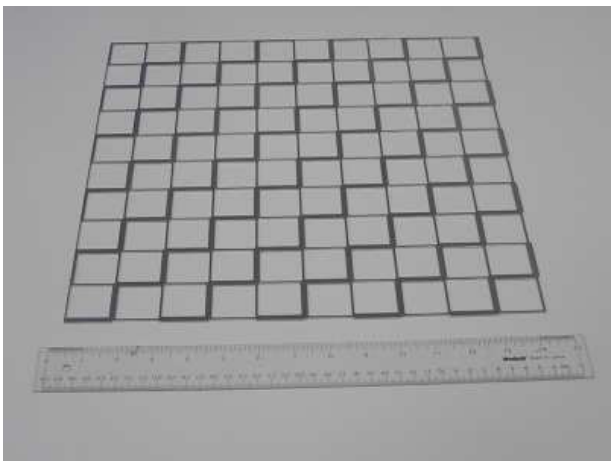

Figure 56: Lattice Specimen

In addition, the Fadal 15 XT machining system has an operating width of about 16", hence the total width of the specimen could not exceed that length. Given these constraints, a design decision was made to manufacture a 5 by 5 lattice measuring between 10" and 16". The width of the first beam member, w_1 was also selected to be 1/16" to give the first beam member a square cross-section. The final parameter, w_2, was finally selected through a parametric study using the computational tools developed in this work. The band-gap predictions for various configurations are listed in Table 11.

The influence of the length of the unit cell, L, and the width of the second beam members, w_2, are clearly seen in this parametric study. The longer the unit cell, the lower

Table 11: Parametric Study for Lattice Configuration

		Band-gap Frequencies		
L (in)	w_2/w_1	Start (Hz)	End (Hz)	Width (Hz)
2	1	0.00	0.00	0.00
2	2	5449.00	5789.70	340.70
2	3	5111.70	5939.40	827.70
2	4	4794.30	5995.40	1201.00
2.2	1	0.00	0.00	0.00
2.2	2	4503.70	4795.80	292.18
2.2	3	4226.20	4932.10	705.93
2.2	4	3966.60	4998.20	1031.50
2.4	1	0.00	0.00	0.00
2.4	2	3784.60	4036.90	252.32
2.4	3	3552.30	4159.50	607.27
2.4	4	3335.80	4227.90	892.07
2.6	1	0.00	0.00	0.00
2.6	2	3224.90	3444.40	219.52
2.6	3	3027.50	3554.30	526.83
2.6	4	2844.20	3621.20	777.06
2.8	1	0.00	0.00	0.00
2.8	2	2780.70	2973.10	192.38
2.8	3	2610.90	3071.60	460.72
2.8	4	2453.60	3135.30	681.72
3.0	1	0.00	0.00	0.00
3.0	2	2422.40	2592.20	169.77
3.0	3	2274.70	2680.60	405.89
3.0	4	2138.20	2740.40	602.14

the frequency at which the band-gap behavior can be first observed. Additionally, the larger the ratio between the two members' widths, the wider the band-gap. Ideally, the configuration that gives the widest possible band-gap at the lowest observable frequency is desired. Taking into account the manufacturing constraints, the final configuration for the unit cell and the material properties of the aluminum used are summarized in Table 12.

Table 12: Mechanical properties and geometry of experimental lattice.

Property	Value	Units
Young's Modulus	7.0×10^{10}	Pa
Density	2700	kg/m^3
Poisson's Ratio ν	0.3	
D_1	$\frac{1}{16}$	in
D_2	$\frac{3}{16}$	in
Unit Cell Length L	2.8	in

5.4 Experimental Validation

The computational tools used to compute the harmonic response of the specimen are first validated experimentally. The validation is done by comparing the measured frequency response versus the computed response. The specimen is clamped at one corner and excited near the clamped edge. The harmonic response is then measured at the furthest corner from the point of excitation. Fig. 57 shows the clamped specimen and the point of excitation near the clamped corner. Fig. 58 shows the comparison between the experimentally measured and the computed response over the $0 - 100$ Hz range. The numerical data shows excellent agreement with the experimental data. Over wider frequency ranges, the comparison becomes hard to visualize, as the modal density becomes very high.

5.5 Experimental Setup for Band-gap Analysis

Vibrations at a point in a structure can easily be measured by attaching an accelerometer at a given location. However, the measurement of the complete wave field cannot be done using the same method. The number of accelerometers needed to reconstruct the complete wave

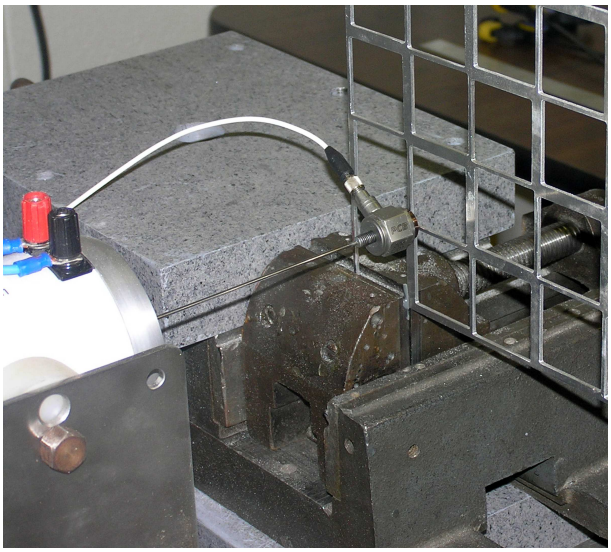

Figure 57: Clamped Corner and Point of Excitation

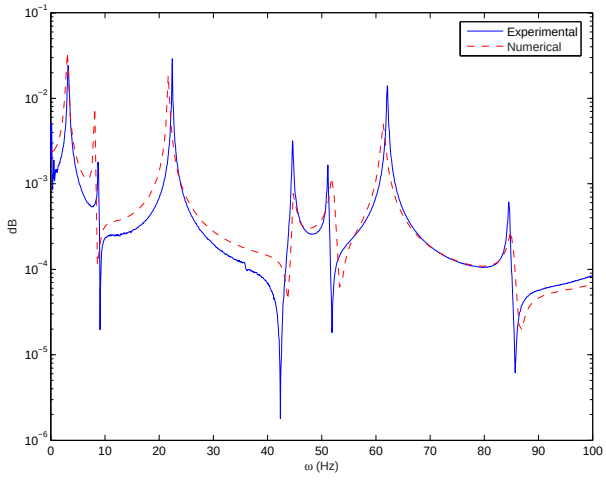

Figure 58: Frequency Response Comparison

field would be prohibitively large, making the traditional method practically unfeasible. Advances in experimental instrumentation provides a solution in the form of a Scanning Laser Doppler Vibrometer (SLDV). SLDV uses the doppler effect to measure displacements and/or velocities of the specimen, and it is able to take measurements on several locations quickly and non-instrusively. The SLDV that will be used in the experimental validation is a Polytec PSV-400 scanning head.

The complete vibration field of the experimental specimen at several frequencies is measured to study its dynamic characteristics. These experimental observations are then compared to the numerical predictions found using the developed computational tools.

The lattice is harmonically excited at various frequencies to determine if attenuation in band-gaps can be observed as predicted by the computational simulations. The lattice is suspended to emulate free-free boundary conditions and is excited at one corner of the lattice. The excitation location is represented by the circle in the lower left corner in Fig. 59. Table 13 summarizes the instrumentation used in the experiments.

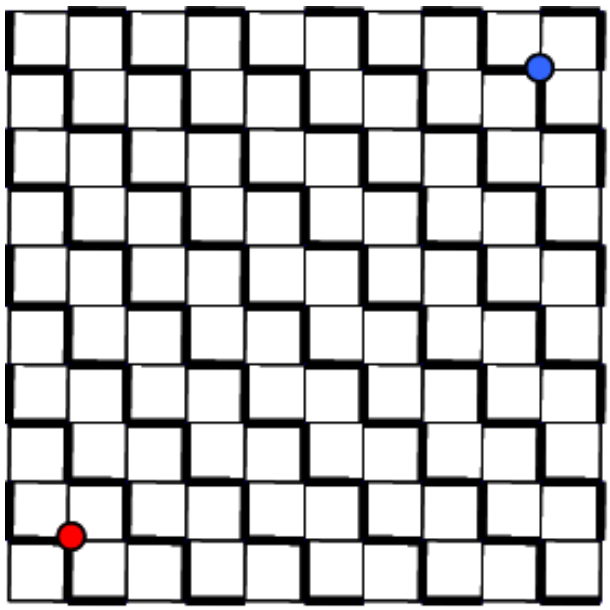

Figure 59: Lattice Schematic

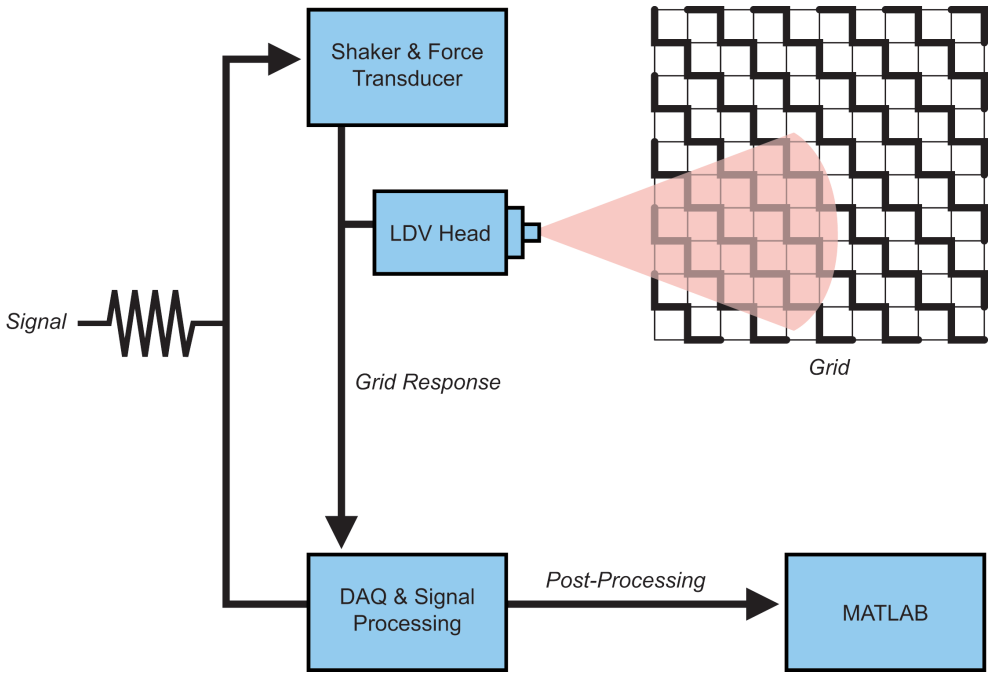

Figure 60: Schematic of experimental setup

Table 13: Experimental Equipment

Part	Manufacturer	Model No.
SLDV	Polytec	PSV-400
SLDV Controller	Polytec	OFV-5000
DAQ System	Polytec	PSV-W400M2
Mechanical Shaker	Ling Dynamic Systems	V203

5.6 Experimental Results

The frequency response function of a point at the upper right hand corner (upper right circle in Fig. 59.a) on the lattice is shown in Fig. 61. The results show that the band-gap behavior is observed around 2900 Hz and 3200 Hz as denoted by the two dashed lines in Fig. 61. This is slightly different from the computational model, which predicted a band-gap between 2611 Hz and 3072 Hz. This difference is graphically shown in Fig. 62, where the shaded area denotes the band-gap predicted by the computational model and the two dashed red lines represent bounds of the experimentally observed band-gap. The agreement between

the numerical predictions and experimental data is acceptable, however some discrepancy can be clearly observed. The reasons for these differences has not been fully investigated due the limitations in time and cost required to perform various experiments on several specimens. However a number of hypotheses can be formulated. First of all, it should be noted how the band-gaps in the computational model are predicted through the analysis of the dispersion relation performed on the unit cell, while in the experiments, the bounds are only estimated from the measured harmonic response of the finite lattice. In addition, manufacturing imperfections may lead to non-perfect periodicity, which may slightly alter the location of the band-gap for the assembly. Previous work has shown how small levels of aperiodicity in a nominally periodic assembly may in fact alter the bounds of the band-gaps [48]. In addition, the model considered for the unit cell analysis does not include damping, while in the experimental specimen some dissipation is certainly expected. While damping does not generally shift the band-gaps (see [37]), it may make the estimation of their upper and lower bounds harder to estimate from harmonic response plots. Finally, our computational model idealizes the lattice as an assembly of 1-D beam elements, while in reality the lattice is made of beams with a finite in-plane width. The difference between real and idealized grid may become noticeable in the frequency range where the band-gap is detected.

The complete vibration field at various frequencies are reproduced in MATLAB®by post-processing the acquired data. Figs. 63.a-65.a show the amplitude of the harmonic response of the lattice at 2500 Hz, 3000 Hz and 3200 Hz respectively. Figs. 63.b- 65.b show the same deformation but displayed as a colormap of the interpolated displacements over the whole lattice. Figs. 63 and 65 clearly show that waves are free to propagate through the lattice and there is no attenuation. However, Fig. 64 indicates that at that frequency, waves are attenuated and vibration is localized to the area around the point of excitation. To verify that the behavior observed at 3000 Hz is not due to anti-resonance, the harmonic response at two other frequencies within the band-gap is measured. The harmonic response at 3050 Hz is similar to that observed at 3000 Hz, vibration in the lattice is isolated to the area around the point of excitation. Less attenuation is observed at 3100 Hz, but it is still

evident that the vibration is still localized to the region of excitation.

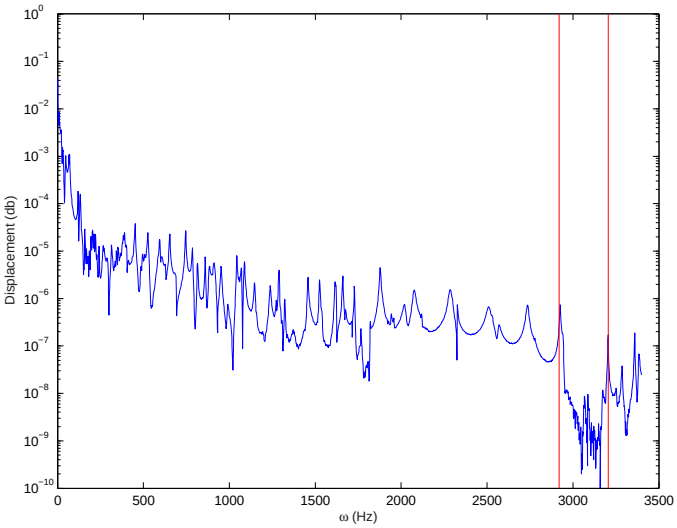

Figure 61: Experimental Frequency Response Function

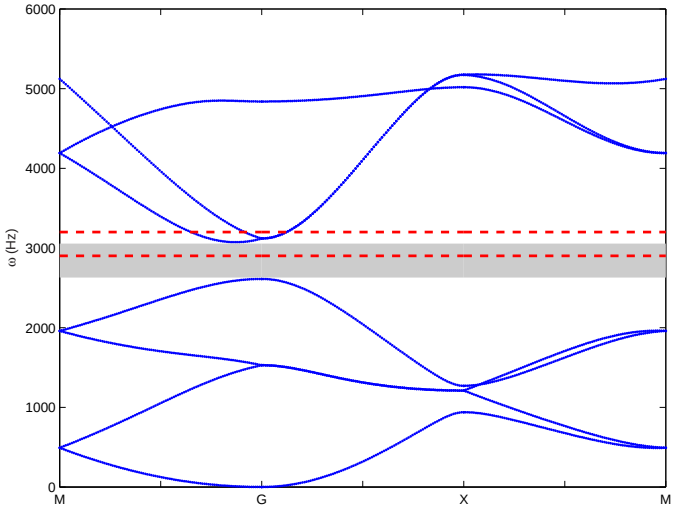

Figure 62: Experimental and Computational Band-gap

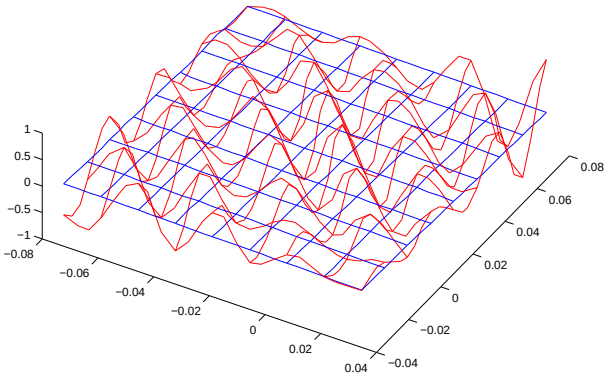

(a) Deformed grid

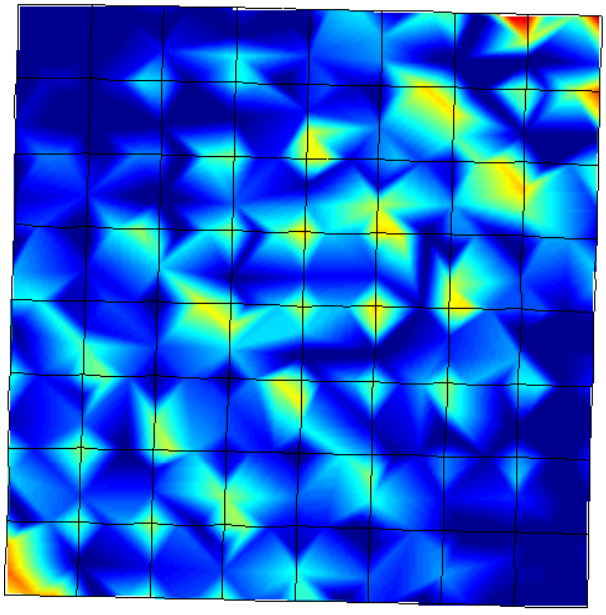

(b) Color map of deformation

Figure 63: Harmonic response at 2500 Hz

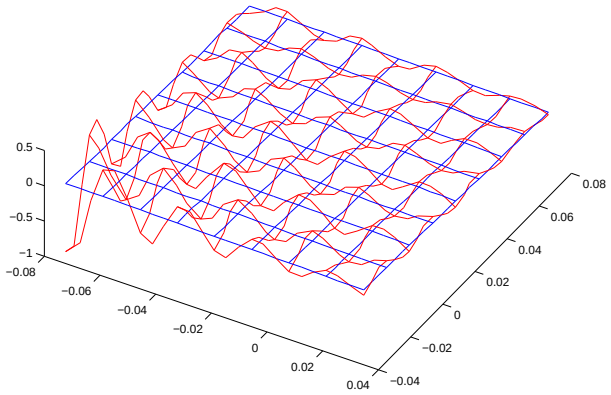

(a) Deformed grid

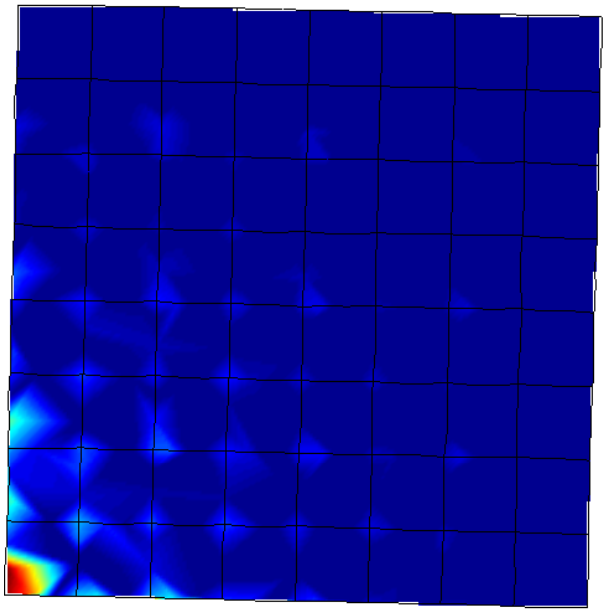

(b) Color map of deformation

Figure 64: Harmonic response at 3000 Hz (Band-gap)

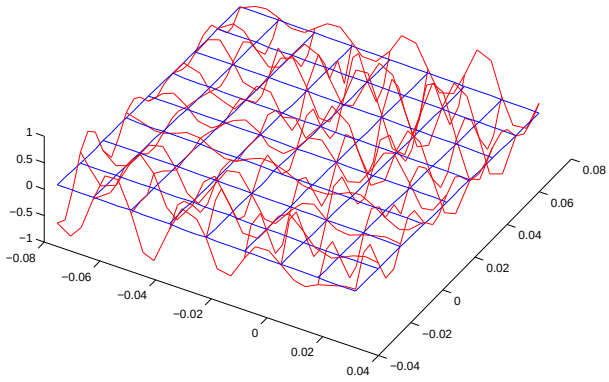

(a) Deformed grid

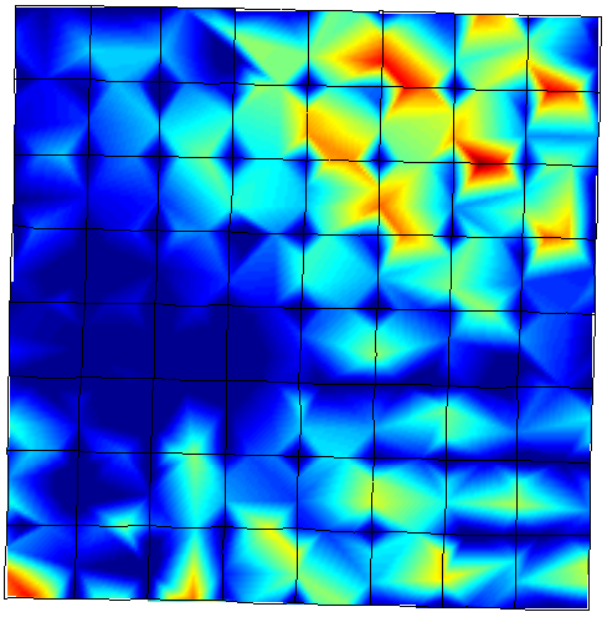

(b) Color map of deformation

Figure 65: Harmonic response at 3200 Hz

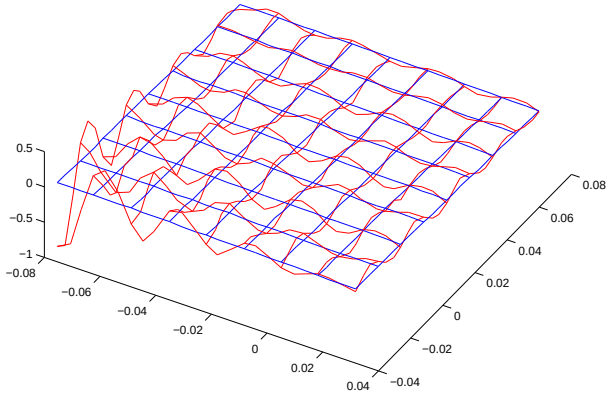

(a) Deformed grid

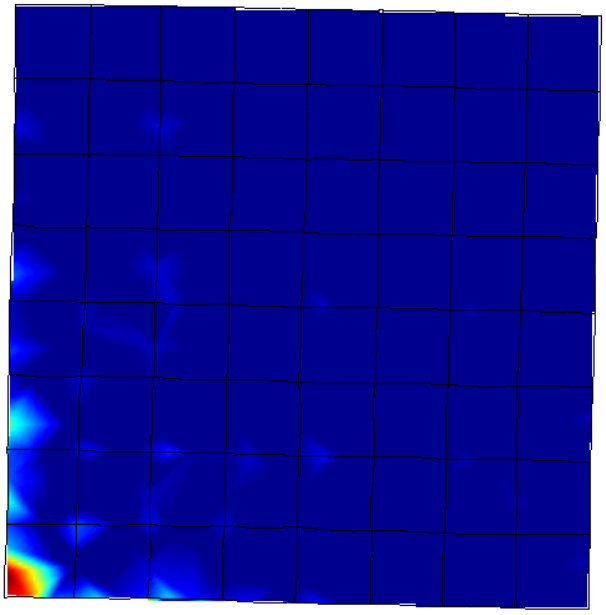

(b) Color map of deformation

Figure 66: Harmonic response at 3050 Hz (Band-gap)

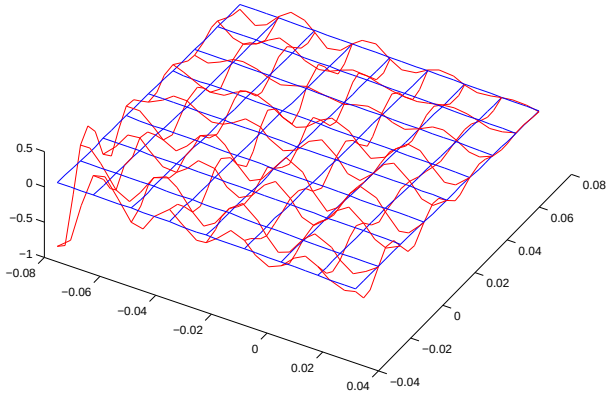

(a) Deformed grid

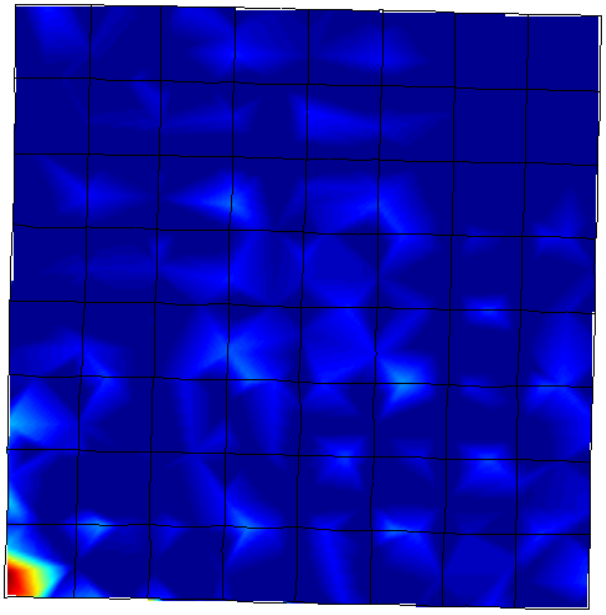

(b) Color map of deformation

Figure 67: Harmonic response at 3100 Hz (Band-gap)

CHAPTER VI

CYLINDRICAL GRIDS

6.1 Overview

In this chapter the study of wave propagation of a 2-D periodic cellular structure is extended to the more complex geometry of cylindrical lattices. In this analysis, the objective is to investigate the directional and bandgap behavior of two different types of cylindrical grids. The first grid is composed of curved rectangular unit cells (Fig. 68.a), while the second is composed of curved hexagonal unit cells (Fig. 69.a). Both unit cells are made up of curved or straight beams rigidly connected to each other. The objective of this double analysis is to assess the influence of both unit cell geometry and topology on the wave propagation characteristics of the assembly. The investigation of cylindrical grids is of practical relevance as grid stiffened composite shells and shrouds, or integrally stiffened cylindrical components can be considered as practical implementation of the considered geometries [13]. The investigations here presented may provide guidelines for the design of innovative configurations for grid stiffened or integrally stiffened assemblies. The resulting wave attenuation capabilities may be beneficial to reduce vibrations, and may also have important implications on the sound radiation characteristics of this class of structures.

The cylindrical unit cells are modeled using the general beam element formulation described in Chapter 3. The computational cost for the evaluation of the harmonic response of the entire structural assembly is reduced by taking advantage of the rotational periodicity of the structure, which allows a significant reduction of the required degrees of freedom. Details of this reduction technique are presented in the next section.

6.2 Harmonic Response of Rotationally Periodic Structures

Rotationally periodic structures consist of a number of identical elements or 'strips' connected to form a closed ring [49, 50] (Fig. 70). Accordingly, their geometry at a given angular position θ is identical to the geometry at the angle $(\theta + 2\pi n/N)$, where N is the number of periodic strips in the complete structure and n is an integer varying between

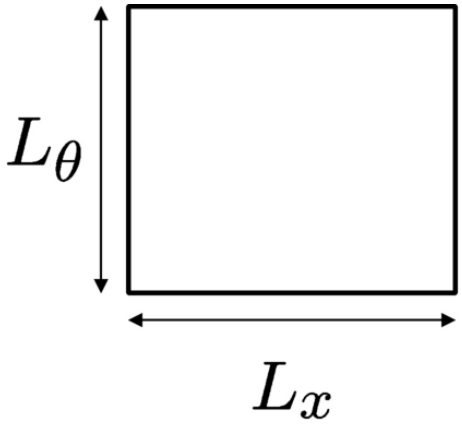

(a) Unit cell

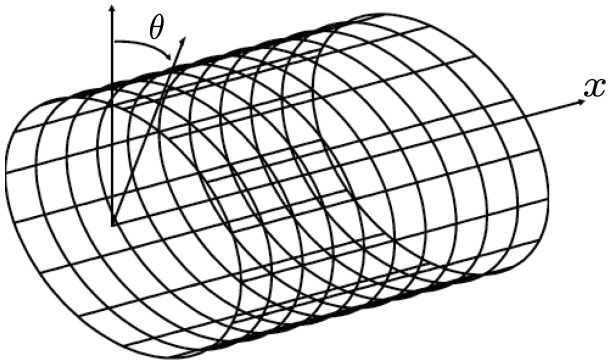

(b) Grid

Figure 68: Curved rectangular cell and grid

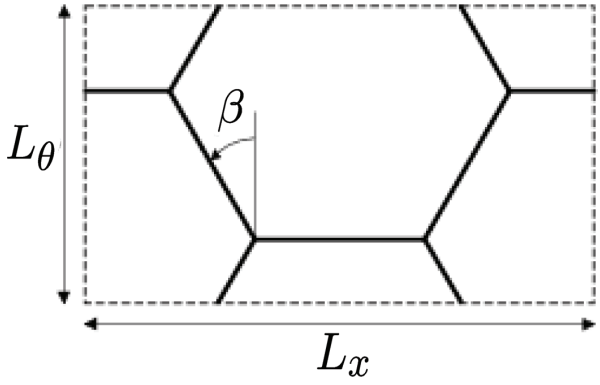

(a) Unit cell

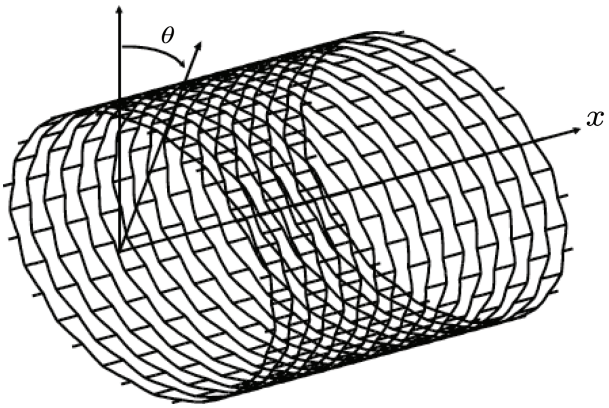

(b) Grid

Figure 69: Hexagonal cell and grid

0 and N. The rotational periodicity allows the analysis to be performed by considering a single strip with imposed periodic boundary conditions (Fig. 70).

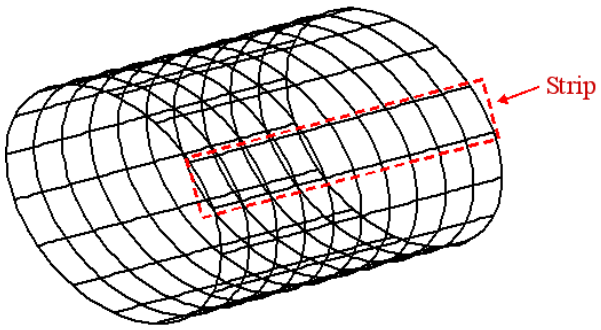

Figure 70: Rotationally Periodic Assembly

6.2.1 Equivalent nodal load

According to Petyt [50], the equivalent nodal force on the s^{th} strip due the applied external loads can be expressed as:

$$\underline{F}^{(s)} e^{i\omega t} = \sum_{p=1}^{N} \left(\underline{Q}_p e^{i(\omega t - 2\pi(s-1)p/N)} \right) \tag{75}$$

where $\underline{Q}_p$ defines the magnitude of the equivalent nodal loads on the p^{th} strip. From eq. (75), the force on the first strip is simply:

$$\underline{F}^{(1)} e^{i\omega t} = \sum_{p=1}^{N} \left(\underline{Q}_p e^{i\omega t} \right) \tag{76}$$

and the forces in subsequent strips are identical except for a phase difference $\epsilon = 2\pi p/N$. Expressing eq. (75) in matrix form gives:

$$\mathbf{F} = \mathbf{Q}\mathbf{\Phi} \tag{77}$$

where the s^{th} column of $\mathbf{F}$ is $\underline{F}^{(s)}$, the p^{th} column of $\mathbf{Q}$ is $\underline{Q}_p$, and $\mathbf{\Phi}$ is a $N \times N$ Hermitian matrix [49] whose (p, s) element is $e^{(-i2\pi p(s-1)/N)}$. Hence, $\mathbf{Q}$ is simply,

$$\mathbf{Q} = \mathbf{F}\mathbf{\Phi}^H \tag{78}$$

6.2.2 Reduced equation of motion

The response of the structure to each of the N harmonic terms in eq. (75) can be obtained from a separate analysis. Each component induces a deflection of the structure with the same frequency and phase variation, which can therefore be expressed as:

$$\underline{\delta}^{(s)} = \mathbf{W} \left\{ \begin{array}{c} \underline{\delta}_L \\ \underline{\delta}_I \end{array} \right\}_p^{(s)} \tag{79}$$

where $\underline{\delta}_I$ and $\underline{\delta}_L$ denote vectors containing the intermediate nodal degrees of freedom and those on the left boundary of the considered strip. Matrix $\mathbf{W}$ is defined in terms of the phase difference ϵ associated to the component of the considered set of loads. Matrix $\mathbf{W}$ is given by:

$$\mathbf{W} = \left[\begin{array}{cc} \mathbf{I} & 0 \\ e^{\epsilon} & 0 \\ 0 & \mathbf{RI} \end{array} \right] \tag{80}$$

where $\mathbf{R}$ is a rotation matrix that transforms the displacements of the nodes to the right of the considered strip from the global coordinate system into the local coordinates of the left nodes. Such a transformation is required to enforce the compatibility of displacements after imposing the phase difference ϵ and therefore to satisfy the conditions of rotational periodicity.

The force acting on a single substructure can be considered as composed of a combination of external loads and boundary forces. Accordingly, the total force acting on the s^{th} strip $\underline{F}^{(s)}$, can be written as:

$$\underline{F}^{(s)} = \left\{ \begin{array}{c} \underline{F}_L^{(e)} \\ \underline{F}_I^{(e)} \\ \underline{F}_R^{(e)} \end{array} \right\}^{(s)} + \left\{ \begin{array}{c} \underline{F}_L^{(b)} \\ 0 \\ \underline{F}_R^{(b)} \end{array} \right\}^{(s)} \tag{81}$$

where the superscripts (e) and (b) respectively denote external loads and boundary forces. Using eq. (81) and following a reduction analysis similar to the one presented in Chapter

2, one obtains:

$$\left\{ \begin{array}{c} \underline{F}_L^e \\ \underline{F}_I^e \\ \underline{F}_R^e \end{array} \right\}^{(s)} = \left\{ \begin{array}{c} \underline{Q}_L \\ \underline{Q}_I \\ e^{i\epsilon}\underline{Q}_L \end{array} \right\}_p^{(s)} \tag{82}$$

where $\underline{Q}_L$ and $\underline{Q}_I$ are the loads acting on the left and interior nodes of the s^{th} strip respectively and where $\epsilon = 2\pi p/N$, with p denoting one of the components in eq. (75). The equation of motion of the s^{th} strip can be generally expressed as:

$$\left(\mathbf{K}^{(s)} - \omega^2 \mathbf{M}^{(s)}\right) \underline{\delta}^{(s)} = \underline{F}^{(s)} \tag{83}$$

where $\mathbf{K}^{(s)}$, $\mathbf{M}^{(s)}$ are respectively the stiffness and mass matrix for the considered strip, while $\underline{F}^{(s)}$ is the vector of the applied loads. Substituting eq. (79) into eq. (83) and premultiplying by $\mathbf{W}^H$ gives:

$$\left(\mathbf{K}_r^{(s)}(\epsilon) - \omega^2 \mathbf{M}_r^{(s)}(\epsilon)\right) \left\{ \begin{array}{c} \underline{\delta}_L \\ \underline{\delta}_I \end{array} \right\}_p^{(s)} = \left\{ \begin{array}{c} 2\underline{Q}_L \\ \underline{Q}_I \end{array} \right\}_p^{(s)} \tag{84}$$

where

$$\mathbf{K}_r^{(s)}(\epsilon) = \mathbf{W}^H \mathbf{K}^{(s)} \mathbf{W} \tag{85}$$

$$\mathbf{M}_r^{(s)}(\epsilon) = \mathbf{W}^H \mathbf{M}^{(s)} \mathbf{W} \tag{86}$$

Eq. (84) is solved N times corresponding to the components in eq. (75). The complete set of displacements for the strip can be then obtained from eq. (79). For the considered N values of ϵ the total displacements of the entire structure are obtained from:

$$\mathbf{U} = \mathbf{\Delta}\mathbf{\Phi} \tag{87}$$

where $\mathbf{\Delta}$ is a $N \times N$ matrix whose columns are the N solutions of eq. (84) and the s^{th} column of matrix $\mathbf{U}$ describes the displacement of the s^{th} substructure.

Table 14: Geometry and material properties of cylinder

Property	Value	units
Length-to-radius L/R	10	
Young's Modulus E	7.0×10^{10}	Pa
Density ρ	2700	kg/m^3
Poisson's ratio ν	0.3	

6.3 Cylindrical Grid Configurations

The wave propagation characteristics of rectangular and hexagonal cell topologies are analyzed. For both configuration, the cylindrical grids are considered with a length-to-radius ratio of 10/1. All the grids are composed of 16 cells around the circumference and 10 cells along the axial direction. The overall dimensions of the cylindrical structure, and the considered material properties are listed in Table 14. These material properties are used as a reference, but do not influence the non-dimensional results presented in this chapter.

The rectangular topology is obtained by the assembly of two straight beams and two curved beams of square cross section that are rigidly connected to each other at the joints. The cross section of the two curved beams and the overall dimensions of the cell are kept constant, while the cross section of the straight beam (thick lines in Fig. 68.a) is varied. The length of the side of the cross section for the curved beams is denoted as a_0, while the side of the straight beam is a. The performance of the rectangular grid is investigated in terms of the ratio $\alpha = a/a_0$, with the following considered values: $\alpha = 1$, $\alpha = 2.5$, $\alpha = 5$. The results are normalized in terms of a frequency parameter of the kind described in Chapter 4 (eq. (73)), in here the dimensions and the material properties of the straight beams with $\alpha = 1$ are used. Given this configuration, the non-dimensionalization parameter is $\omega_0 = 14.7$ rad/s. The validity of the non-dimensionalization strategy has been tested in a way similar to the one presented in Chapter 4, but the results of these investigations are omitted for the sake of brevity.

The curved hexagonal grids are obtained by the assembly of 9 curved beams (see Fig. 69.a). The overall dimensions of the hexagonal cell L_x, L_θ are kept constant throughout the study. The only factor that is varied is the angle, β (see Fig. 69.a). The considered

angles are $\beta = 30°$, which defines a regular hexagonal topology, and $\beta = -30°$, to obtain a re-entrant geometry [6]. The selection of a re-entrant configuration is based on previous work on planar re-entrant lattices shown by Ruzzene et al. [51]. The investigation of cylindrical re-entrant lattices presented in this dissertation represents the natural extension of the results presented in [51]. The non-dimensionalization parameter is computed by considering the dimensions of the straight beam of the unit cell with internal angle $\beta = 30°$. The corresponding value is $\omega_0 = 98.3$ rad/s.

6.3.1 FE discretization of unit cells

The FE mesh considered for the analysis of cylindrical grids is selected through a convergence study aimed at determining the accuracy of the model within a specified frequency range. For rectangular cells, we elect to limit our investigations to $\Omega \in [0\ 200]$, while for the behavior hexagonal grids is investigated for $\Omega \in [0\ 12]$. These ranges are dictated by the choice of limiting the analysis to frequencies which, for the considered number of cells and dimensions, include most of the dynamic behavior of the assembled grid. For the rectangular grid, for example, the considered frequency range includes more than 40 vibrational modes for the grid. Figure 71 for example shows the results of the convergence study on the hexagonal grid with $\beta = 30°$. The plot compares the dispersion relations evaluated with an increasingly refined mesh. The dispersion relations are predicted by considering the contour of the first Brillouin zone shown in Fig. 72. As there is no symmetry in the phase constant surfaces with respect to a 45° line, the boundary $M \rightarrow P \rightarrow G \rightarrow X \rightarrow M$ must be considered. In Fig. **??**, the number of elements in the legend indicate the elements used on each side of the unit cell. Convergence is achieved with 5 elements, as no changes in the dispersion relations are observed by refining the mesh beyond this value. The finite element mesh and geometry for rectangular and hexagonal grids are summarized in Tables 15 and 16.

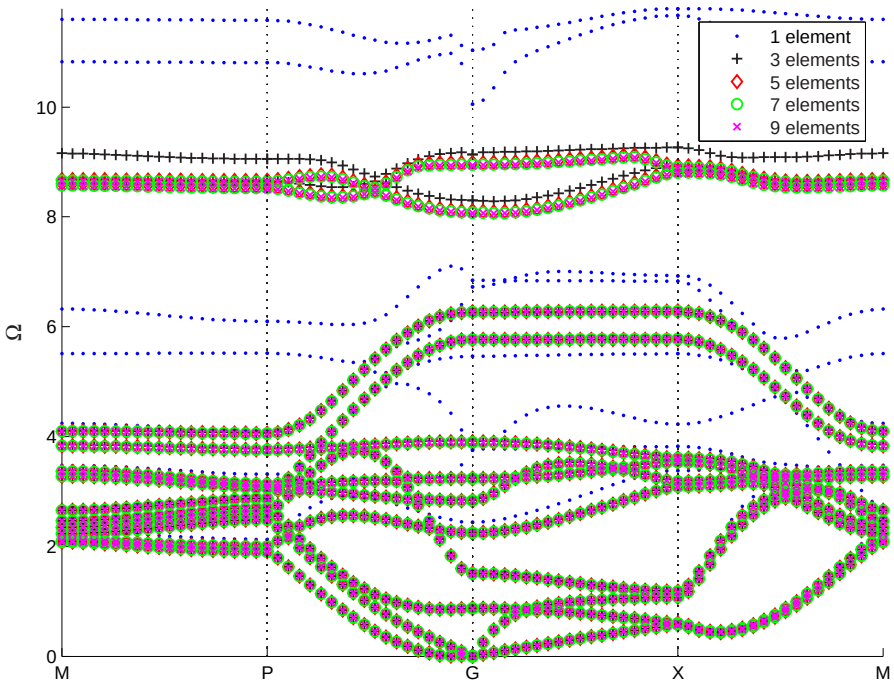

Figure 71: Convergence of dispersion relations

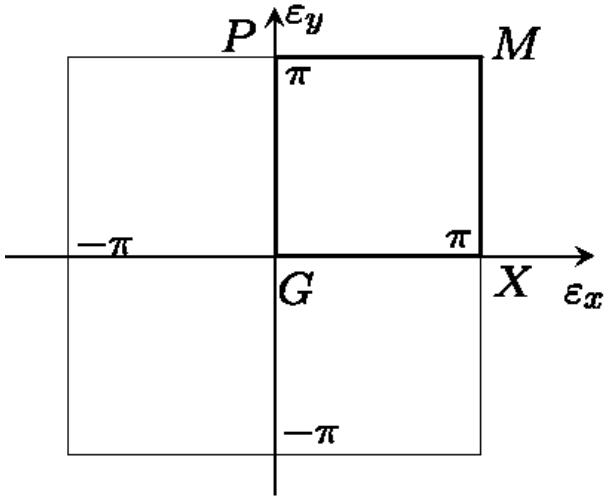

Figure 72: First Brillouin Zone: Rectangular and Hexagonal Cylindrical Grid

Table 15: FE mesh for rectangular cylindrical grids

Number of elements per cell	20
Number of nodes per cell	40
Number of elements per strip	105
Number of nodes per strip	211

Table 16: FE mesh for hexagonal cylindrical grids

Number of elements per cell	45
Number of nodes per cell	91
Number of elements per strip	450
Number of nodes per strip	301

6.4 Performance of rectangular grids

6.4.1 Directional behavior: Phase constant surfaces

The contour maps of the first phase constant surface for the considered rectangular grids are shown in Fig. 73. The isofrequency lines are labeled with the corresponding values of the normalized frequency. As discussed in Chapter 2, and in [51, 52], the perpendicular to each isofrequency contour indicates the direction of wave propagation for the considered pair of propagation constants. Fig. 73.a shows that as frequency increases beyond approximately $\Omega = 6.5$, the iso-frequency lines tend to become almost horizontal and parallel to the ϵ_x axis. This indicates the onset of directionality in the grid. This phenomenon can be clearly shown by computing the propagation angle at various values of Ω. The results of this analysis are summarized in Fig. 74, where plots of the maximum angle of wave propagation versus Ω are presented for two of the considered grid configurations. The analysis is limited to a single quadrant of the phase constant surface, and therefore a maximum angle of 90° indicates a non-directional behavior for the grid, while lower angles correspond to directionality. It is interesting to observe how for both configurations, the transition between directional and non-directional behavior occurs at a specified frequency value which depends upon the unit cell configuration. This frequency value is defined as the "transition frequency". For convenience, the contour corresponding to the transition frequency is highlighted as a solid, thicker line in the phase constant surface contours of Fig. 73. Fig. 73 also shows that modifying the cross section of the straight beams significantly alters the phase constant surfaces. In the grid with $\alpha = 1$, wave propagation above the transition frequency mostly occurs along the circumferential direction (θ), while for $\alpha = 2.5$ and above the corresponding transition frequency ($\Omega = 15$), waves mostly propagate along the longitudinal direction (x). This behavior is also observed at a lower frequency for $\alpha = 5$, where

above the transition frequency of $\Omega = 7.8$ (bold line in Fig. 73.c), wave propagation occurs preferentially along the axial direction (x). These results demonstrate that the directional behavior of rectangular cylindrical grids can be changed by modifying the cell geometry. Proper selection of the geometry of the straight beams in the unit cell, for example, allows switching the directional behavior from the circumferential direction to the axial direction.

6.4.2 Harmonic response

The predictions obtained from the analysis of the phase constant surfaces are validated through the evaluation of the harmonic response of the complete 2-D periodic assembly obtained using the reduction technique previously considered. The response of the first ($\alpha = 1$) and third ($\alpha = 5$) rectangular grid is considered for harmonic excitations of unit amplitude and frequency equal to $\Omega = 5.4$, $\Omega = 7.1$ and $\Omega = 8.5$. A harmonic radial load is applied at a location identified by the following set of cylindrical coordinates: $\theta = \pi$, $z/R = 5$. The results are shown in Figs. 75-76, which show the magnitude of the radial motion of the grid through bi-dimensional maps, obtained by interpolating the grid displacements resulting from the FE analysis. Fig. 75.a shows the harmonic response of the first grid at an excitation frequency of $\Omega = 5.4$. According to the phase constant surface shown in Fig. 73.a, at this frequency waves are free to propagate in both the circumferential and longitudinal directions. Hence no wave attenuation nor directionality of the response are noticeable. However the response at $\Omega = 7.1$ and $\Omega = 8.5$ displayed in Fig. 75.b and Fig. 75.c show significantly different displacement patterns. Both frequencies are in fact above the transition predicted by the phase constant surface, whose analysis indicates that at these frequencies wave propagation occurs preferentially in the circumferential direction. The responses shown in Fig. 75.b and Fig. 75.c confirm such predictions. The harmonic responses of the third grid at $\Omega = 5.4$ and $\Omega = 7.1$ are presented in Fig. 76.a and Fig. 76.b. Both displacement maps indicate that waves are free to propagate in both circumferential and longitudinal directions. However, the harmonic response at $\Omega = 8.5$ shown in Fig. 76.c confirms that this frequency is above the transition between non-directional and directional behavior and that propagation occurs mostly in the longitudinal direction. The results

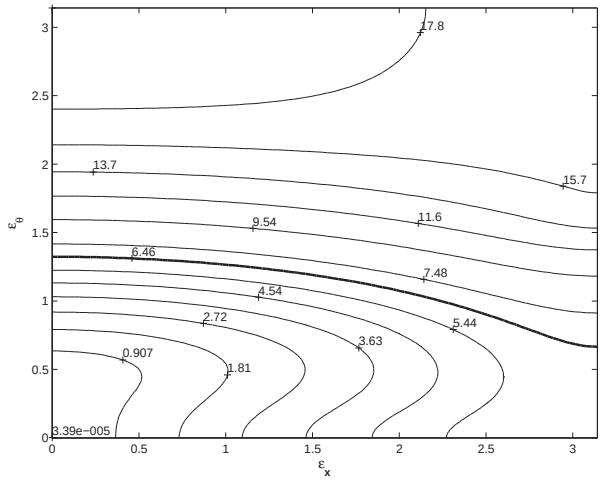

(a) $\alpha = 1$

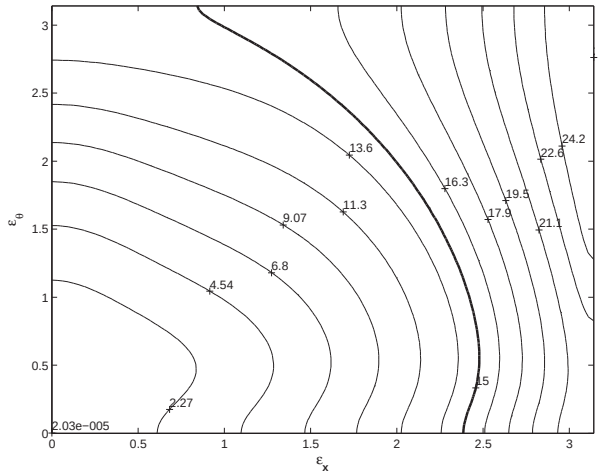

(b) $\alpha = 2.5$

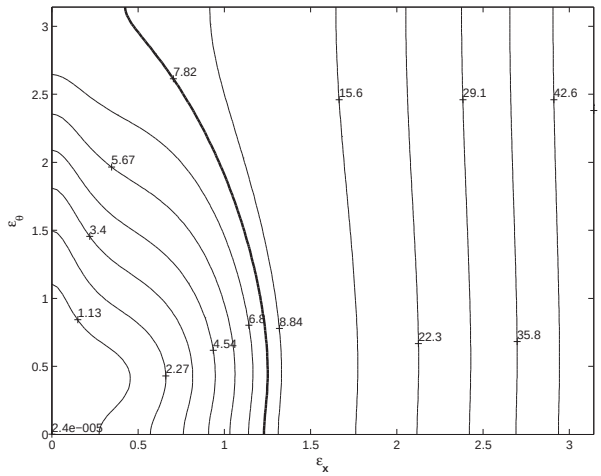

(c) $\alpha = 5$

Figure 73: Phase constant surfaces for rectangular grids (Bold lines: "Transition" frequency)

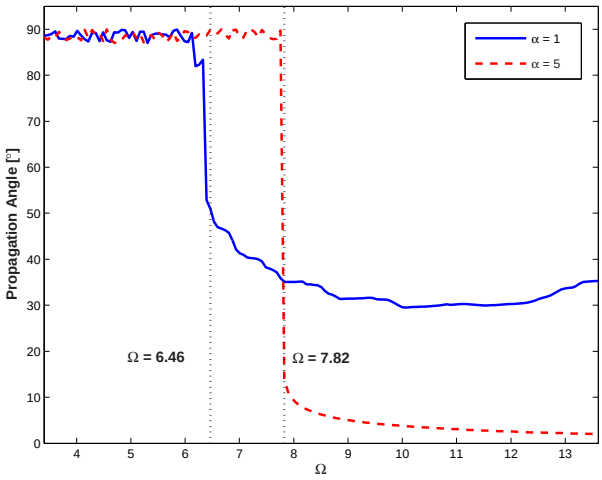

Figure 74: Propagation angles for rectangular grids

presented in this section demonstrate how proper design of the unit cell can effectively control the directions of wave propagation and can modify the frequency of transition between non-directional and directional behavior.

6.4.3 Band-gaps

The band-gap behavior of the considered rectangular cylindrical grids is analyzed by considering the first Brillouin zone of the unit cell for all three grids (Fig. 72). Unfortunately, no band-gap behavior is found for any of the three grids considered (Fig. 77), over the frequency range of interest.

6.5 Performance of hexagonal grids

6.5.1 Phase constant surfaces

The directional and band-gap characteristics of hexagonal grids can be modified by varying the topology of the unit cell through changes in the angle β (see Fig. 69). This is demonstrated by the phase constant surfaces shown in Fig. 78, which compares the characteristics of grids with $\beta = +30°$ and $\beta = -30°$. In the grid with $\beta = 30°$, above the transition frequency of $\Omega = 2.9$ (bold line in Fig. 78.a), wave propagation mostly occurs along the circumferential direction (θ), while for $\beta = -30°$ this transition frequency is lower at $\Omega = 1.4$ (bold line in Fig. 78.b). In both cases the iso-frequency lines above the transition tend to be

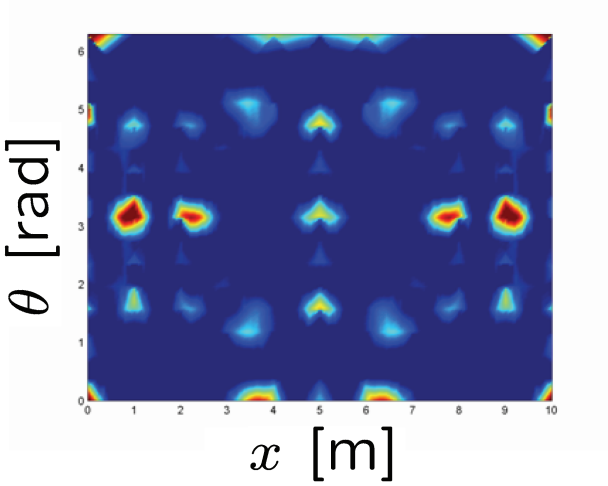

(a) $\Omega = 5.4$

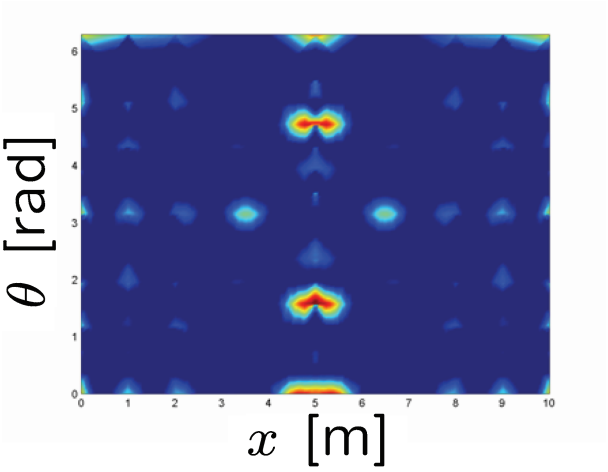

(b) $\Omega = 7.1$

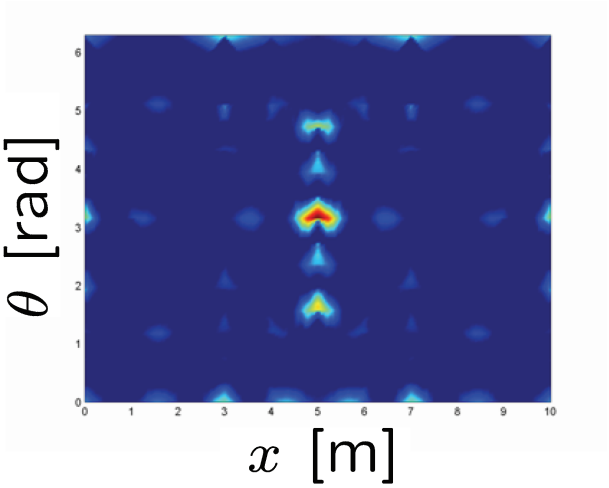

(c) $\Omega = 8.5$

Figure 75: Harmonic response of first rectangular grid ($\alpha = 1$)

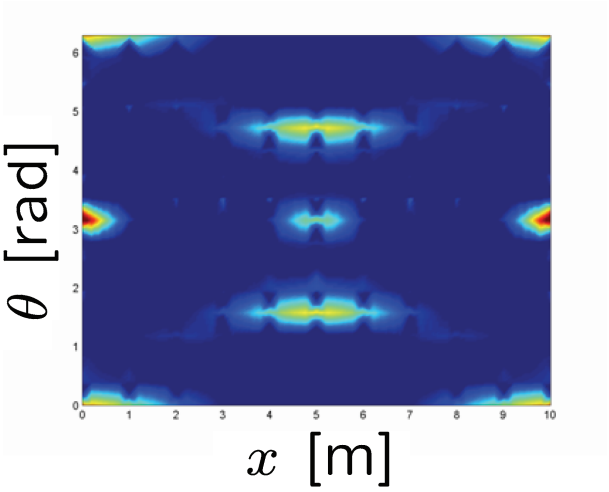

(a) $\Omega = 5.4$

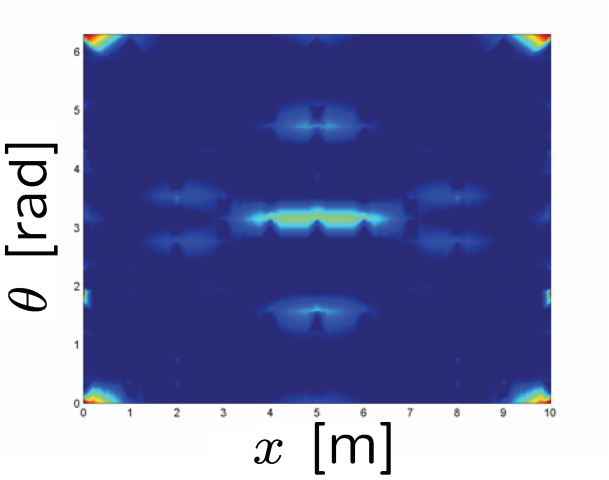

(b) $\Omega = 7.1$

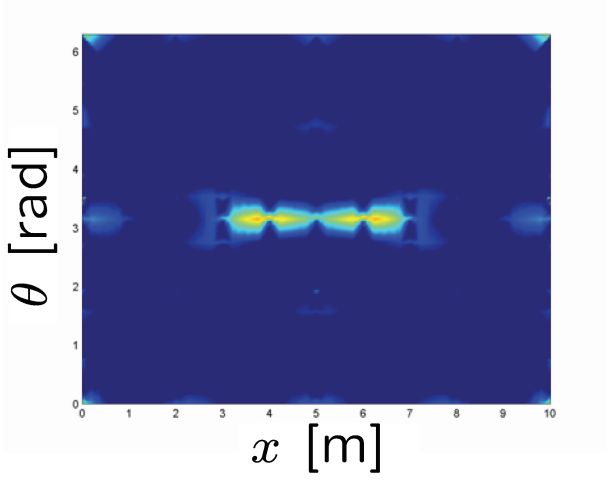

(c) $\Omega = 8.5$

Figure 76: Harmonic response of third rectangular grid ($\alpha = 5$)

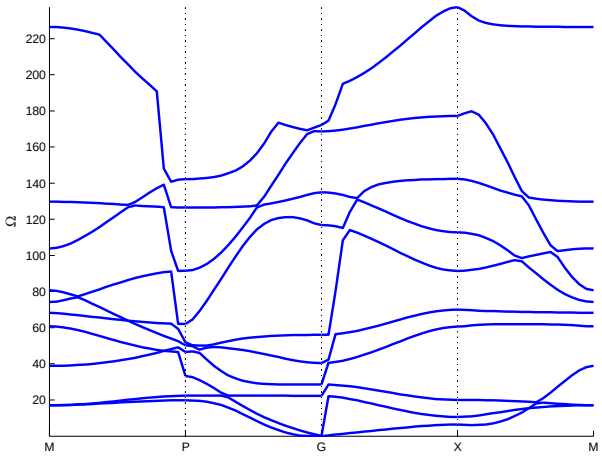

(a) $\alpha = 1$

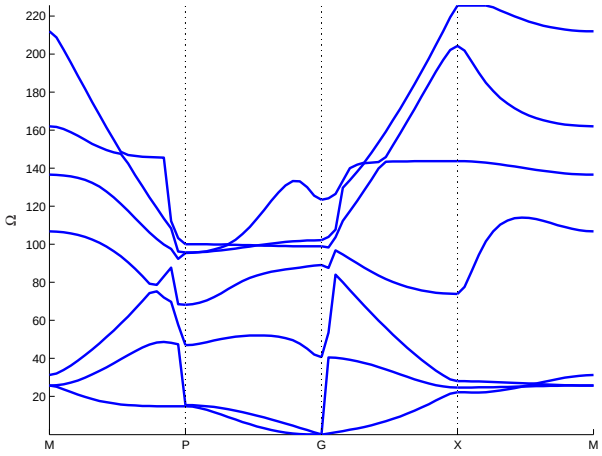

(b) $\alpha = 2.5$

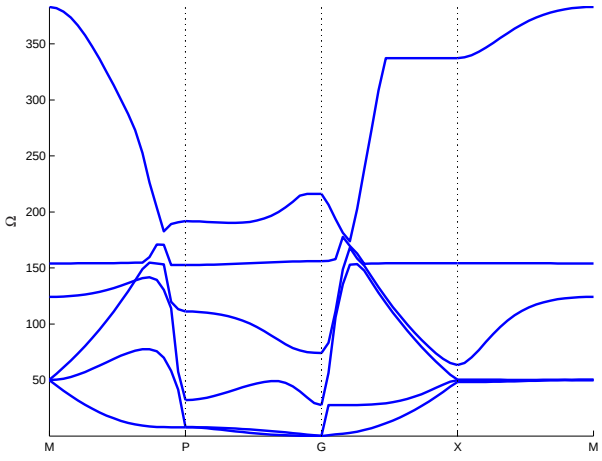

(c) $\alpha = 5$

Figure 77: Dispersion relations for rectangular grids

almost horizontal and parallel to the ε_x axis, thus indicating strong directionality of wave motion along the circumferential direction.

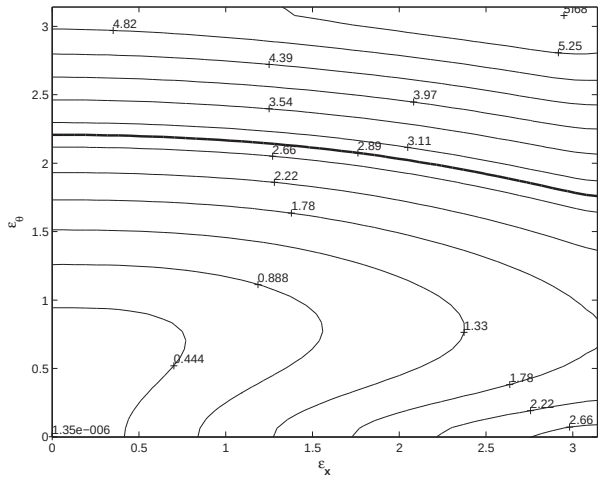

(a) $\beta = 30^\circ$

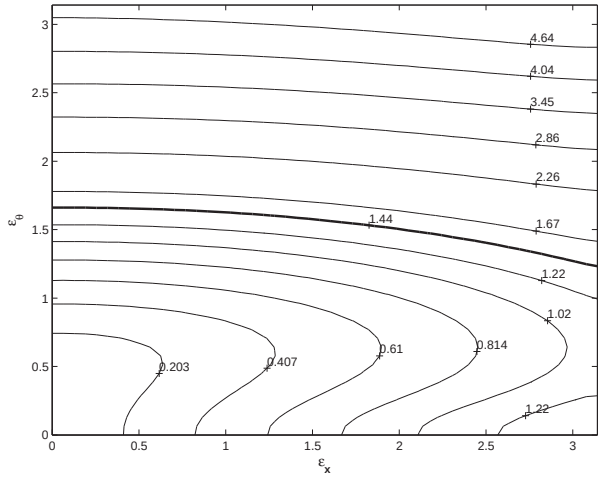

(b) $\beta = -30^\circ$

Figure 78: Phase constant surfaces for hexagonal grids (Bold lines: "Transition" frequency)

The propagation angles for both hexagonal grids are compared in Fig. 79. For the case where $\beta = 30^\circ$, at $\Omega = 2.9$ the maximum propagation angle drops from 90° to 35°, while for $\beta = -30^\circ$, the transition occurs at $\Omega = 1.4$, where it decreases from 90° to approximately 15°. This shows that directional behavior of the hexagonal cylindrical grid can be influenced by the cell topology. By changing the interior angle β from 30° to −30°, the directional behavior is observed at a lower frequency and the angle of propagation is reduced.

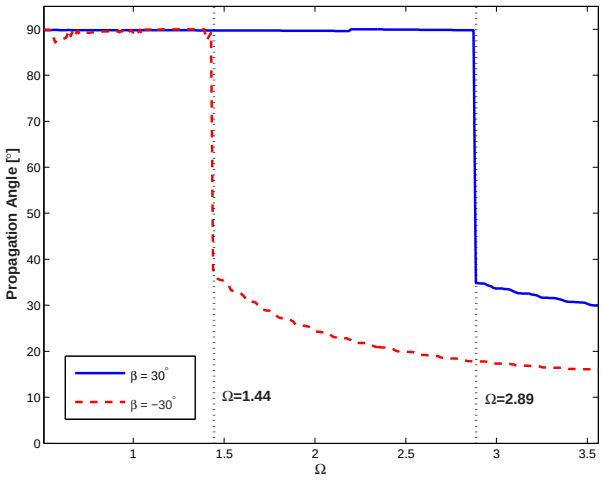

Figure 79: Propagation angles for rectangular grids

6.5.2 Harmonic response

The predictions obtained from the analysis of the phase constant surfaces are again verified by evaluating the harmonic response of the complete 2-D periodic assembly. The response of both hexagonal grids ($\beta = 30°$ and $\beta = -30°$) are considered at frequencies below and above the transition. The phase constant surfaces analysis has indicated that for the first grid, transition occurs at $\Omega \cong 2.9$, while for the second grid it takes place at $\Omega \cong 1.4$. The structure is again excited at a location along its center rim by a harmonic force of unit amplitude, and the corresponding displacement maps are shown in Fig. 80 and Fig. 81. Fig. 80.a shows the harmonic response of the first grid to an excitation frequency $\Omega = 0.75$, i.e. below transition, while the displacement map shown in Fig. 80.b corresponds to an excitation frequency of $\Omega = 3$. At this frequency, one can observe wave attenuation in the longitudinal direction, and propagation in the circumferential direction. Similar characteristics are found in the response of the second grid, which is here evaluated at 0.75 and 1.9 (see Fig. 81). The phenomenon of wave attenuation in the cylindrical grid is greatly affected by the geometry of the unit cell.

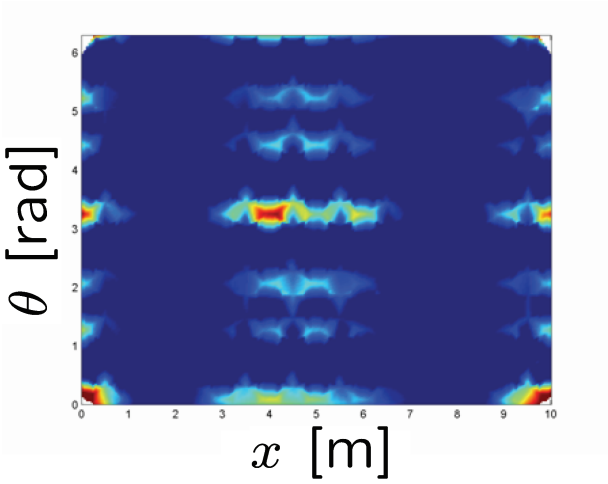

(a) $\Omega = 0.75$

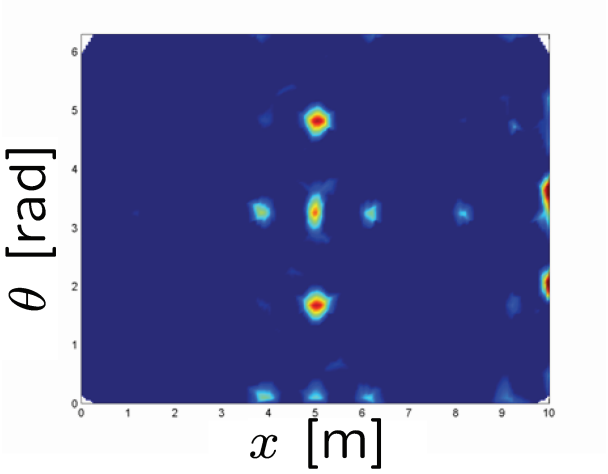

(b) $\Omega = 3$

Figure 80: Harmonic response for hexagonal grid with $\beta = 30°$

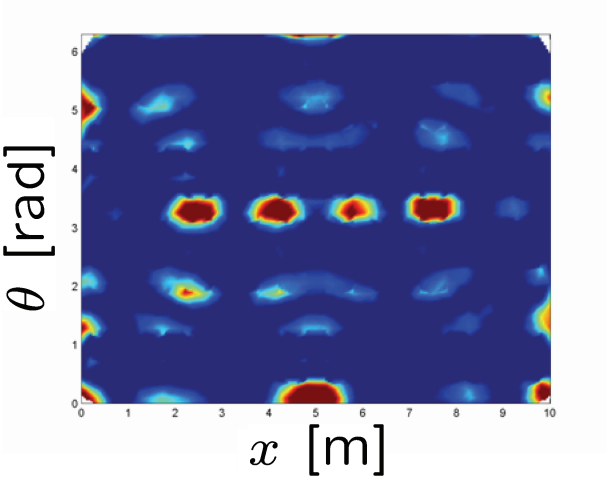

(a) $\Omega = 0.75$

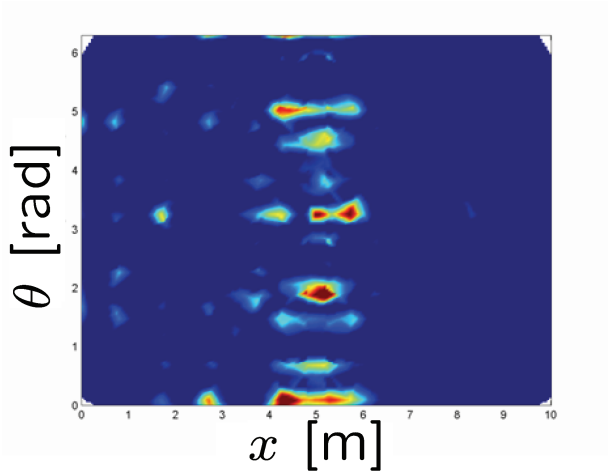

(b) $\Omega = 1.9$

Figure 81: Harmonic response for hexagonal grid with $\beta = -30°$

6.5.3 Band-gaps

The band-gap behavior of the hexagonal cylindrical grids is analyzed by considering the first Brillouin zone of the unit cell (Fig. 72). There is no additional symmetry in the phase constant surfaces, so the dispersion relations along the boundary $M \rightarrow P \rightarrow G \rightarrow X \rightarrow M$ must be considered. Both the regular ($\beta = +30°$) and re-entrant ($\beta = -30°$) hexagonal grid exhibit band-gap behavior. However the location and width of the band-gap are different for the two grids. For the regular hexagonal grid, there is a narrow band-gap around $\Omega = 2.6$ (Fig. 82.a). A harmonic radial load applied at a non-dimensional frequency of $\Omega = 2.6$ results in vibrations in the grid that are localized to the point of excitation (Fig. 83.a). For the re-entrant configuration, a much wider band-gap exists between $\Omega = 6.5$ and $\Omega = 8$ (Fig. 82.b). A harmonic radial load applied at a non-dimensional frequency of $\Omega = 7.5$ results in vibration in the re-entrant grid that is localized to the point of excitation, and waves are attenuated in all directions (Fig. 83.b).

The influence of the interior angle, β, on the band-gap behavior is studied by considering the width and location of the band-gap for various values of β. The indices used to measure the band-gap behavior is the total width of the band-gap $\Delta\Omega$ and the central frequency Ω_c, which is computed as the average of the highest and lowest frequency of the band-gap. The results of the sensitivity analysis are shown in Fig. 84. By decreasing β from 30° to 0, the width of the band-gap is gradually reduced but is observed at a lower frequency until it disappears at $\beta = 18°$. However, as β varies from 0 to $-30°$, the band-gap reappears at $\beta = -12°$, the width increases, and the central frequency decreases. This band-gap appears at a higher frequency than those observed when β is positive. Hence, for a large band-gap, a unit cell with a re-entrant configuration ($\beta < -12°$) is desired, but if the band-gap needs to be observed at the lowest possible frequency, then one with a positive β needs to be selected.

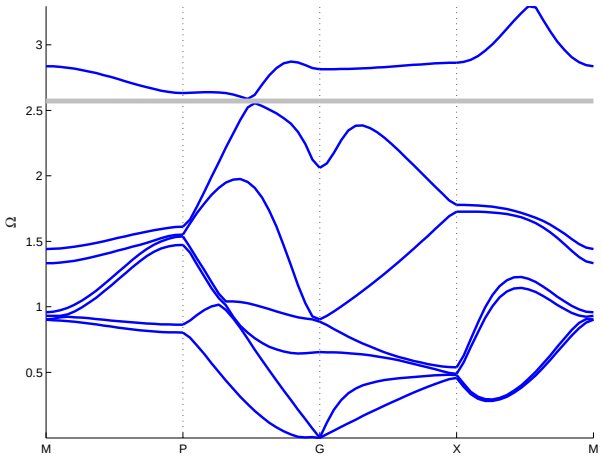

(a) $\beta = 30°$

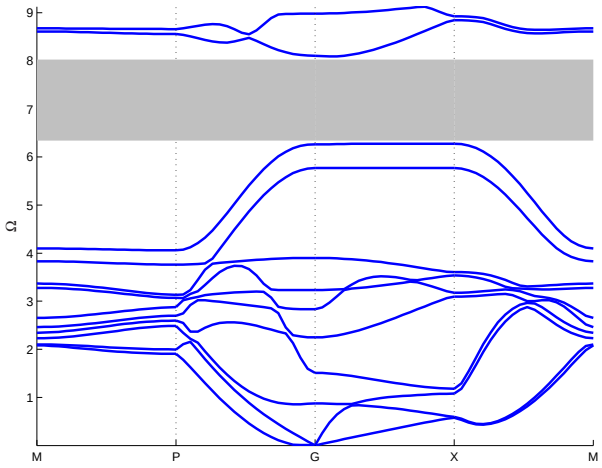

(b) $\beta = -30°$

Figure 82: Dispersion relations for hexagonal grids

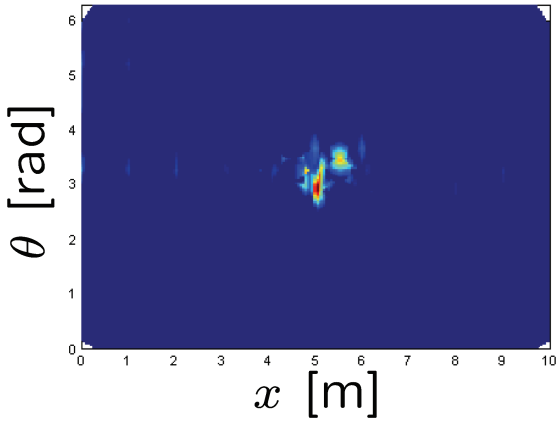

(a) $\beta = 30°$, $\Omega = 2.6$

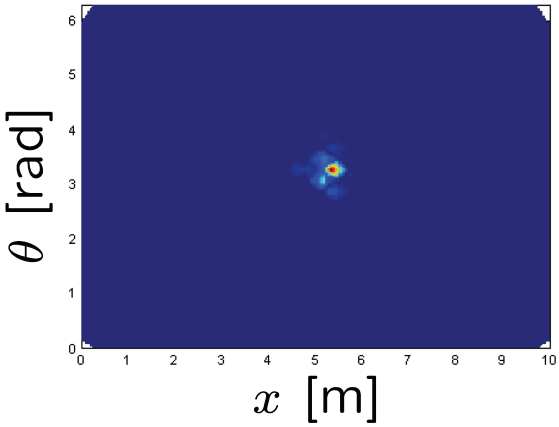

(b) $\beta = -30°$, $\Omega = 7.5$

Figure 83: Harmonic response for hexagonal grids

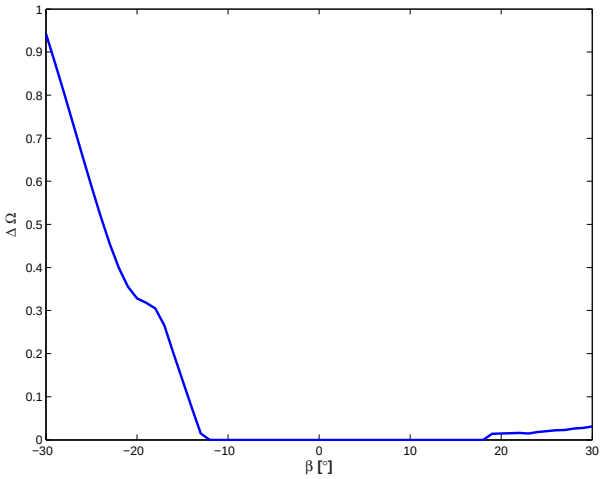

(a) Width of band-gap

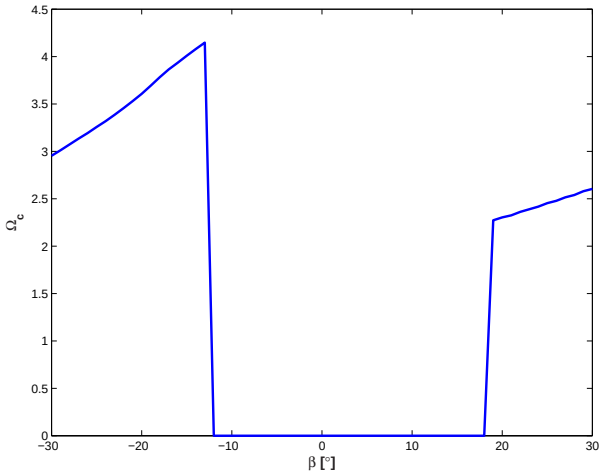

(b) Location of band-gap

Figure 84: Sensitivity analysis for hexagonal grids

CHAPTER VII

KAGOMÉ AND TETRAHEDRAL LATTICE STRUCTURES

7.1 Overview

Recent studies of ultra-light metallic systems have shown that periodic truss-like structures are as weight efficient as the best competing concepts [2] and may also possess superior thermo-structural, acoustic, and energy absorption characteristics [2]. The properties of such structures are generally linearly related to the relative density [8, 9, 7] of the assembly. Of the many proposed truss designs, the tetrahedron truss has shown a lot of promise (Fig. 85.a) in terms of static strength performance [10]. Sandwich panels with tetrahedron configuration have been optimized to improve their shear and compressive strength along with their bending characteristics in [7, 53]. A competing topology, known as the 3-D Kagomé (Fig. 85.b), has recently been proposed and the initial studies have shown that this design can show superior static performance with respect to the tetrahedron configuration [54]. This increase in performance has been mostly attributed to the greater resistance to plastic buckling for the same core density.

(a) Tetrahedron Truss (b) Kagomé Truss

Figure 85: Considered Truss Cores

The Kagomé configuration has also been proposed for morphing applications. Work by dos Santos e Lucato et al. [55] has in fact shown how localized actuation of selected Kagomé members can provide global shape control of an entire panel, or small, localized

deformations at selected locations.

The literature on the strength and static performance of truss topologies is slowly growing, yet little, or no work has been done to evaluate the dynamic characteristics of these class of structures. The dynamic analysis of these two topologies is therefore a natural completion of the general characterization of their performance. In particular, the work at hand attempts to investigate the directional and band-gap characteristics of Kagomé and tetrahedron truss topologies. Their wave attenuation and directional characteristics can be a significant addition to the functionality of this class of structures.

7.2 Performance of Kagomé Lattice

7.2.1 Kagomé Lattice Configuration

The single Kagomé cell is not periodic (Fig. 85.b) however two cells connected together forms a periodic unit cell (Fig. 86). The unit cell made up of two Kagomé cells will be analyzed to determine the wave propagation characteristics of the lattice.

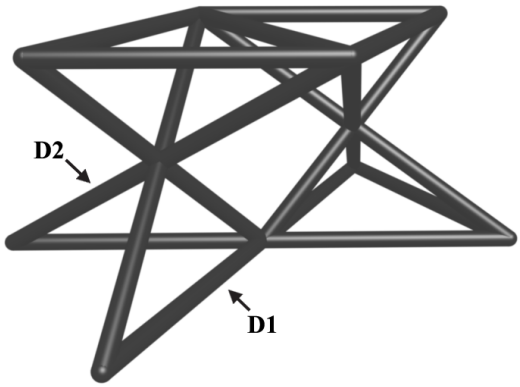

Figure 86: Unit Cell: Kagomé Truss

The considered Kagomé lattice is composed of beam elements of circular cross section rigidly connected to each other. The diameter of the members vary depending upon their orientation (Fig. 86). All planar beam elements that lie on the top and bottom surface have diameter D_1, while elements that connect the top and bottom surfaces have diameter D_2. The diameter D_1 is fixed at a non-dimensional length of $D_1/L_x = 20$, but D_2 is allowed to

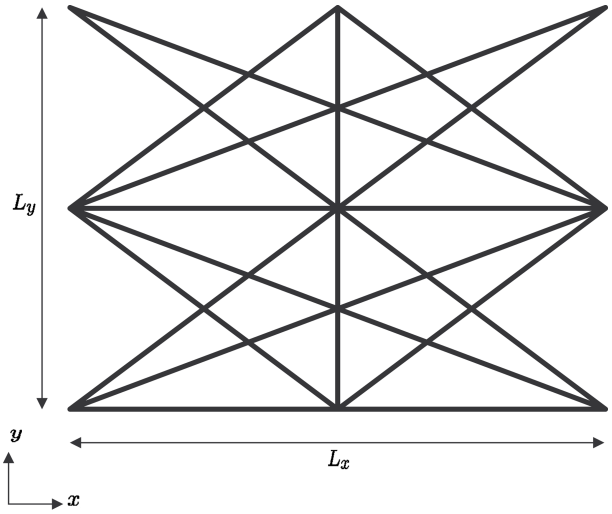

Figure 87: Dimensions of Kagomé Unit Cell

vary. The unit cell analyzed has equal length and width, $L_x = L_y$ (Fig. 87). The material properties of aluminum is used as a reference, but do not influence the non-dimensional results presented here. The non-dimensional parameter is computed by considering the dimensions of the straight beam on the top surface, and the corresponding value of ω_0 used here is 636.5 rad/s. The configuration of the unit cell is summarized in Table 17. The lattice is composed of 10 cells in the x direction and 5 cells in y direction.

Table 17: Mechanical properties and geometry of Kagomé truss core.

Property	Value	Units
Young's Modulus	7.0×10^{10}	Pa
Density	2700	$\mathrm{Kg/m^3}$
Poisson's Ratio	0.3	
D_1/L_x	20	

7.2.2 Phase Constant Surfaces

The first phase constant surface for the Kagomé core is evaluated for two different configurations, $D_2 = D_1$ and $D_2 = 2D_1$ (Fig. 88). Both configurations show strong directional behavior in the y direction. For $D_2 = D_1$, wave attenuation along the x direction appears

to happen at $\Omega \cong 2.4$. For the case of $D_2 = 2D_1$, the directional behavior is instead observed at a higher frequency of $\Omega \cong 3.5$. Aside from the non-dimensional frequency at which the directional behavior is observed, the two configurations feature similar characteristics. However the configuration of $D_2 = D_1$ is preferred if directional behavior is desired at a lower frequency.

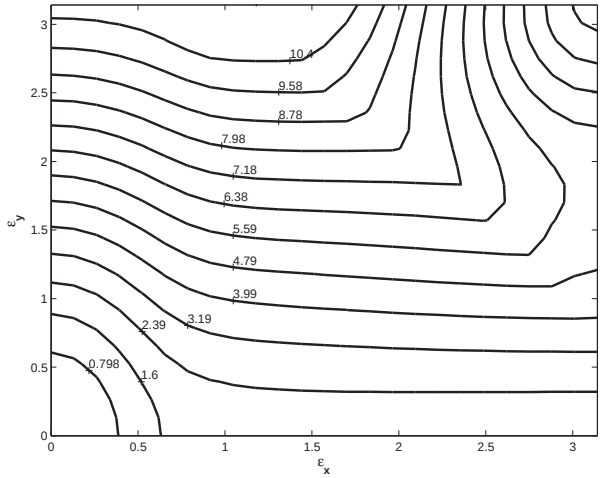

(a) $D_2 = D_1$

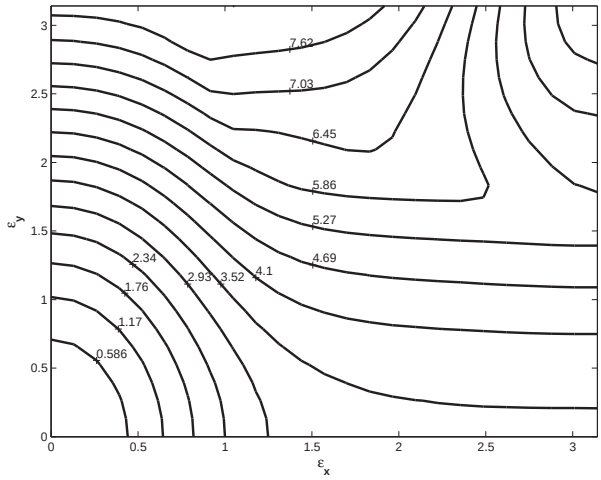

(b) $D_2 = 2D_1$

Figure 88: Phase Constant Surface: Kagomé Truss

7.2.3 Harmonic Response

The predictions obtained from the analysis of the phase constant surfaces are validated through the evaluation of the harmonic response of the lattice using SFEs. A harmonic out

of plane load is applied at the center of the lattice (Fig. 89) and the out of displacement is represented as a colormap. The harmonic response of both lattice configurations is found for an excitation frequency of $\Omega = 1.2$ where no directional behavior is observed (Fig. 90.a & Fig. 91.a). Then the frequency at which the directional behavior is most evident is found for each configuration. For the configuration $D_2 = D_1$, directional behavior is very evident at a non-dimensional frequency of $\Omega = 4.7$ (Fig. 90.b). However for the configuration with $D_2 = 2D_1$, such evident directional behavior is only observed at around $\Omega = 8.5$ (Fig. 91.b).

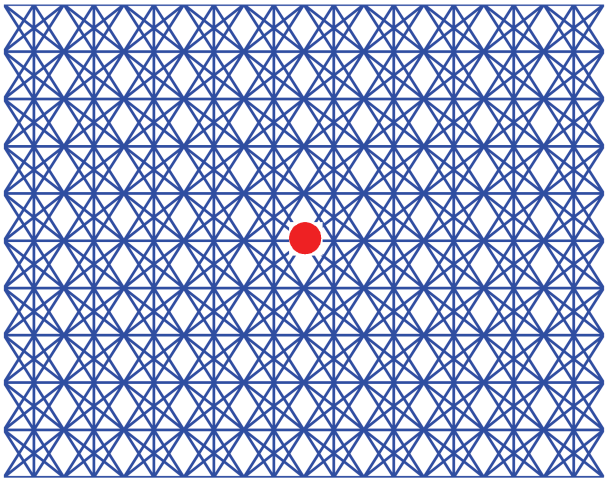

(a) 2-D View

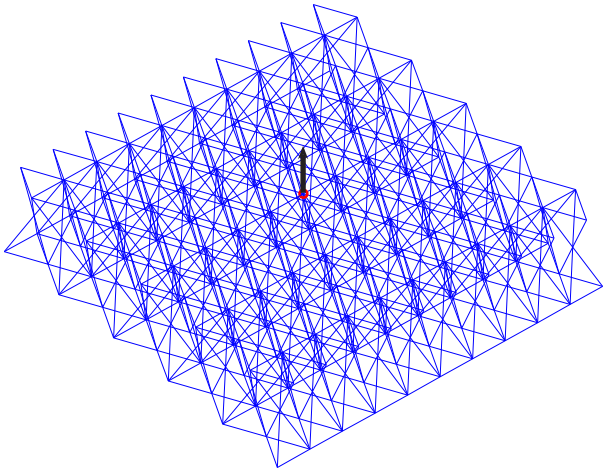

(b) 3-D View

Figure 89: Kagomé Lattice: Point of Excitation

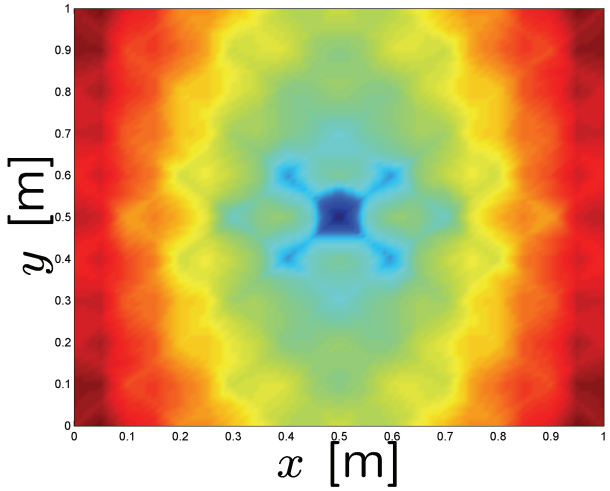

(a) $\Omega = 1.2$

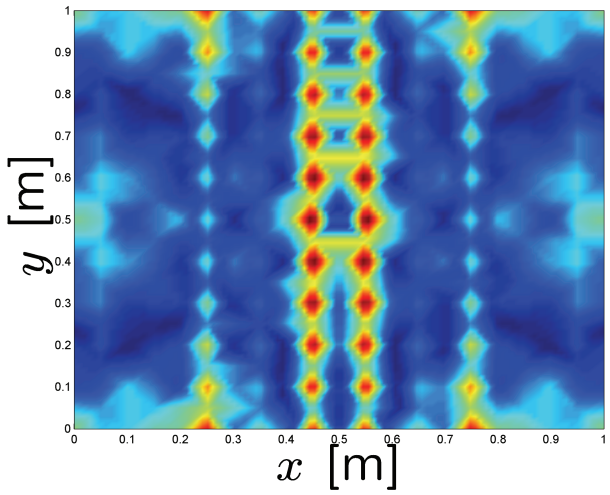

(b) $\Omega = 4.7$

Figure 90: Harmonic Response of Kagomé Lattice: $D_2 = D_1$

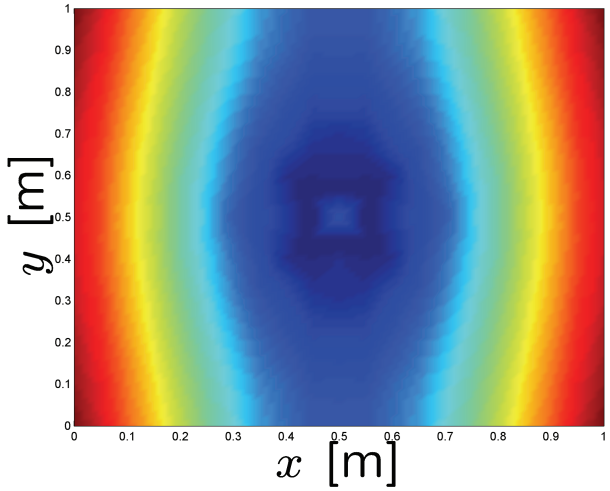

(a) $\Omega = 1.2$

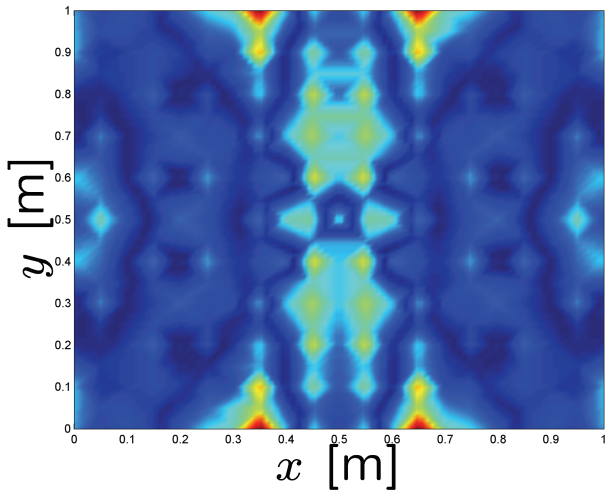

(b) $\Omega = 8.5$

Figure 91: Harmonic Response of Kagomé Lattice: $D_2 = 2D_1$

7.2.4 Band-gaps

The band-gap behavior of the two considered Kagomé lattice configurations is analyzed by considering the first Brillouin zone of the unit cell (Fig. 92). There is no additional symmetry in the phase constant surfaces, so the dispersion relations along the boundary $M \rightarrow P \rightarrow G \rightarrow X \rightarrow M$ must be considered. Unfortunately, no band-gap behavior was found for any of the configurations considered (Fig. 93).

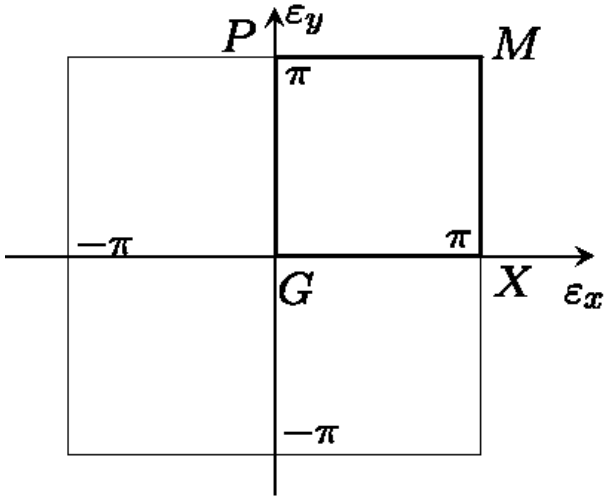

Figure 92: First Brillouin Zone: Kagomé Truss

7.3 Performance of Tetrahedron Lattice

7.3.1 Tetrahedron Lattice Configuration

The considered tetrahedron lattice is composed of beam elements of circular cross section rigidly connected to each other. The projection of the lattice on the x, y plane appears as an hexagonal lattice, whose geometry can be defined by the internal angle β (Fig. 94). The non-dimensional parameter is computed by considering the dimensions of the horizontal beam connecting the bottom and top surface with internal angle $\beta = 30°$, with a corresponding value of $\omega_0 = 609.3$ rad/s. The influence of this parameter on the dynamic characteristics of the lattice can be thus investigated. A unit cell with equal characteristic dimensions, $L_x = L_y$, is chosen and the diameter of the members is fixed at a non-dimensional length of $D_1/L_x = 20$ (Fig. 94). The lattice is composed of 10 cells in the x direction and 10 cells in

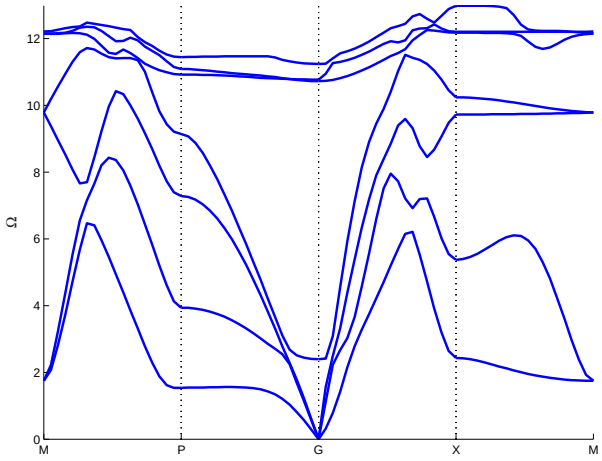

(a) $D_2 = D_1$

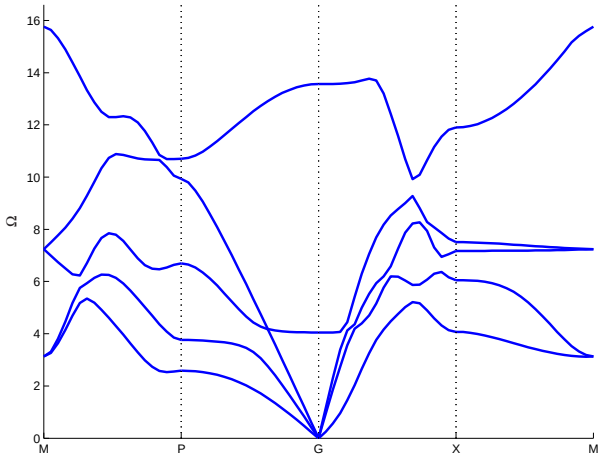

(b) $D_2 = 2D_1$

Figure 93: Dispersion Relations: Kagomé Truss

y direction to form a lattice with 100 cells. The configuration is summarized in Table 18. The material properties of aluminum are again used as a reference.

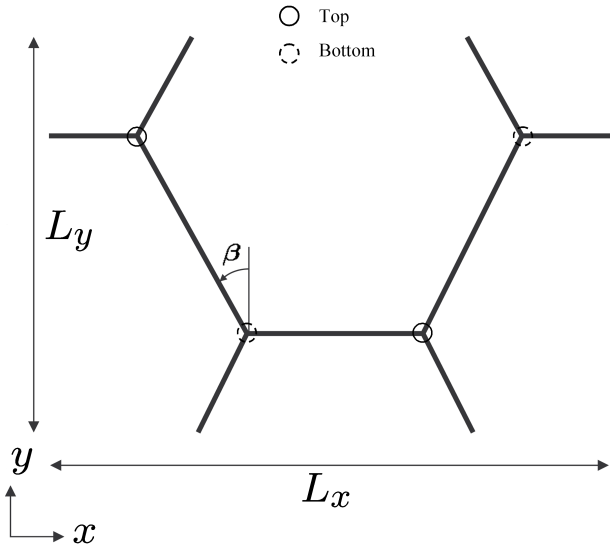

Figure 94: Dimensions of Tetrahedron Unit Cell

Table 18: Mechanical properties and geometry of Tetrahedron truss core.

Property	Value	Units
Young's Modulus	7.0×10^{10}	Pa
Density	2700	Kg/m^3
Poisson's Ratio	0.3	
D_1/L_x	20	

7.3.2 Phase Constant Surfaces

The first phase constant surface for the tetrahedron cell is evaluated for two different configurations, one with $\beta = 30°$ and the other with a re-entrant geometry (Fig. 95), $\beta = -30°$, (Fig. 96), however neither configurations show evident directional behavior.

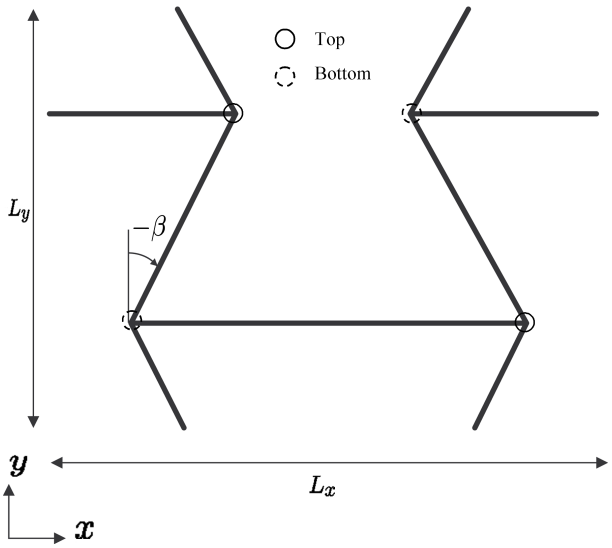

Figure 95: Tetrahedron Unit Cell with Re-entrant Geometry

7.3.3 Band-gaps

The band-gap behavior of the two considered tetrahedron lattice configurations is analyzed by considering the first Brillouin zone of the unit cell (Fig. 97). Large band-gaps are found in both configurations (Fig. 98), and the only difference is in the width of the band-gap. The tetrahedron core with the re-entrant geometry shows a slightly wider band-gap, starting from $\Omega \cong 0.8$ and ending at $\Omega \cong 6$ Hz (Fig. 98.b). The core with $\beta = 30°$ has a band-gap that extends from $\Omega \cong 1$ to $\Omega \cong 5.7$ (Fig. 98.a).

7.3.4 Harmonic Response

The predictions obtained from the analysis of the dispersion relations are validated through the evaluation of the harmonic response of the lattice. A harmonic out-of-plane load is applied at the center of the lattice (circle in Fig. 99) and the out-of-plane displacement is represented as a color map. The harmonic response of both lattice configurations is found for an excitation frequency of $\Omega = 0.18$ which is below the band-gap (Figs. 100.a and 101.a). It is clearly evident that waves are free to propagate in both lattices at this frequency. When the excitation frequency is increased to $\Omega = 1.81$, the band-gap phenomenon is observed in both lattices. Waves are attenuated in all directions and vibration is localized to the region

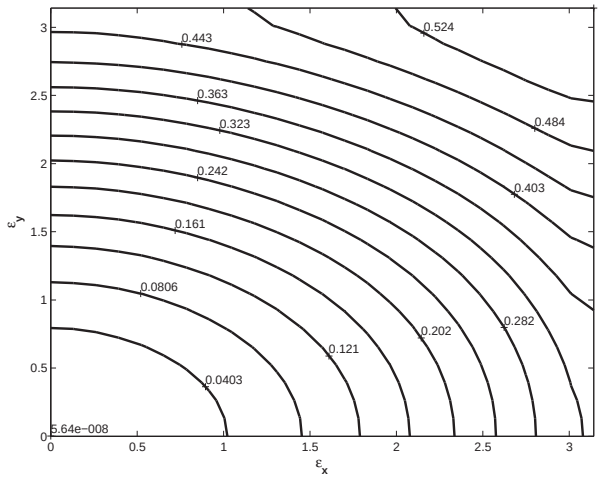

(a) $\beta = 30°$

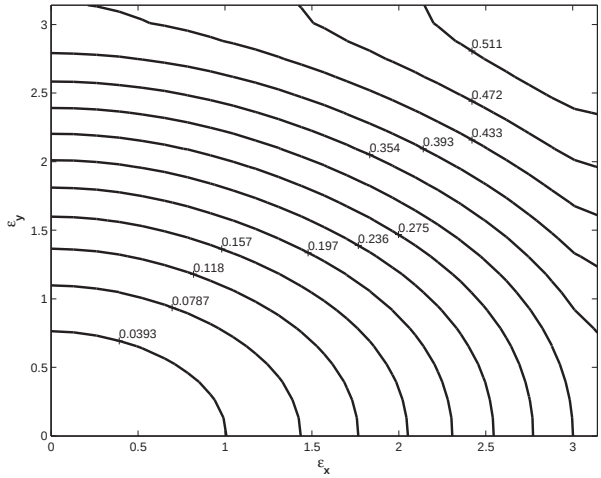

(b) $\beta = -30°$

Figure 96: Phase Constant Surface: Tetrahedron Truss

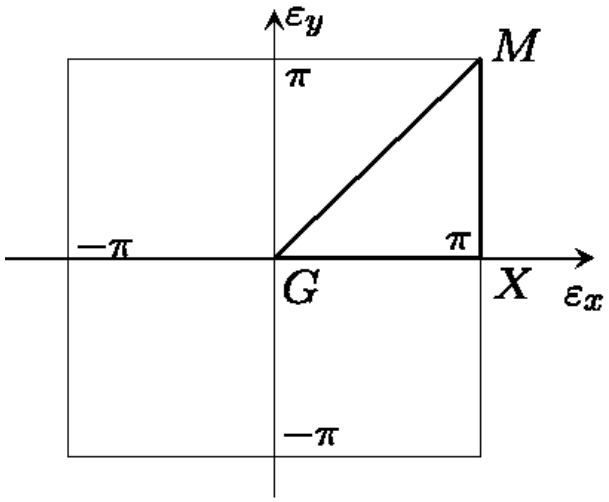

Figure 97: First Brillouin Zone: Tetrahedron Truss

around the point of excitation (Figs. 100.b and 101.b). Finally, at a frequency of $\Omega = 5.8$, there is evidence of wave propagation in the lattice corresponding to $\beta = 30°$ (Fig 100.c) but waves are still attenuated in all directions in the lattice with the re-entrant configuration (Fig 101.c).

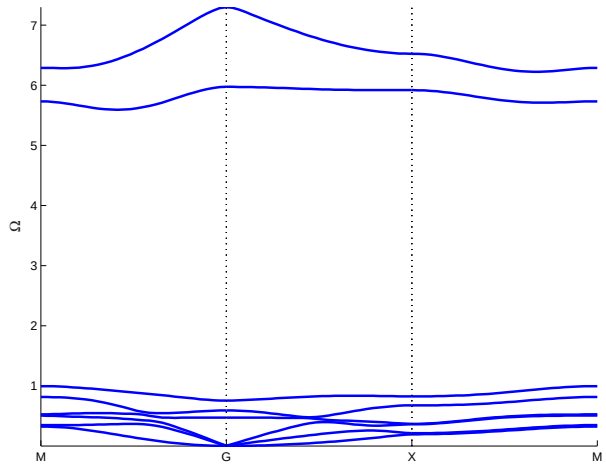

(a) $\beta = 30°$

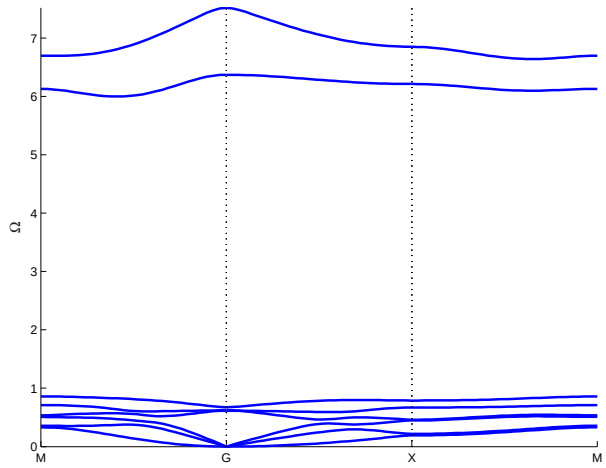

(b) $\beta = -30°$

Figure 98: Dispersion Relations: Tetrahedron Truss

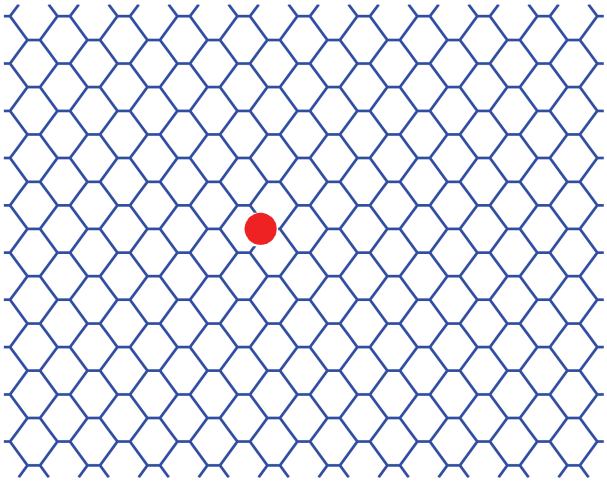

(a) 2-D View

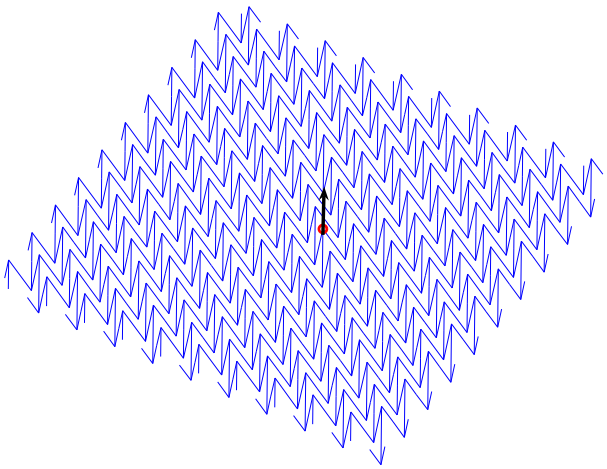

(b) 3-D View

Figure 99: Tetrahedron Lattice: Point of Excitation

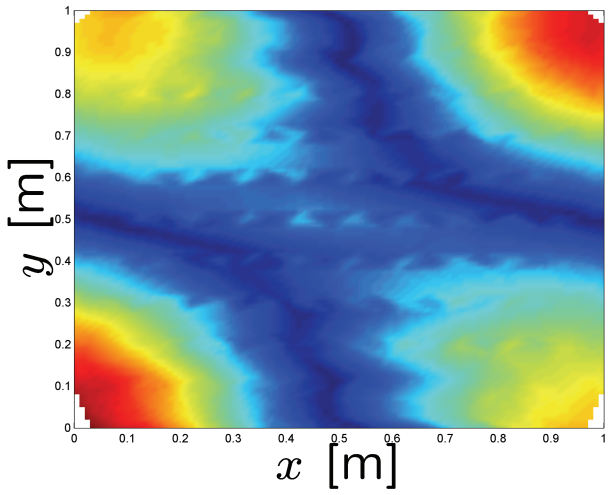

(a) $\Omega = 0.18$

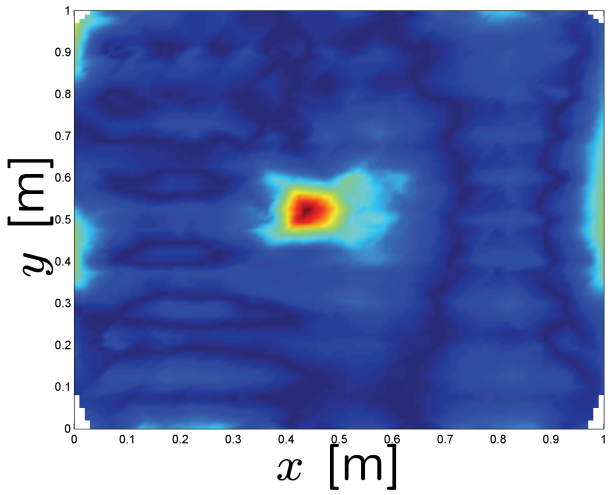

(b) $\Omega = 1.81$

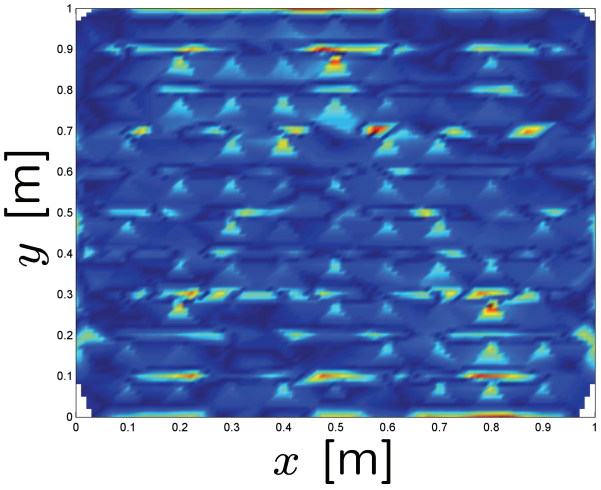

(c) $\Omega = 5.8$

Figure 100: Harmonic Response of Tetrahedron Lattice: $\beta = 30°$

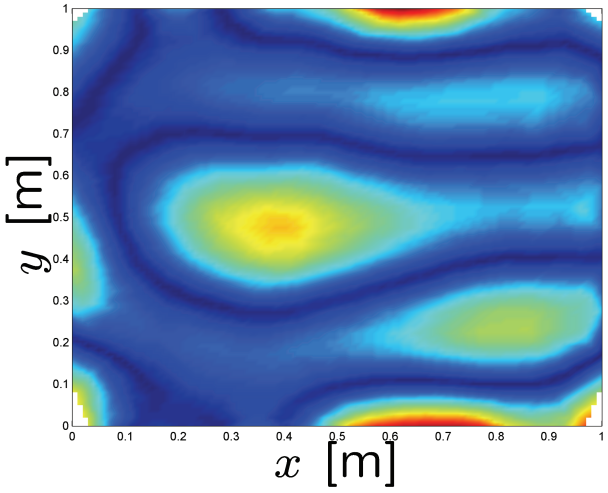

(a) $\Omega = 0.18$ Hz

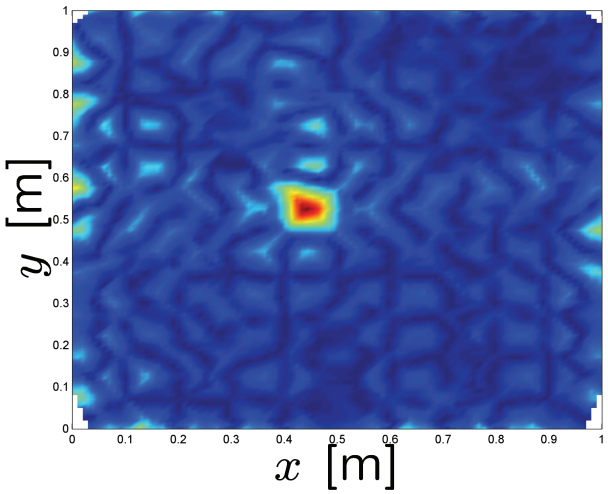

(b) $\Omega = 1.81$ Hz

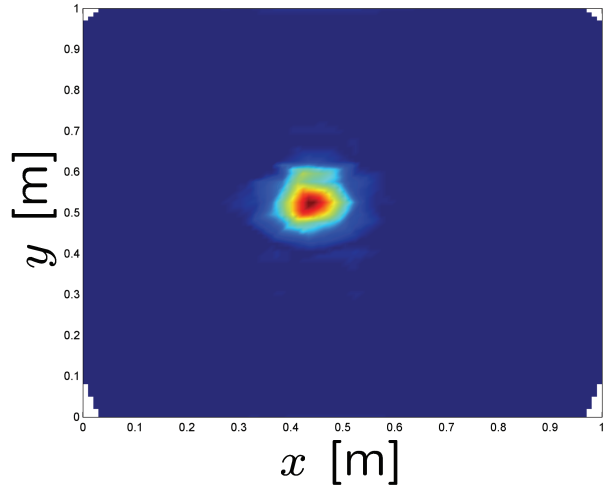

(c) $\Omega = 5.8$

Figure 101: Harmonic Response of Tetrahedron Lattice: $\beta = -30°$

CHAPTER VIII

CONCLUSIONS

8.1 Conclusions

This work investigates the dynamic characteristics of 2-D periodic cellular structures. This is done by recognizing that deterministic cellular structures can also be classified as periodic structures. It is found that these class of structures show directional and/or band-gap behavior. Directional behavior is the phenomenon where vibrations are attenuated in certain directions but not others, while band-gap behavior is the phenomenon where vibrations are attenuated in all directions. A spring-mass lattice system is first considered to gain insight into the reasons for this unique dynamic behavior which is found to be associated with the in-plane variations of mass and stiffness distributions. The directional behavior in particular is associated with the stiffness distribution, while it is shown that the occurrence of a band-gap corresponds to an internal resonance within a unit cell.

The study is extended to systems with distributed mass and stiffness properties, and for this reason robust finite element models are formulated to predict the dynamic characteristics of unit cells and complete lattices. The first continuous system considered is a 2-D rectangular grid with beams of varying cross-sectional geometry. It is found that changes in the cell geometry result in different directionality and band-gap characteristics. A sensitivity analysis is performed to identify trends which may lead the design of this class of grid as mechanical pass-band filters in given directions. The analysis is completed by the formulation of an optimization problem, where optimal configurations for directional only, band-gap only and both behaviors are found.

Extending on the initial study of systems with distributed mass and stiffness, "practical" configurations of periodic cellular structures are investigated. The first class of such structures analyzed are cylindrical grid lattices. In here, the effect of changes in topology is studied in addition to changes in geometry. The influence of cell geometry is studied for the case of rectangular cylindrical grids, where the uniform grid considered exhibits directional behavior in the circumferential direction. However increasing the mass and stiffness

along the axial direction through changes in the cell geometry, results in a cylindrical grid that exhibits strong directional behavior in the axial direction. This analysis demonstrates the potential for tailoring directional behavior in periodic cellular structures. The effect of topology is studied using a hexagonal cylindrical grids. In the considered configuration, an interior angle is varied to determine the effect of topology changes to the unit cell. A sensitivity analysis shows that small changes of the cell topology can cause significant changes in the directional and band-gap behavior. This analysis demonstrates the potential of affecting the dynamic performance of the grids with minimal configuration modifications.

The work then describes the analysis performed on concepts proposed by other researchers, namely the Kagomé and tetrahedron configurations. The Kagomé and tetrahedron trusses are selected because they show superior static strength performance compared to other ultra-light design concepts. The Kagomé configuration has also been proposed for shape morphing applications. The research on this class of structures has mostly characterized their strength and static performance. The dynamic characterization is performed as a natural extension of the on-going work and to complement their other documented capabilities. The Kagomé configuration has shown to exhibit better static characteristics, but this analysis indicates that the tetrahedron truss are potentially more useful in applications where dynamic performance is also of importance.

In summary, the research demonstrates that it is possible to influence the dynamic behavior of even the simplest periodic cellular geometries with minimum changes to the cell configuration. Geometry and/or topology influence the range of frequencies over which directional and band-gap behavior occur.

The inverse problem of designing a specific unit cell to match a desired set of dynamic characteristic is also of interest. The optimal configuration of a unit cell for a specified band-gap and directional behavior over an arbitrary frequency range is a general problem worth investigating. However, this problem is an investigation of topology optimization which is outside the scope of the current work. Additionally, more work needs to be done to further the understanding of the band-gap and directional phenomenons before a solution to such a general problem can be found.

8.2 Future Work

8.2.1 Experimental Validation of Complex Lattice Structures

The experimental investigations carried out in Chapter 5 can be extended to more complex lattice structures such as those considered in Chapter 7. The work can also be extended to consider truss core lattices with attached face sheets, which is a configuration that is used in ultra-light weight applications. Experimental investigations of directional behavior in lattices should also be performed. Overcoming manufacturing limitations will be necessary for the experimental investigations on more complex lattices.

8.2.2 Cylindrical Lattice Structures

The two types of periodic cellular structures detailed herein have been simple rectangular and cylindrical grids. The current study can be extended to consider the dynamic performance of cylindrical structures made up of curved truss core panels (Fig. 102). In particular, the structural-acoustic performance of this type of cylinders should be analyzed. Cylindrical panels have many practical applications where structural-acoustic performance is important, like submarine hulls, aircraft fuselages and pay-load fairings. A study can be carried out to investigate the acoustic transmission properties of cylinders with different core topologies, and the effect of core topology and geometry on the acoustic properties.

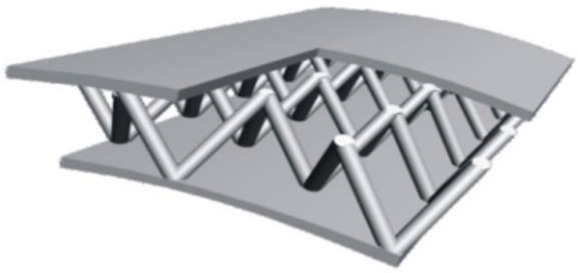

Figure 102: Curved Truss Core Panel

8.2.3 Multifunctional Optimization

One of the major contributions of this work is the dynamic characterization of deterministic cellular structures, hence adding to their well-documented multifunctional properties [2]. However, little work has been done to consider all or several of these multifunctional properties for design. Liu and Lu [4] investigated the optimal configuration of tetrahedron core panels for multiple loading cases and minimum weight. Aside from this investigation, no work has been done in the design optimization of cellular structures to take full advantage of their numerous desirable engineering properties. An example of such an optimization would be the design of a truss with superior strength-to-weight performance, acting as a passive mechanical filter or as a vibration isolator over specified frequency ranges. Such a truss design would be desirable in several different applications. An extension of this work would be to incorporate the computational tools developed herein to existing optimization methodologies and/or environments for the design of cellular structures with optimal performance characteristics in several areas, hence fully utilizing their potential as multifunctional structures.

REFERENCES

[1] Gibson, L., Ashby, M., and Clarke, D., *Celluar Solids: Structure and Properties*. Cambridge: Cambridge University Press, 1999.

[2] Evans, A., Hutchinson, J., and Ashby, M., "Multifunctionality of cellular metal systems," *Progress in Materials Science*, vol. 43, pp. 171–221, 1999.

[3] Evans, A., Hutchinson, J., Fleck, N., Ashby, M., and Wadley, H., "The topological design of multifunctional cellular metals," *Progress in Materials Science*, vol. 46, pp. 309–327, 2001.

[4] Liu, J. and Lu, T., "Multi-objective and multi-loading optimization of ultralight-weight truss materials," *International Journal of Solids and Structures*, vol. 41, pp. 619–635, 2004.

[5] Gu, S., Lu, T., and Evans, A., "On the design of two-dimensional cellular metals for combined heat dissipation and structural load capacity," *International Journal of Heat and Mass Transfer*, vol. 44, pp. 2163–2175, 2001.

[6] Lakes, R., "Deformation mechanisms in negative poisson's ratio materials: Structural aspects," *Journal of Material Science*, vol. 26, pp. 2287–2291, 1991.

[7] Chiras, S., Mumm, D., Evans, A., Wicks, N., Hutchinson, J., Dharmasena, K., Wadley, H., and Fitchter, S., "The structural performance of optimized truss core panels," *International Journal of Solids and Structures*, vol. 39, pp. 4093–4115, 2002.

[8] Wallach, J. and Gibson, L., "Mechanical behavior of a three-dimensional truss material," *International Journal of Solids and Structures*, vol. 38, pp. 7181–7196, 2001.

[9] Deshpande, V., Fleck, N., and Ashby, M., "Effective properties of the octet-truss lattice material," *Journal of Mech. Phys. Solids*, vol. 49, pp. 1747–1769, 2001.

[10] Deshpande, V. and Fleck, N., "Collapse of truss core sandwich beams in 3-point bending," *International Journal of Solids and Structures*, vol. 38, pp. 6275–6305, 2001.

[11] Wicks, N. and Hutchinson, J., "Optimal truss plates," *International Journal of Solids and Structures*, vol. 38, pp. 5165–5183, 2001.

[12] Huybrechts, S. and Tsai, S., *Analysis and behavior of grid structures*. Massachusetts: Elsevier Science Limited, 1996.

[13] Huybrechts, S. and Meink, T., "Advanced grid stiffened structures for the next generation of launch vehicles," in *Proceedings of Aerospace Conference*, vol. 1, pp. 263–270, IEEE, 1997.

[14] Meink, T., "Composite grid vs composite sandwich: A comparison based on payload shroud requirements," in *Proceedings of Aerospace Conference*, vol. 1, pp. 215–220, IEEE, 1998.

[15] Vipperman, J., Li, D., and Avdeev, I., "Investigation of the transmission loss behavior of an advanced grid-stiffened structure," in *ASME International Mechanical Engineering Congress and Exposition*, (New York), 2001.

[16] Cremer, L. and Leilich, H., "Zur theorie der biegekettenleiter," *Archive der Elektrischen Ubertragung*, vol. 7, p. 261, 1953.

[17] Brillouin, L., *Wave Propagation in Periodic Structures*. New York: Dover, 1953.

[18] Lord Rayleigh, "On the maintenance of vibrations by forces of double frequency, and on the propagation of waves through a medium endowed with a periodic structure," *Philosophical Magazine*, vol. XXXIV, pp. 145–149, 1887.

[19] Miles, J., "Vibrations of beams on many supports," *Proceedings of the American Society of Civil Engineers*, vol. 82, 1956.

[20] Heckl, M., "Investigations on the vibrations of grillages and other simple beam structures," *Journal of the Acoustical Society of America*, vol. 36, pp. 1335–1343, 1964.

[21] Mead, D. and Wilby, E., "The random vibrations of a multi-supported heavily damped beam," *The Shock and Vibration Bulletin*, vol. 35, pp. 45–55, 1966.

[22] Gupta, G. S., *Dynamics of Periodically Stiffened Structures Using a Wave Approach*. PhD thesis, University of Southampton, 1970.

[23] Gupta, G. S., "Natural frequencies of periodic rib-skin structures using a wave approach," *Journal of Sound and Vibration*, vol. 16, pp. 567–580, 1971.

[24] DeEpsindola, J., *Numerical Methods in Wave Propagation in Periodic Structures*. PhD thesis, University of Southampton, 1974.

[25] Zhong, W. and Williams, F., "On the direct solution of wave propagation for repetitive structures," *Journal of Sound and Vibration*, vol. 181, pp. 485–501, 1995.

[26] Abrahamson, A., *The Response of Periodic Structures to Aero-Acoustic Pressures, with Particular Reference to Aircraft Skin-Rib-Spar Structures*. PhD thesis, University of Southampton, 1973.

[27] Mead, D., "A general theory of harmonic wave propagation in linear periodic systems with multiple coupling," *Journal of Sound and Vibration*, vol. 27, pp. 235–260, 1973.

[28] Orris, R. and Petyt, M., "A finite element study of harmonic wave propagation in periodic structures," *Journal of Sound and Vibration*, vol. 33, pp. 223–236, 1974.

[29] Orris, R. and Petyt, M., "Random response of periodic structures by a finite element technique," *Journal of Sound and Vibration*, vol. 43, pp. 1–8, 1975.

[30] Bardell, N. and Mead, D., "Free vibration of an orthogonally stiffened cylindrical shell, part i: Discrete line simple supports," *Journal of Sound and Vibration*, vol. 134, pp. 29–54, 1989.

[31] Ashby, M., Evans, A., Fleck, N., Gibson, L., Hutchinson, J., and Wadley, H., *Metal Foams: A Design Guide*. Butterworth-Heinemann, 2000.

[32] Langley, R., "The response of two-dimensional periodic structures to point harmonic forcing," *Journal of Sound and Vibration*, vol. 197, no. 4, pp. 447–469, 1996.

[33] Stokes, G., *Mathematical and Physical Papers*. Cambridge University Press, 1883.

[34] Brillouin, L., *Wave Propagation and Group Velocity*. London: Academic Press, 1960.

[35] Mead, D., "Free wave propagation in periodically supported infinite beams," *Journal of Sound and Vibration*, vol. 11, no. 1, pp. 181–197, 1970.

[36] Mead, D., "Plates with regular stiffening in acoustic media: vibration and radiation," *Journal of the Acoustical Society of America*, vol. 88, no. 1, pp. 391–401, 1990.

[37] Jensen, J., "Phononic band gaps and vibrations in one- and two-dimensional mass-spring structures," *Journal of Sound and Vibration*, vol. 266, pp. 1053–1078, 2003.

[38] Bathe, K., *Finite Element Procedures*. New Jersey: Prentice-Hall, 1996.

[39] Doyle, J., *Wave Propagation in Structures*. New York: Springer-Verlag, 1997.

[40] Stolarski, H. and Belytschko, T., "Membrane locking and reduced integration for curved element," *Journal of Applied Mechanics*, vol. 49, pp. 172–176, 1982.

[41] Meck, H., "An accurate polynomial displacement function for finite ring elements," *Computers & Structures*, vol. 11, pp. 265–269, 1980.

[42] Bathe, K. and Chaudhary, A., "On the displacement formulation of torsion of shafts with rectangular cross-sections," *International Journal of Numerical Methods in Engineering*, vol. 18, pp. 1565–1580, 1982.

[43] Doyle, J., "A spectrally-formulated finite element for longitudinal wave propagation," *International Journal of Analytical and Experimental Modal Analysis*, vol. 3, pp. 1–5, 1988.

[44] Martinsson, P. and Movchan, A., "Vibrations of lattice structures and phononic bandgaps," *Journal of Mechanics and Applied Mathematics*, vol. 56, pp. 45–64, 2003.

[45] Mead, D., "Wave propagation and nautral modes in periodic systems: Ii. multi-coupled systems, with and without damping," *Journal of Sound and Vibration*, vol. 40, no. 1, pp. 19–39, 1975.

[46] Mead, D., "Wave propagation in continuous periodic structures: research contributions from southampton 1964–1996," *Journal of Sound and Vibration*, vol. 190, no. 3, pp. 495–524, 1996.

[47] Langley, R. and Bardell, N., "The response of two-dimensional periodic structures to harmonic point loading: A theoretical and experimental study of a beam grillage," *Journal of Sound and Vibration*, vol. 207, no. 4, pp. 521–535, 1997.

[48] Lin, Y., "Chapter iii: Random vibration of periodic and almost periodic structures," in *Mechanics Today* (Nemat-Nasser, S., ed.), vol. 3, New York: Pergamon Press, 1976.

[49] Thomas, D., "Dynamics of rotationally periodic structures," *International Journal for Numerical Methods in Engineering*, vol. 14, pp. 81–102, 1979.

[50] Petyt, M., *Introduction to Finite Element Vibration Analysis*. Cambridge: Cambridge University Press, 1998.

[51] Ruzzene, M., Scarpa, F., and Soranna, F., "Wave beaming effects in two-dimensional cellular structures," *Smart Materials and Structures*, vol. 12, pp. 363–372, 2003.

[52] Langley, R., "On the modal density and energy flow characteristics of periodic structures," *Journal of Sound and Vibration*, vol. 172, pp. 491–511, 1994.

[53] Evans, A., "Lightweight materials and structures," *Mater. Res. Bull*, vol. 26, pp. 790–797, 2001.

[54] Wang, J., Evans, A., Dharmasena, K., and Wadley, H., "On the performance of truss panels with kagomé cores," *International Journal of Solids and Structures*, vol. 40, pp. 6981–6988, 2003.

[55] dos Santos e Lucato, S., McMeeking, R., and Evans, A., "Kagomé-based high authority shape morphing structure," *Proceedings of 2004 ASME International Mechanical Engineering Congress and Exposition*, pp. 1–6, 2004.

[56] Vipperman, J., Li, D., and Avdeev, I., "Characterization and control of sound radiation in a complex fairing structure," in *Proceedings of InterNoise-01 Conference*, pp. 2429–2435, InterNoise, 2001.

[57] Bathe, K. and Almeida, C., "A simple and effective pipe elbow element - interaction effects," *Journal of Applied Mechanics*, vol. 49, pp. 165–171, 1982.

[58] Meirovitch, L. and Baruh, H., "On the inclusion principle for the hierarchical finite element method," *International Journal for Numerical Methods in Engineering*, vol. 19, no. 281-291, 1983.

[59] Lee, U., "Equivalent continuum models of large platelike lattice structures," *International Journal of Solids and Structures*, vol. 31, no. 4, pp. 457–467, 1994.

[60] Lee, U., "Dynamic continuum modeling of truss-type space structures using spectral elements," *Journal of Spacecraft and Rockets*, vol. 33, no. 3, pp. 404–409, 1996.

[61] Lee, U., "Equivalent continuum representation of lattice beams: Spectral element approach," *Journal of Engineering Structures*, vol. 20, no. 7, pp. 587–592, 1998.

[62] Mead, D., "Wave propagation and nautral modes in periodic systems: I. mono-coupled systems," *Journal of Sound and Vibration*, vol. 40, no. 1, pp. 1–18, 1975.

[63] Bardell, N. and Mead, D., "Free vibration of an orthogonally stiffened cylindrical shell, part i: Discrete line simple supports," *Journal of Sound and Vibration*, vol. 134, no. 1, pp. 29–54, 1989.

[64] Bardell, N. and Mead, D., "Free vibration of an orthogonally stiffened cylindrical shell, part ii: Discrete general stiffeners," *Journal of Sound and Vibration*, vol. 134, no. 1, pp. 55–72, 1989.

[65] Langley, R. and Bardell, N., "The response of two-dimensional periodic structures to harmonic point loading: A theoretical and experimental study of a beam grillage," *Journal of Sound and Vibration*, vol. 207, no. 4, pp. 521–535, 1997.

[66] Mester, S. and Benaroya, H., "Periodic and near periodic structures," *Shock and Vibration*, vol. 2, no. 1, pp. 69–95, 1995.

[67] Shen, I., "Vibration of rotationally periodic structures," *Journal of Sound and Vibration*, vol. 172, no. 4, pp. 459–470, 1994.